# Electronic, spin-dependent, conductive properties of modified graphene

**Abhilash Ravikumar**

A thesis presented for the degree of

Doctor of Philosophy


Department of Materials Science

University of Milano-Bicocca

Italy

**Electronic, spin-dependent, conductive properties of modified graphene**

Ph.D. Thesis

Abhilash Ravikumar

Supervisor: Prof. Gian Paolo Brivio

Co-Supervisor: Dr. Guido Fratesi

Secondment Supervisor: Dr. Daniel Sánchez Portal

*To truth and beauty*

# Acknowledgements

This wonderful journey of entering research from being a software engineer, stuck at a dead-end job in India could never have been possible without lot of hard work and dedication from my side, but also unimaginable support from various people close to me who entered my life at the perfect time to guide and nurture me forward. This acknowledgement does not do enough justice to all their help and support but is just a small way of showing my gratitude.

My first thanks is to my professor, Prof. Gianpaolo Brivio, for making all this possible. His contribution to my life has been immense and my heartfelt thanks for the opportunity, support, guidance and his wonderful love for physics.

My co-supervisor, Dr. Guido Fratesi, is one of the most intelligent minds I have had the pleasure of interacting with (and also a genuinely good and humble person) and I am truly grateful for that. His patience and care, research methodology, attention to detail and an inherent understanding of physics have been some of the several qualities I have tried to learn from and I am thankful for his guidance and support. I am also grateful to my supervisor during my secondments at Centro de Física de Materiales (CSIC-UPV/EHU), San Sebastian, Dr. Daniel Sánchez Portal, for his support and guidance during my stay there. I am also indebt to Dr. Maria Cristina Fassina, who was very helpful when I went to her regarding any

administrative work.

To my parents, who continue to love and support me at every juncture of my life, especially at the time when I had to change my career path. All of this would not have been possible without their belief. I would also like to thank my grandmother (Seetamma) for all her love and childhood stories!

To my uncle, Jaggu chittapa, who is one of my inspirations to enter research, I thank you for all the support and guidance. A heartfelt thanks to my early physics teacher, Seema mam, who used to bring physics textbooks from her college library for me and spend hours discussing them. I am also grateful to Dr. Rizwan Rahman and Brahma for their support. A shout out to Jyo, Shru and Dumms (The Sai Rams gang) !

A big thanks to my research group: Anu Baby, Aldo Ugolotti, Moritz Muller and He Lin for all discussions, support and great camaraderie. A special thanks also to one of my really good friends (and flat-mate), Myles Rooney, this sarcastic Irish guy who loves travel, beer (and racist jokes !). I probably wouldn't have seen any place in Europe if it wasn't for you, so thanks pal! To Pikakshi, Jyoti, Sudhi, Murali and the cricket gang of Milan, thanks for all the wonderful memories.

To Ayush Raj Goel, my brother, my best friend and everything else ! Thank you.

The computational resources used were provided by CINECA, DIPC (Donostia International Physics Center)-CFM (Centro de Física de Materiales) and our JIGEN from University of Milano-Bicocca and I would like to thank these in-

stitutions for the support. I acknowledge the Marie-Curie THINFACE training network for the opportunity and funding of my PhD program. This work was performed within the PCAM European Doctorate Programme.

# Contents

# List of Figures

# Chapter 1

# Abstract

Understanding the adsorption mechanisms of organic molecules on graphene and their subsequent influence on the electronic and magnetic properties of this interface is essential in designing graphene based devices. In this thesis we perform first principles calculations based on density functional theory (DFT) in an effort to understand these phenomena. Most organic electronic devices are composed of interfaces formed by the organic overlayer and a metallic electrode. Understanding the charge transfer dynamics at the interface would help engineer efficient organic devices.

With this in mind, the first part of research we present is the adsorption of core-excited organic molecules on graphene. We predict the induction or suppression of magnetism in the valence shell of physisorbed and chemisorbed organic molecules on graphene occurring on the femtosecond time scale as a result of core level excitations. We consider three organic molecules: Pyridine - whose interaction with graphene is mainly facilitated by van der Waals forces, Picoline radical - an intermediate case where there is a strong van der Waals interaction of the pyridine $\pi$ ring with graphene but a covalent bonding of the molecule and pyridine

radical - where the interaction is mainly through covalent bonding, and study the ground state and N 1s core excited state electronic properties for these systems. For physisorbed molecules, where the interaction with graphene is dominated by van der Waals forces and the system is non-magnetic in the ground state, numerical simulations based on density functional theory show that the valence electrons relax towards a spin polarized configuration upon excitation of a core-level electron. The magnetism depends on efficient electron transfer from graphene on the femtosecond time scale. On the other hand, when graphene is covalently functionalized, the system is magnetic in the ground state showing two spin dependent mid gap states localized around the adsorption site. At variance with the physisorbed case upon core-level excitation, the LUMO of the molecule and the mid gap states of graphene hybridize and the relaxed valence shell is not magnetic anymore.

Next we discuss the interplay between the charge transfer lifetime of core excited organic molecules adsorbed on graphene and the modification of its electronic structure by a variable coupling with a metal substrate. The nitrogen 1s core electron of 1,1′- bipyridine $(C_5H_4N)_2$ is photo-excited and adsorbed on bilayer graphene/nickel(111) (BP/BLG/Ni) and epitaxially grown graphene/Ni(111) (BP/ EG/ Ni). We predict from first principle calculations that the charge transfer time of core excited molecules depend strongly on the coupling of graphene to the underlying Ni substrate. In the ground state, the LUMO of the molecule is quite strongly coupled with the substrate in both the cases (BP/BLG/Ni and BP/EG/Ni). In the case of BP/BLG/Ni, the layer of graphene in contact with nickel substrate strongly hybridizes but the upper layer of graphene remains fairly decoupled. The excited molecular LUMO* finds very few states of graphene close to the Dirac point at the Fermi level to hybridize with. This leads to a decoupled molecular LUMO* and the lifetime increases significantly ($\sim$ 116 fs). But in

the case of BP/EG/Ni, the strong hybridization of graphene with the underlying nickel substrate significantly distorts the electronic structure of graphene generating states close to the Fermi level. The LUMO* of the molecule strongly couples with these states resulting in a substantially smaller lifetime ($\sim$ 33 fs). We also find experimental evidence to confirm this trend by performing core-hole-clock spectroscopy. The resonant charge transfer lifetime we find is $\sim$ 30 fs$\pm$5 fs for the BP/BLG/Ni and $\sim$ 4 fs$\pm$1 fs for the BP/EG/Ni, thus clearly demonstrating the effect of substrate on the charge transfer dynamics of organic molecules on graphene.

This thesis is structured as follows: In the second chapter we review graphene and recent advances in graphene technology. The physical properties of graphene and the study of its electronic structure from Tight-Binding approach, DFT and experiments are discussed. This is followed by a summary of its chemical, electronic, magnetic and mechanical properties. Several experimental techniques to synthesize graphene such as exfoliation, epitaxial routes and growth on metal substrates are detailed followed by a discussion on the electronic applications of graphene.

In the third chapter, we briefly review the electronic structure theory for many electron systems such as Hartree-Fock approach, Thomas-Fermi model, Hohenberg-Kohn and Kohn-Sham theorems which setup the backbone for density functional theory. Approximations within DFT such as the local density approximation, local spin density approximation and generalized gradient approximation are discussed. We also summarize the non-equilibrium Green's function approach, an alternate electronic structure approach which is used to simulate bulk continuum by coupling the system to self-energy operators.

These methods are mainly used to calculate the ground state electronic structure of systems. In the fourth chapter we discuss the excited state methods which can successfully simulate spectroscopic experiments such as x-ray photo-emission spectroscopy (XPS) (evaluated by initial state approximation and $\Delta$ SCF approximation), near-edge x-ray absorption fine structure (NEXAFS) (calculated by the transition potential approach) and core-hole-clock (CHC) technique (which can be calculated by the $\Delta$ SCF approach and the charge transfer lifetime extracted from the intrinsic Lorentzian linewidths of the molecular coupling with the substrate).

Chapter 5 details the phenomenon of femtomagnetism which is induced/ suppressed in graphene by the adsorption of core level excited organic molecules. We find that the adsorption mechanism of the organic molecules play a crucial role in effecting the system magnetism. We study three cases: pyridine, picoline radical and pyridine radical, each with a different adsorption mechanism when interacting with graphene, and study the electronic and magnetic properties of these system upon molecular core-level excitation.

Chapter 6 discusses the dynamic charge transfer lifetime of a molecular overlayer with respect to the variable coupling of graphene with a metal substrate. Core excited bipyridine is adsorbed on epitaxially grown graphene/Ni(111) and bilayer graphene/Ni(111) and study the interaction of the molecule in these two cases. The charge transfer dynamics and extraction of the charge transfer lifetime from these interfaces are discussed and these results are validated using core-hole-clock measurements. In chapter 7 we conclude by summarizing our results followed by the references used.

# Chapter 2

# A brief review of graphene

Carbon is an extremely versatile element of the periodic table capable of forming a variety of allotropes due to its valency. It is a non-metallic tetra-valent element with the capability of forming sp /$sp^2$/$sp^3$ hybridized compounds. Its unique ability to form various organic compounds and long chain polymers at temperatures commonly encountered on earth enables this element to exist in diverse forms. Well known stable allotropes of carbon are diamond and graphite. In the recent years several more allotropes like fullerenes, carbon nanotubes and 2 dimensional (2-D) graphene have been discovered. Graphite, as named by Abraham Gottlob Werner in 1789, is one of the most stable and common allotrope of carbon. As seen from Figure 2.1 (b), it consists of planar $sp^2$ hybridized, hexagonal lattice structured carbons, stacked on top of each other and stabilized by the interplanar $\pi$-$\pi$ interactions. A single layer of graphite is called graphene, which until recently, was expected to be thermodynamically unstable and hence not to exist.

In 2004, the research group of K. S. Novoselov and A. K. Geim from the University of Manchester [1] isolated graphene. It is a 2-D allotrope of carbon with a honeycomb lattice structure. The carbon atoms of graphene are $sp^2$ hybridized leading to a trigonal planar structure with a carbon-carbon bond of 1.42

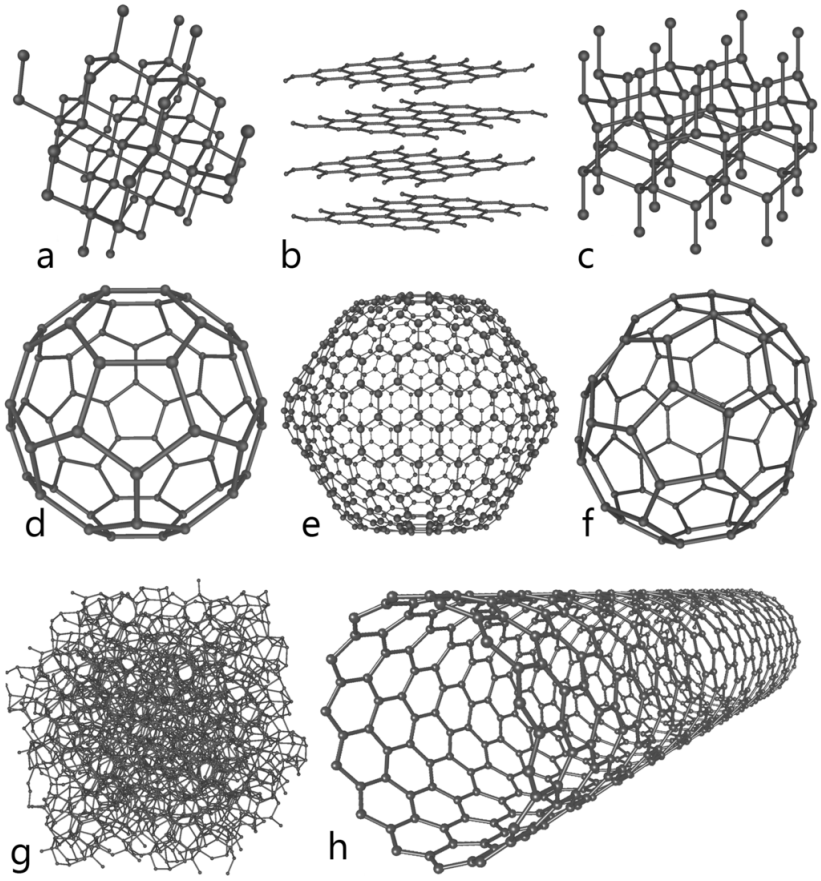


Figure 2.1: Some of the allotropes of carbon: a) diamond, b) graphite, c) lonsdaleite, d) C60 buckminsterfullerene, e) C540, Fullerite f) C70, g) amorphous carbon, and h) single-walled carbon nanotube. (The image is taken from Wikipedia, the free encyclopedia)

Å. The electrons of the 2s and 2p orbitals hybridize to form half filled $\pi$ bands which play an important role in physics of such strongly correlated systems. The primitive cell of the hexagonal crystal lattice consists of two inequivalent carbon atoms named A and B in Figure 2.2. The lattice vectors in the real space are $\mathbf{a}_1=\frac{a}{2}\,(3,\sqrt{3})$ and $\mathbf{a}_2=\frac{a}{2}\,(3,-\sqrt{3})$. The nearest neighbour vectors in the real space are $\delta_1=\frac{a}{2}\,(1,\sqrt{3})$, $\delta_2=\frac{a}{2}\,(1,-\sqrt{3})$ and $\delta_3=-a(1,0)$. Here $a$ is the

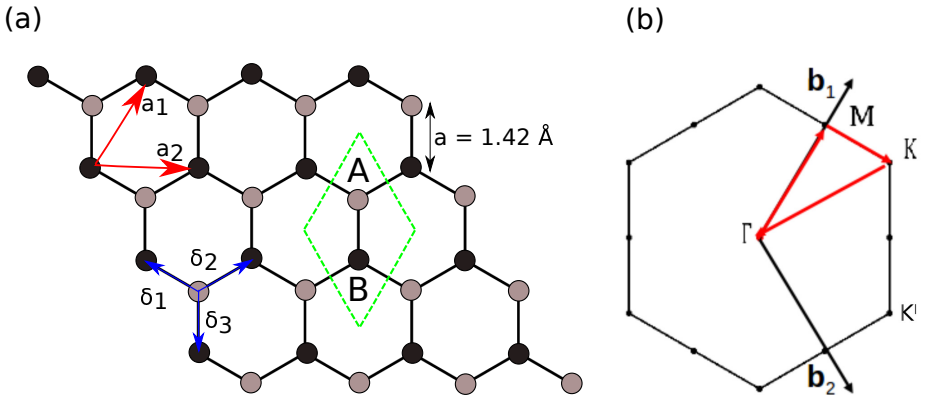


Figure 2.2: The honeycomb crystal structure of graphene in (a) real space. $\mathbf{a}_1$ and $\mathbf{a}_2$ are the unit lattice vectors of the triangular Bravais lattice. A and B represent the two inequivalent sub-lattices with C-C bond length of 1.42 Å. $\delta_1$, $\delta_2$, $\delta_3$ are the nearest neighbour carbon atoms. (b) The reciprocal lattice of the triangular lattice. Its primitive lattice vectors are $\mathbf{b}_1$ and $\mathbf{b}_2$. The path along the first irreducible Brillouin zone is $\Gamma - M - K - \Gamma$. The Dirac cones are located at $K$ and $K^{|}$.

C-C distance which is 1.42 Å. The reciprocal lattice vectors are $\mathbf{b}_1$=$\frac{2\pi}{3a}$ $(1,\sqrt{3})$ and $\mathbf{b}_2$=$\frac{2\pi}{3a}$ $(1,-\sqrt{3})$. The points $K$ and $K^{|}$ of the Brillouin zone are of particular importance for graphene physics. Their positions in the reciprocal space are $K = (\frac{2\pi}{3a}, \frac{2\pi}{3\sqrt{3}a})$ and $K^{|} = (\frac{2\pi}{3a}, -\frac{2\pi}{3\sqrt{3}a})$. The electronic band structure of graphene was first studied by P.R.Wallace in 1947 [2] when he was exploring the theoretical background of graphite.

## 2.1 Tight-Binding model for electrons in a honeycomb lattice

In this section we calculate the energy of the $\pi$ bands in graphene, where one confronts the problem of two atoms per unit cell. The formal solution of the tight binding model is presented with a brief discussion of the Bloch's theorem and we calculate the energy dispersion of the $\pi$ bands of graphene taking into account the nearest neighbour overlap corrections.

The general idea of the tight binding model is to take into account a basis set of orbitals centered at each lattice point $\phi^{(a)}(\mathbf{r})$, where $a$ labels the atomic orbitals. For a simple Bravais lattice of one atom per unit cell with one electron, the Hamiltonian is given by

$$H = -\frac{\hbar^2}{2m}\nabla_r^2 + \sum_{j=1}^{N} V(\mathbf{r}-\mathbf{R}_j) \tag{2.1}$$

where $\nabla_r^2$ is the 2 dimensional Laplacian operator since we will be focusing on tight binding solution for 2-D graphene system and $m$ is the mass of electron. The ions on the sites $\mathbf{R}_j$ interacts with the electron yielding an overall potential energy $\sum_{j=1}^{N} V(r-\mathbf{R}_j)$, where N is the total number of lattice sites. The assumption considered while formulating the tight binding approach is that the electron, at position $l$ is bound to a particular ionic lattice site $\mathbf{R}_l$. The interactions from other ionic lattice sites is described after introducing Bloch waves.

### 2.1.1 Bloch Theorem

To reflect the underlying lattice symmetries and the translational invariance, we make up new wavefunctions satisfying the Bloch's theorem. The translation by a

lattice vector $\mathbf{R_i}$ can be described by a quantum mechanical operator:

$$\top_{\mathbf{R_i}} = e^{\frac{i}{\hbar}\widehat{\mathbf{p}}.\mathbf{R}_i} \tag{2.2}$$

Here the momentum operator $\widehat{\mathbf{p}}$ must be defined suitably for a crystal lattice and may be named a quasi- momentum operator. The translation operator must commute with the full Hamiltonian as $[\top_{\mathbf{R}_i}, H] = 0$ since it is a symmetry operation which leaves the physical problem invariant. This would imply that the Eigen states of the full Hamiltonian $H$ are also the eigenstates of $\top_{\mathbf{R}_i}$ for any lattice vector $\mathbf{R_i}$ and the quasi crystal momentum $\mathbf{p} = \hbar\mathbf{k}$ with $\mathbf{k}$ the reciprocal space wave vector limited to the first Brillouin zone.

A Bloch wavefunction is constructed from the atomic orbital wavefunction $\phi^{(a)}(r - \mathbf{R_j})$ taking into account the above mentioned considerations:

$$\psi^{(a)}_{\mathbf{k}}(r) = \sum_{\mathbf{R}_j} e^{i\mathbf{k}.\mathbf{R}_j}\, \phi^{(a)}(r - \mathbf{R}_j) \tag{2.3}$$

These are good trial wavefunctions which fulfill the translational invariance of the lattice and are the eigen states of $\top_{\mathbf{R}_i}$ so that the solution of the eigen value problem can be conducted as a linear combination of these states.

### 2.1.2 Lattice with two atoms per unit cell

When there is more than one atom per unit cell, the above reasoning is slightly modified. Here since the translation operation by a vector $\delta_j$ relates one inequivalent sub-lattice to another inequivalent lattice site, $[\top_{\delta_j}, H] \neq 0$ if the translation operator remains $\top_{\delta_j} = e^{\frac{i}{\hbar}\widehat{p}.\delta_j}$. Therefore these inequivalent sub-lattices must be treated separately. In the case of graphene, where there are two inequivalent carbons in the unit cell and in the current formulation we include only the $p_z$ states,

the trial wavefunction is written as

$$\psi_{\mathbf{k}}(\mathbf{r}) = a_{\mathbf{k}}\psi^{A}_{\mathbf{k}}(\mathbf{r}) \; + \; b_{\mathbf{k}}\psi^{B}_{\mathbf{k}}(\mathbf{r}) \tag{2.4}$$

where $a_{\mathbf{k}}$ and $b_{\mathbf{k}}$ are complex functions with quasi momentum $\mathbf{k}$. $\psi^{A}_{\mathbf{k}}(\mathbf{r})$ and $\psi^{B}_{\mathbf{k}}(\mathbf{r})$ are both Bloch functions which can be expanded as

$$\psi^{j}_{\mathbf{k}}(\mathbf{r}) = \sum_{\mathbf{R}_l} e^{i.\mathbf{k}.\mathbf{R}_l} \; \phi^{j}(\mathbf{r} + \delta_j - \mathbf{R}_l) \tag{2.5}$$

where $j$ is the label on the two inequivalent sub-lattices A/B and $\delta_j$ is the vector that connects the $j^{th}$ atom with the underlying Bravais lattice. For convenience we can choose one of the sub lattice (atomic site A in this case) as reference. Now we search for solution of the Schrödinger equation with the help of these trial wavefunctions

$$H\psi_{\mathbf{k}} = \varepsilon_{\mathbf{k}}\psi_{\mathbf{k}} \tag{2.6}$$

Multiplying both sides with $\psi^{*}_{\mathbf{k}}$ and expanding the terms, the equation can be rewritten in the matrix form as

$$\begin{bmatrix} a^{*}_{\mathbf{k}} & b^{*}_{\mathbf{k}} \end{bmatrix} H_{\mathbf{k}} \begin{bmatrix} a_{\mathbf{k}} \\ b_{\mathbf{k}} \end{bmatrix} = \varepsilon_{\mathbf{k}} \begin{bmatrix} a^{*}_{\mathbf{k}} & b^{*}_{\mathbf{k}} \end{bmatrix} S_{\mathbf{k}} \begin{bmatrix} a_{\mathbf{k}} \\ b_{\mathbf{k}} \end{bmatrix} \tag{2.7}$$

Where the Hamiltonian matrix $H_{\mathbf{k}}$ is

$$H_{\mathbf{k}} \equiv \begin{bmatrix} \psi^{(A)*}_{\mathbf{k}} H \psi^{(A)}_{\mathbf{k}} & \psi^{(A)*}_{\mathbf{k}} H \psi^{(B)}_{\mathbf{k}} \\ \psi^{(B)*}_{\mathbf{k}} H \psi^{(A)}_{\mathbf{k}} & \psi^{(B)*}_{\mathbf{k}} H \psi^{(B)}_{\mathbf{k}} \end{bmatrix} = H^{\dagger}_{\mathbf{k}} \tag{2.8}$$

and the overlap matrix is

$$S_{\mathbf{k}} \equiv \begin{bmatrix} \psi^{(A)*}_{\mathbf{k}} \psi^{(A)}_{\mathbf{k}} & \psi^{(A)*}_{\mathbf{k}} \psi^{(B)}_{\mathbf{k}} \\ \psi^{(B)*}_{\mathbf{k}} \psi^{(A)}_{\mathbf{k}} & \psi^{(B)*}_{\mathbf{k}} \psi^{(B)}_{\mathbf{k}} \end{bmatrix} = S^{\dagger}_{\mathbf{k}} \tag{2.9}$$

The eigenenergy values $\varepsilon_{\mathbf{k}}$ of the Schrödinger equation which represent the energy dispersion or the energy bands are obtained by solving the secular equation

$$det[H_{\mathbf{k}} - \varepsilon^{\lambda}_{\mathbf{k}} S_{\mathbf{k}}] = 0 \tag{2.10}$$

where $\lambda$ denotes the labels on the energy bands. The solution for this secular equation is derived in [2] and these energy bands have the form

$$E_{\pm}(\mathbf{k}) = \pm t\sqrt{3+f(\mathbf{k}-t'f(\mathbf{k}))} \tag{2.11}$$

where

$$f(\mathbf{k}) = 2\cos(\sqrt{3}k_y a) + 4\cos(\frac{\sqrt{3}}{2}k_y a)\cos(\frac{3}{2}k_x a) \tag{2.12}$$

$t$ is the nearest neighbour hopping energy which $\approx$ 2.8eV. $t'$ is the next nearest neighbour hopping energy whose estimate from *ab initio* calculations was $0.02t \lesssim t' \lesssim 0.2t$ [3, 4]. The plus and minus signs refer to the upper $\pi^*$ and the lower $\pi$ bands respectively.

The full electronic band structure is shown in Figure 2.3. The energy dispersion

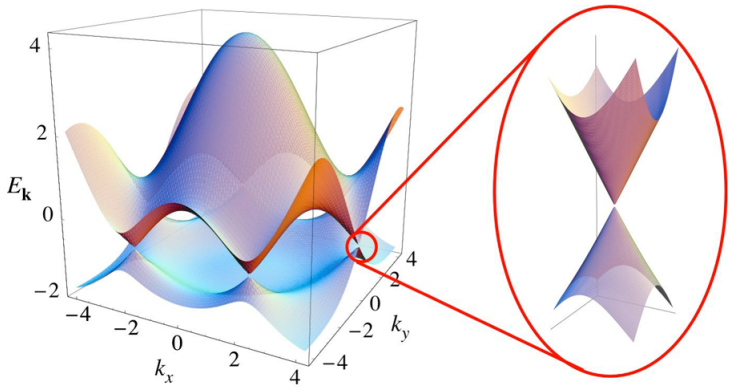


Figure 2.3: The electronic dispersion of graphene is shown. The figure is taken from [5]. The figure is plotted for $t$=2.7eV and $t'$=0.2$t$. The energy bands close to the Fermi level at one of the Dirac points has been zoomed in the inset.

has been plotted for $t$=2.7eV and $t'$=0.2$t$. The inset shows the so called Dirac point where the valence and the conduction band of graphene intersect at the $K$ and $K'$ points of the first Brillouin zone at the Fermi level. The Fermi velocity $v_f$ at the Dirac points was first calculated by [2] with the relation $v_f = 3ta/2$ and the value is $\simeq 1\times 10^6 m/s$. A detailed description of the tight binding approach and electronic properties of graphene can be found in [5, 6].

## 2.2 Graphene density of states

The electronic density of states is a very useful quantity in understanding several properties such as the electronic transport in diffusive regimes, excited states, bonding character, etc. Here $\rho(\varepsilon)d\varepsilon$ counts the number of quantum states in the interval $d\varepsilon$. The total number of states below $\varepsilon$ is given by

$$N(\varepsilon) = A \int_{-\infty}^{\varepsilon} d\varepsilon' \rho(\varepsilon') \tag{2.13}$$

where $A$ is the total surface area. The derivative with respect to energy gives

$$\rho(\varepsilon) = \frac{1}{A} \frac{\partial N(\varepsilon)}{\partial \varepsilon} \tag{2.14}$$

At the vicinity of the Dirac point, due to isotropy of the energy dispersion, the density of states is approximated to

$$\rho(\varepsilon) = \frac{g|\varepsilon|}{2\pi\hbar^2 v_f^2} \tag{2.15}$$

for $|\varepsilon| \ll t$. Here $v_f$ is the Fermi velocity and the factor $g$ takes into account the degeneracy arising from the internal degrees of freedom. The value of $g$ for graphene is 4 because of the two fold valley degeneracies and two electron spin induced ones. We therefore see that the density of states vanishes linearly at zero energy (at the Fermi level) [2, 7]. This linearity of the DOS around the Fermi level is a consequence of the linear dispersion at the Dirac point and is unique to graphene giving rise to its several interesting properties. A density functional theory calculation of the electronic graphene density of states with its projection on $s$,$p_z$ and $p_x + p_y$ orbitals are plotted in figure 2.4. We see that $p_z$ contributes to states close to the Dirac point at the Fermi level and that the DOS vanish altogether at the Dirac point. This corresponds to the $K$ point in the first Brillouin zone. The singularities (saddle points) that occur on either sides of the $K$ point are a result of van-Hove singularities which correspond to the $M$ points of the first

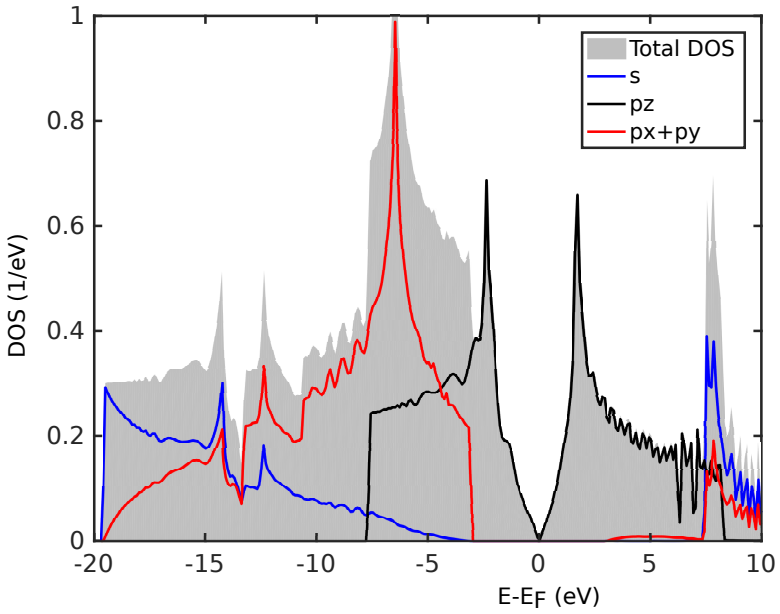


Figure 2.4: The density of states for graphene showing the orbital contributions are plotted. The linear dispersion of the $p_z$ orbital at the Fermi level shows the Dirac point.

Brillouin zone.

## 2.3 Experimental graphene band structure

Angle resolved photo-emission spectroscopy (ARPES) is often used to determine the energy dispersion relation of solids. This technique involves the detection of direction and energy of a photo-electron which is emitted from a sample due to well defined optical excitations. The energy bands and energy surfaces computed from ARPES measurements of single layer graphene grown on (0001) surface of SiC was performed by Bostwick *et. al.* [8]. Figure 2.5 (a) shows the $\pi$ band of graphene which is in good agreement with that previously calculated [5]. Figure

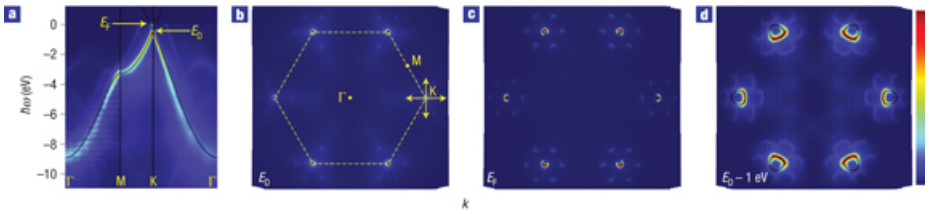


Figure 2.5: The energy dispersion relation of epitaxial graphene from ARPES measurements is taken from [8]. (a) The π band of graphene, (b) The energy dispersion at zero energy forming the first Brillouin zone, (c) Energy cut -1 eV away from the Dirac point and (d) The trigonal warping of the Fermi energy surface.

2.5 (b) shows the section of the energy dispersion at zero energy forming the first Brillouin zone. The energy cut at the Fermi energy ($E_f \approx 0.45$eV) showing a circular Fermi surface at the $K$ and $K'$ points of the first Brillouin zone are seen in Figure 2.5 (c) and the energy cut at -1 eV away from the Dirac point is shown in Figure 2.5 (d). At this energy the trigonal warping of the Fermi surface is clearly seen.

## 2.4 Properties of graphene

The rapid inclusion of graphene in current technology is due to its unique properties that we are going to outline in this section. Since its discovery in 2004, this 2-D allotrope of carbon has generated a lot of research interest because single layer graphene, few layer graphene and graphene oxide show very unusual properties.

### 2.4.1 Chemical properties

Due to the 2-D structure of graphene, it is the only allotrope of carbon available for chemical reactions from two sides. A single layer of graphene is found to be a hundred times more chemically reactive than few/many layer graphene [9]. The boundaries of these 2-D sheets have an interesting chemical reactivity with a very high ratio of edge atoms. Defects and doping of graphene sheets is found to increase its chemical reactivity significantly [10]. Graphene burns at considerably low temperatures of 620K [11] and its reaction temperature with oxygen is 530K [12]. Controlled doping graphene with oxygen [13] and nitrogen [14] also show very interesting properties and have been extensively studied.

### 2.4.2 Electronic properties

Graphene is a zero bandgap semi-metal where its valence and conduction bands touch at the Fermi level corresponding to the $K$ and $K'$ points of the first Brillouin zone forming the so called Dirac cone. This was theoretically obtained in the previously section from tight binding calculations. Consequently, electrons propagating through graphene behave as massless Dirac Fermions and the dispersion close to one of the Dirac points is essentially $E(q) = \pm v_F|q|$, where $q$ is measured from the Dirac point[5, 15]. Graphene therefore displays remarkable electron mobility at room temperature with values in excess of 15,000 $\mathrm{cm^2V^{-1}s^{-1}}$ [16]. The charge carriers (electrons and holes) show very similar mobilities which are nearly independent of temperature within the range of 10K to 100K [15, 17, 18, 19]. Such a high mobility would imply that the dominant scattering mechanism in graphene is by defect scattering. Acoustic phonons limit the mobility of charge carriers in graphene at room temperature, but the reported mobility is still $10\times10^6$ times larger than in copper [19, 20].

The quantum Hall effect is a quantum mechanical extension of the classical Hall effect where there is a production of a current perpendicular to the direction of the main current in the presence of a magnetic field. The Hall effect $\sigma_{xy}$ is quantized in terms of integer multiples of $e^2/h$ (where $e$ is electronic charge and $h$ is the Planck's constant)at low temperatures and high magnetic fields. Graphene shows an interesting phenomenon called anomalous quantum Hall effect where the quantization of Landau levels are shifted by 1/2 with respect to the standard sequence and with an additional factor of 4. The quantum Hall conductivity of graphene $\sigma_{xy} = \pm 4(N + 1/2)e^2/h$ where $N$ is the Landau levels and the double valleys and spin degeneracies gives a value 4 [16]. These anomalies are even seen at near room temperatures (293 K) [17, 21, 22].

### 2.4.3 Mechanical properties

Graphene is the strongest material ever tested with an intrinsic tensile strength of 130 GPa and a Young's modulus of 1 TPa [23]. Even upon extreme strain and distortion, graphene continues to show mechanical robustness and does not significantly affect its excellent charge carrier mobility [24]. The spring constant of graphene is measured using atomic force microscopy by suspending graphene over $SiO_2$ cavities and the value was found to be in the range of 1-5 N/m and the stiffness being 0.5 TPa [23, 25]. These properties lead to several interesting applications in nano-electro mechanical systems (NEMS) like pressure sensors and resonators [26]. Another important mechanical attribute of graphene is the rippling caused by thermal and quantum fluctuations. Usually in 3-D materials these fluctuations are bound, but according to Mermin-Wagner theorem [27], it is shown that as the system approaches 2-D scales, the amplitude of these fluctuations grow

logarithmically. It was thus believed that sufficiently large 2-D materials would crumple to form a more stable 3-D structure. It has been observed that suspended graphene indeed shows these thermal fluctuations and as a consequence of these dynamical deformations [28], there has been some debate on whether graphene is indeed truly 2-D [16, 29, 30, 31, 32]. But these ripples, which are enhanced by defects, can lead to negative Poisson's ratio in graphene [33].

### 2.4.4 Magnetic properties

Pristine graphene has no intrinsic magnetism in the ground state. This is due to the bipartite lattice structure which is explained by the two theorems of Lieb [34]. The first theorem proves that in an attractive Hubbard model, the ground state has a zero spin angular momentum ($S$=0) for every even electron filling. In a repulsive scenario, when the lattice structure is bipartite and the bands are half filled, the ground state $S$=$\frac{1}{2}$ $||B|-|A||$, where $|B|$ ($|A|$) are the number of sites in the sublattice sites B(A). In the ground state, both these cases are unique. The second theorem confirms that when $|B| = |A|$ the system is non-magnetic and when $|B| \neq |A|$, the solution leads to a ferromagnetic state. These theorems hold in all dimensions even for systems without periodic lattice. In graphene, the two inequivalent carbon atoms prefer opposite spin occupancies and the total magnetic moment is zero. There have been several methods proposed to induce magnetism in graphene. Creating structural vacancies or surface defects [35, 36, 37, 38, 39]and polarized edge states [40, 41, 42] have shown to induce magnetism in graphene. But these methods destroy the crystalline integrity of graphene and proves to be experimentally challenging to maintain the induced magnetism during device fabrication [43]. For these reasons recent studies about partial hydrogenation of graphene [44, 45] and covalent adsorption of organic molecules on graphene [46, 47, 48] and more

recently graphene nanoridges with oriented fluorine chains [49] has attracted a lot of attention.

## 2.5 Experimental graphene synthesis techniques

There has been increasing research interest in the experimental community to produce good quality, commercially viable graphene due to its unique properties and its several potential applications. Production of single layer graphene in large scale has been challenging due to thermodynamic barriers that need to be surmounted in order to create large scale 2-D materials. A hint on how one can find a way around this problem is is eloquently written in one of the articles by Andrey Geim [50] drawing references to Edwin Abbott's well known *novella Flatland: A Romance of Many Dimensions* as:
*Fundamental forces place seemingly insurmountable barriers in the way of creating [2D crystals]... The nascent 2D crystallites try to minimize their surface energy and inevitably morph into one of the rich variety of stable 3D structures that occur in soot.*

But there is a way around the problem. Interactions with 3D structures stabilize 2D crystals during growth. So one can make 2D crystals sandwiched between or placed on top of the atomic planes of a bulk crystal. In that respect, graphene already exists within graphite... One can then hope to fool Nature and extract single-atom-thick crystallites at a low enough temperature so that they remain in the quenched state prescribed by the original higher-temperature 3D growth.

Some of the current experimental techniques are detailed in the following sec-

tions.

### 2.5.1 Exfoliation

The earlier methods of exfoliation involved cleaving multilayer graphite into single layers of graphene [51]. As of 2014, graphene produced via exfoliation is found to produce graphene layers with least number of defects and high electron mobility [52].

#### Scotch tape method

Andre Geim and Konstantin Novoselov cleaved graphite using adhesive tape for the first time in 2004. To get single layer graphene, they repetitively cleaved graphite and the resulting single layer graphene was deposited on a silicon wafer [51].

#### Wedge based techniques

This method was discovered by a group of Indian scientists,where highly ordered pyrolytic graphite (HOPG) is cleaved using a sharp single crystal diamond head to create ordered graphene flakes [53]. These experiments were also supported by molecular dynamics simulations [54].

#### Shearing

Unoxidized graphene can be prepared from graphite using mixers which produce high local shear rates (greater than $10\times10^4$). This method was claimed to be applicable for creating other 2-D layered materials like Boron Nitride and Molybdenum disulfide [55].

### 2.5.2 Epitaxial route

Epitaxy refers to the lattice matching influenced mainly by the crystalline registry when one deposits a crystalline overlayer over a crystalline substrate. The properties of epitaxially grown graphene are significantly influenced by the underlying substrate. Graphene which strongly interacts with the substrate (like nickel (111)) loses its Dirac cone and opens a bandgap in graphene [56]. Surfaces which weakly interact with graphene via van der Waal's forces (like silicon carbide) are found to preserve the Dirac cone and graphene retains its unique electronic properties [1].

#### Silicon Carbide (SiC)

SiC upon heating to temperatures greater than 1100 $^{\circ}C$ and low pressure ($\sim 10^{-6}$ Torr) reduces to graphene. This process produces epitaxial graphene whose thickness, charge density and mobility depends on whether the reduction takes place in a silicon terminated or carbon terminated faces [57]. Graphene interacts via van der Waal's forces with SiC and the band structure and Dirac cone of graphene was first visualized on this material [58, 59, 60]. Graphene which has been grown in this way can further be patterned according to device requirements by using standard microelectronic methods [61].

### 2.5.3 Metal substrates

Growth of graphene on various metal substrates using chemical vapour deposition techniques are found to produce uniform and clean graphene. We shall summarize the growth of graphene on a few metals. Graphene grown on ruthenium is found to be undulated and of non-uniform thickness. This causes graphene to be rippled and affects its electronic properties [62]. Graphene interacts weakly with Iridium to produce highly ordered, rippled overlayers with uniform thickness. Graphene

shows long range order on this metal and retains the Dirac cone [63]. An important factor that effects the growth of graphene on metals is the lattice mismatch. Graphene has the closest lattice matching with the nickel(111) surface and interacts strongly with the $d_{z^2}$ orbitals of the metal. This leads to a clean, unrippled graphene with a bandgap opened at the Fermi level [64]. Some of the methods employed to create high quality few layer graphene sheets exceeding 1 $cm^2$ on nickel surface are discussed here. First the film is exposed to Argon at 900-1000 $^{\circ}$C. Methane is then injected into the chamber which disassociates and the carbon atoms of methane diffuse into nickel. The carbon when cooled disperses from the metal forming ordered graphene sheets [65, 66, 67]. Another method uses temperatures similar to conventional transistor processing using a nickel alloy and gold catalyst. This process also dissolves carbon into the transition metal at high temperatures and as the system is cooled the carbon diffuses to the surface forming single layer graphene [68]. A more detailed description of graphene on nickel (111) is reviewed in chapter 6. Copper at room temperatures and low pressures, in the presence of trace amounts of methane, form high quality single layer graphene. The growth mechanism here is associated with the separation of carbon from methane rather than diffusion of carbon from the metal as seen in the previous case [66, 69].

## 2.6 Graphene in electronics

Owing to high charge carrier mobility and low noise, graphene could be an ideal candidate for channels in field effect transistors. In 2008, the smallest transistor which was one atom thick and $<$10 nm in size was made [70]. IBM fabricated and characterized a graphene transistor in the GHz frequency. This opened up

avenues for the creation of both n and p type transistors [71] and consequently the first graphene integrated inverter comprising of these two types of transistors was fabricated [72]. IBM later went on to build 100 GHz processors on 2 inch graphene sheets [73]. In 2011 they went on to create the first graphene based integrated circuit which was a broadband radio mixer [74]. Dispite these applications, the lack of bandgap in graphene inhibits its use in creating digital logic gates and digital switches. Efforts to induce a bandgap in graphene has been extensively studied by creating defects, or by covalent functionalization of graphene with other molecules [75]. Graphene based non-boolean circuits have also been fabricated taking advantage of the negative differential resistance resulting from the symmetric band structure [76].

Apart from induction of bandgap due to covalent functionalization of graphene, another important application which follows is the sensitivity of electronic properties of graphene to molecular adsorption. This makes graphene a suitable candidate for gas sensors [77, 78, 79, 80]. Its large surface to volume ratio, efficient electrical noise reduction and large exposure area increases the efficiency of these devices. Finally we recall that graphene is also an ideal candidate for transparent thin electrodes due to its high electrical conductivity and high optical transparency, required for applications like touch screens, organic photo-voltaic cells, liquid crystal displays, dye sensitized solar cells and organic light emitting diodes [81, 82, 83].

# Chapter 3

# Ground State Electronic Structure Theory

*Quantum physics thus reveals a basic oneness of the universe.*

*Erwin Schrödinger (12 August 1887 – 4 January 1961)*

In the swamp of materials available in nature and new materials being discovered and synthesized regularly, one of the fundamental aspects in understanding and synergizing their properties is the electrons in these materials. The electrons interact with other ones of their atom and also with electrons of their neighbours in a complex tango of physics which has been captivating researchers for decades. These interactions form the basis for chemical bonding and adsorption mechanisms, surface and interfacial interactions, electronic and magnetic properties and several other fundamental effects associated with matter. In this chapter we shall summarize the basic theory and methods for determining the electronic structure of materials.

## 3.1 Schrödinger's Equation

Erwin Schrödinger, in 1926, went on to formulate a general time dependent partial differential equation to describe hypothetical plane waves describing the motion of material points (which he called 'phase waves') [84],

$$i\hbar \frac{\partial}{\partial t}\psi(\mathbf{r},t) \;=\; \widehat{H}\psi(\mathbf{r},t) \qquad [\mathbf{r} \equiv \mathbf{r}_1, \mathbf{r}_2, ...] \tag{3.1}$$

where $\psi(\mathbf{r},t)$ is the many-body wave function and the Hamiltonian $\widehat{H}$ for a system in terms of the kinetic energy $\widehat{T}$ and potential energy $\widehat{V}$ operators can be written as

$$\widehat{H} = \widehat{T} + \widehat{V} \tag{3.2}$$

For an interacting $N$ particles in 3-D the Hamiltonian can be written as

$$\widehat{H} = -\frac{\hbar^2}{2} \sum_{i=1}^{N} \frac{1}{m_i}\nabla^2_{\mathbf{r}} + V(\mathbf{r}_1, \mathbf{r}_2..\mathbf{r}_N, t) \tag{3.3}$$

We assume that $V$ does not dependent on $t$ (Conservative system) and the corresponding Schrödinger equation reads

$$i\hbar \frac{\partial}{\partial t}\psi(\mathbf{r}_1, \mathbf{r}_2..\mathbf{r}_N, t) \;=\; \left[-\frac{\hbar^2}{2} \sum_{i=1}^{N} \frac{1}{m_i}\nabla^2_{\mathbf{r}} + V(\mathbf{r}_1, \mathbf{r}_2..\mathbf{r}_N)\right] \psi(\mathbf{r}_1, \mathbf{r}_2..\mathbf{r}_N, t) \tag{3.4}$$

The solution of a time dependent Schrödindger equation corresponds to stationary states or orbitals of energy $E$. This can be obtained by the variable-separable method where the spatial and the time dependent parts are separated from the wavefunction.

$$\psi(\mathbf{r}_1, \mathbf{r}_2..\mathbf{r}_N, t) = \psi(\mathbf{r}_1, \mathbf{r}_2..\mathbf{r}_N)\tau(t) = \psi(\mathbf{r}_1, \mathbf{r}_2..\mathbf{r}_N)e^{-iEt/\hbar} \tag{3.5}$$

This reduces the equation to the energy Eigen value times the wave function and its general form simplifies to an Eigen value problem as

$$E\psi(\mathbf{r}_1, \mathbf{r}_2..\mathbf{r}_N) = \widehat{H}\psi(\mathbf{r}_1, \mathbf{r}_2..\mathbf{r}_N) \tag{3.6}$$

The term wavefunction that has been repeatedly used deserves to be explained in more detail. An important postulate of quantum mechanics is that the (time dependent) wavefunction describes and contains all information about the state of a system. For simplicity we restrict our discussion for a time independent case. The Copenhagen interpretation of quantum mechanics subscribes to the Born probability interpretation of the wavefunction where the square of the wavefunction corresponds to the probability density.

$$|\psi(\mathbf{r}_1, \mathbf{r}_2..\mathbf{r}_N)|^2 d\mathbf{r}_1 d\mathbf{r}_2..d\mathbf{r}_N, \tag{3.7}$$

where equation 3.7 corresponds to particles 1,2,..$N$ located simultaneously within volume elements $d\mathbf{r}_1 d\mathbf{r}_2..d\mathbf{r}_N$ respectively. A consequence of the probability interpretation of the wavefunction is the normalization of the wavefunction. The normalization condition says that since the particles must exist somewhere in space and an integral of the volume over all space must result in the probability to be 1:

$$\int d\mathbf{r}_1 \int d\mathbf{r}_2 ... \int d\mathbf{r}_N \, |\psi(\mathbf{r}_1, \mathbf{r}_2..\mathbf{r}_N)|^2 = 1. \tag{3.8}$$

Equation 3.8 gives us a physical criteria the wavefunction must obey, which must normalize to one over the full spatial range and it must be square-integrable. Another property associated with the wavefunction is that when an operator acts on a wavefunction, the resultant expectation value should correspond to that observable for that wavefunction. For an observable $O(\mathbf{r}_1, \mathbf{r}_2..\mathbf{r}_N)$, the expectation value on a wavefunction is generally written as

$$\langle O \rangle = \int d\mathbf{r}_1 \int d\mathbf{r}_2 ... \int d\mathbf{r}_N \, \psi^*(\mathbf{r}_1, \mathbf{r}_2..\mathbf{r}_N) \widehat{O} \psi(\mathbf{r}_1, \mathbf{r}_2..\mathbf{r}_N) \tag{3.9}$$

## 3.2 Many electron systems

Most practical systems like atoms and molecules deal with charged particles like the electrons and nuclei. Setting $\hbar = m_e = e = 4\pi\varepsilon_0 = 1$ a general many body Hamiltonian for a system with $N$ electrons and $M$ nuclei, in the absence of electric or magnetic field, is written using equation 3.6 as

$$E_i\psi_i(\mathbf{r}_1,\mathbf{r}_2..\mathbf{r}_N,\mathbf{R}_1,\mathbf{R}_2..\mathbf{R}_M) = \widehat{H}\psi(\mathbf{r}_1,\mathbf{r}_2..\mathbf{r}_N,\mathbf{R}_1,\mathbf{R}_2..\mathbf{R}_M) \tag{3.10}$$

and the corresponding many body Hamiltonian is written as

$$\widehat{H} = -\frac{1}{2}\sum_{i=1}^{N}\nabla_i^2 \;-\; \frac{1}{2}\sum_{k=1}^{M}Z_k\nabla_k^2 \;-\; \sum_{i=1}^{N}\sum_{k=1}^{M}\frac{Z_k}{|\mathbf{r}_{ik}|} \;+\; \frac{1}{2}\sum_{i=1}^{N}\sum_{j>i}^{N}\frac{1}{|\mathbf{r}_{ij}|} \;+\; \frac{1}{2}\sum_{k=1}^{M}\sum_{l>k}^{M}\frac{Z_kZ_l}{|\mathbf{R}_{kl}|} \tag{3.11}$$

Here in equation 3.11, $Z_k$ refers to the atomic number of the $k^{th}$ nuclei, $\mathbf{r}_{ij} = |\mathbf{r}_i - \mathbf{r}_j|$, $\mathbf{r}_{ik} = |\mathbf{r}_i - \mathbf{R}_k|$ and $\mathbf{R}_{kl} = |\mathbf{R}_k - \mathbf{R}_l|$ which are the electron-electron, electron-nuclei and the internuclear distances. The first two terms of equation 3.11 correspond to the kinetic energies of the electron and nuclei respectively, and the latter three terms denote the electrostatic particle-particle interactions. Considering the Born-Oppenheimer approximation which says that since the nuclear mass is much larger than that of the electrons, we can consider the nuclear motion to be much slower than the electronic one so that the nuclei are spatially fixed. Therefore we can write an approximate electronic Hamiltonian as

$$\widehat{H}_{el} = -\frac{1}{2}\sum_{i=1}^{N}\nabla_i^2 \;+\; \sum_{i=1}^{N}\sum_{j>i}^{N}\frac{1}{\mathbf{r}_{ij}} \;-\; \sum_{i=1}^{N}\sum_{k=1}^{M}\frac{Z_k}{\mathbf{r}_{ik}}, \tag{3.12}$$

or in terms of operators

$$\widehat{H}_{el} \;=\; \widehat{T} \;+\; \widehat{U} \;+\; \widehat{V}. \tag{3.13}$$

Some observations from equations 3.12 and 3.13 is that the kinetic energy term $\widehat{T}$ and $\widehat{U}$ does not depend on the nuclear positions but only on the electron coordinates. The only part of the electronic Hamiltonian that depends on the atomic

positions is the electron-nuclear interactions $\widehat{V}$ which is system dependent. We shall denote the expectation value of $\widehat{V}$ as $V_{ext}$ which is the external potential that need to be specified depending on the system under study. As soon as the external potential is known, the next step would be to solve for $\psi_i$ and the solution contains all information regarding the system. Although this sounds straight forward, finding $V_{ext}$ for large systems is very challenging and over the years lot of research has been devoted to finding good approximations for this value.

## 3.3 Hartree Fock Approach

The Hartree-Fock method is the first *ab initio* method employed in electronic structure theory. The central idea of the Hartree-Fock approach is that the ground state of the system is described by a Slater determinant made up of single particle wavefunctions and the energy obtained from this ground state wavefunction $E_{trial}$ is an upper limit of the actual ground state energy of the system $E_0$, which after self-consistent minimization gives the best estimate of the true ground state energy.

$$E_{trial} \geq E_0 \tag{3.14}$$

The resulting many-electron wavefunction in Hartree-Fock can be written in terms of the lowest energy of the occupied single-electron wavefunction $\psi_i$ using the Slater determinant as

$$\psi(x_1, x_2, ...x_N) = \frac{1}{\sqrt{N!}} \begin{bmatrix} \psi_1(x_1) & \psi_2(x_1) & ... & \psi_N(x_1) \\ \psi_1(x_2) & \psi_2(x_2) & ... & \psi_N(x_2) \\ \vdots & & & \\ \psi_1(x_N) & \psi_2(x_N) & ... & \psi_N(x_N) \end{bmatrix} \tag{3.15}$$

Here the electron coordinates include the spatial coordinate $\mathbf{r}_i$ and the spin component $\xi_i$. The total wavefunction follows the Fermi-Dirac statistics and it is asym-

metric upon interchanging the electronic coordinates and vanishes if two electrons occupy the same state. To find the ground state energy of the system, we vary $\psi_i$ to minimise the expectation value of the Hamiltonian:

$$\begin{aligned}\langle\psi|\widehat{H}|\psi\rangle = &\sum_i \int dx\psi_i^*(x)\left[-\frac{1}{2}\nabla^2 + V_{ext}(\mathbf{r})\right]\psi_i(x) \\ &+ \frac{1}{2}\sum_{i,j}[\int dx \int dx'\psi_i^*(x)\psi_j^*(x')\frac{1}{\mathbf{r}_{ij}}\psi_i(x)\psi_j(x') \\ &- \int dx \int dx'\psi_i^*(x)\psi_j^*(x')\frac{1}{\mathbf{r}_{ij}}\psi_i(x')\psi_j(x)]\end{aligned} \tag{3.16}$$

Equation 3.16 can be minimized using Lagrangian multipliers from variational calculus as :

$$\delta(\langle\psi|\widehat{H}|\psi\rangle \; - \; \sum_i \varepsilon_i\langle\psi_i|\psi_i\rangle) \; = \; 0 \tag{3.17}$$

the right hand side of equation 3.17 reflects the normalization constraints of the single electron wavefunction. Substituting equation 3.16 in 3.17 and varying the wavefunctions :

$$\begin{aligned}&\sum_i \int dx\delta\psi_i^*(x)[-\frac{1}{2}\nabla^2 + V_{ext}(\mathbf{r})]\psi_i(x) \\ &+ \frac{1}{2}\sum_{i,j}[\int dx \int dx'\delta\psi_i^*(x)\psi_j^*(x')\frac{1}{\mathbf{r}_{ij}}\psi_i(x)\psi_j(x') \\ &+ \int dx \int dx'\psi_i^*(x)\delta\psi_j^*(x')\frac{1}{\mathbf{r}_{ij}}\psi_i(x)\psi_j(x') \\ &- \int dx \int dx'\delta\psi_i^*(x)\psi_j^*(x')\frac{1}{\mathbf{r}_{ij}}\psi_i(x')\psi_j(x) \\ &- \int dx \int dx'\psi_i^*(x)\delta\psi_j^*(x')\frac{1}{\mathbf{r}_{ij}}\psi_i(x')\psi_j(x)] \\ &-\sum_i \varepsilon_i \int dx\delta\psi_i^*(x)\psi_i(x) \; + \; c.c \; = \; 0\end{aligned} \tag{3.18}$$

The summations in equation 3.18 run over the occupied states and has to satisfy any variations of $\psi_i$'s, which implies that each single particle wavefunction must

satisfy:

$$\begin{aligned}[-\frac{1}{2}\nabla^2 + V_{ext}(\mathbf{r})]\psi_i(x) \; + \; \sum_j [\int dx' \psi_j(x')\psi_j^*(x')\frac{1}{\mathbf{r}_{ij}}\psi_i(x) \\ - \; \int dx' \psi_i(x')\psi_j^*(x')\frac{1}{\mathbf{r}_{ij}}\psi_j(x)] \; = \; \varepsilon_i\psi_i(x)\end{aligned} \tag{3.19}$$

This is the effective single-electron Schrödinger equation which, apart from the external potential also contains two more terms. One is the Hartree potential which is a result of the spread out charge density of the electrons:

$$V_H(\mathbf{r}) \; = \; \sum_j \; \int \; d\mathbf{r}' \psi_j(x')\psi_j^*(x')\frac{1}{\mathbf{r}_{ij}} \tag{3.20}$$

and the other term is the non-local exchange potential which is the consequence of the antisymmetric structure of the electronic wavefunction and operates in a non-local fashion on $\psi_i$ :

$$\int dx' V_x(x,x')\psi_i(x') \; = \; -\sum_j \int d\mathbf{r}' \psi_i(x')\psi_j^*(x')\frac{1}{\mathbf{r}_{ij}}\psi_j(x) \; \delta_{\sigma_i\sigma_j} \tag{3.21}$$

Which acts on electrons of the same spin. The expectation value of the Hamiltonian gives the ground state energy as:

$$\begin{aligned} E \; &= \; \langle\psi|H|\psi\rangle \\ &= \; \sum_i \varepsilon_i \; - \; \frac{1}{2}\sum_{i,j}[\int dx \int dx' \psi_i^*(x)\psi_j^*(x')\frac{1}{\mathbf{r}_{ij}}\psi_i(x)\psi_j(x') \\ &- \int dx \int dx' \psi_i^*(x)\psi_j^*(x')\frac{1}{\mathbf{r}_{ij}}\psi_i(x')\psi_j(x)]. \end{aligned} \tag{3.22}$$

In equation 3.22, $\varepsilon_i$ are the one-electron orbital energies following the Koopman's theorem and is corrected by subtracting the Hartree and the exchange energies appropriately to make up for the double counting of these interactions. We see that the Hartree and the exchange terms also depend on the wavefunctions and therefore one must start with a sensible guess of the initial trial wavefunction and solve the problem self consistently to find the ground state energy of the system.

Although this method is quite good in calculating the total energies and equilibrium geometries, there are certain limitations that arise from the approximations considered. Also one can see in equation 3.22 that the expectation value electron-electron Coulomb interaction consists of the exchange energy minus the Hartree energy. We also remark that in the Hartree-Fock method there are no terms to explain the correlation effects due to the dynamic electronic motion which further lowers the total energy. This remains a fundamental problem in many-electron physics and better methods and approximations are being developed to find these correlation effects.

## 3.4 Density Functional Theory

The fundamental principle of density functional theory (DFT) is that for a many particle system, all the ground state system properties can be viewed as functionals of its ground state density $n_0(\mathbf{r})$ [85, 86, 87, 88]. Although the formed proofs are given by the Hohenberg and Kohn theorems, they do not describe ways to obtain practical solutions. Kohn and Sham, in their ansatz [89], went on to supply a way to perform realistic calculations to approximate ground state functionals for practical many-electron systems. They replace the many-body interacting problem as an independent single particle one and include the many-body effects in the exchange-correlation functional. Although the exact form of these exchange-correlation functionals are not known, various approximations have been proposed to try and accurately describe them. In this section we describe these concepts and setup the fundamental theory for treating many-body systems in the ground state.

### 3.4.1 Thomas-Fermi approximation

The Thomas-Fermi model (TF), a precursor for modern Density functional theory was proposed by Thomas [90] and Fermi [91] in 1927. Although their approximations are not accurate enough for modern-day electronic structure calculations, they offer the general way in which DFT works. In the TF method, they assume a non-interacting homogeneous electron gas and propose a kinetic energy term which is a functional of this density. They also neglect the exchange and correlation interactions of the electrons (The exchange term was later included by Dirac as local approximations). The total energy functional for electrons in an external potential $V_{ext}(\mathbf{r})$ is given by:

$$\begin{aligned} E_{TF}[n] \;=\; C_1 \int d^3 r n(\mathbf{r})^{5/3} \;+\; \int d^3 r V_{ext}(\mathbf{r}) n(\mathbf{r}) \\ +\; C_2 \int d^3 r n(\mathbf{r})^{4/3} \;+\; \frac{1}{2} \int d^3 r d^3 r' \frac{n(\mathbf{r}) n(\mathbf{r}')}{|\mathbf{r}) - \mathbf{r}')|} \end{aligned} \tag{3.23}$$

where the terms $C_1 = \frac{3}{10}(3\pi^2)^{2/3}$ and $C_2 = -\frac{3}{4}(\frac{3}{\pi})^{1/3}$. The first term in equation 3.23 is the local approximation of the kinetic energy, the third term is the local exchange and the final term is the classic electrostatic energy. The ground state energy $n_0(\mathbf{r})$ can be found by minimizing the energy functional with a constraint that integrating the density over all space would give us the total number of electrons in the system $N$. Minimizing and using Lagrangian multiplier $\mu$ (which is the chemical potential) for small variations of density $\delta n(\mathbf{r})$,

$$\int d^3 r [\frac{5}{3} C_1 n(\mathbf{r})^{2/3} \;+\; V(\mathbf{r}) \;-\; \mu] \delta n(\mathbf{r}) \;=\; 0 \tag{3.24}$$

where $V(\mathbf{r})$ is the total potential which includes the external potential, the Hartree and exchange terms. This functional is said to be stationary if the density and potential terms of equation 3.24 satisfy the condition :

$$\frac{1}{2}(3\pi^2)^{2/3} n(\mathbf{r})^{2/3} \;+\; V(\mathbf{r}) \;-\; \mu \;=\; 0 \tag{3.25}$$

There have been extensions proposed to take into consideration the inhomogeneity of many-body systems, non-local exchange treatments by appropriate gradient corrections and correlation effects. To find $n(\mathbf{r})$ and $V(\mathbf{r})$ this equation is coupled to Poission's equation. Even with these considerations, the TF model starts with approximations that miss some essential physics like orbital structures of atoms and the bonding of molecules. But it shows promise for solving metallic systems with a homogeneous electron gas.

### 3.4.2 The Hohenberg-Kohn theorems

Density functional theory is based on the two theorems first proved by Hohenberg and Kohn in 1964 [86, 89].

**Theorem 1:** For any system of interacting particles in an external potential $V_{ext}(\mathbf{r})$, the potential $V_{ext}(\mathbf{r})$ is uniquely determined, except for a constant, by the ground state particle density $n_0(\mathbf{r})$.

**Corollary 1:** Since the Hamiltonian is thus fully determined, it follows that the many-body wavefunction for all states of the system are determined. Therefore all the properties of the system are completely determined from the ground state density $n_0(\mathbf{r})$.

From the first HK theorem, the implication is that it is not possible to have two different external potentials which differ from each other by more than a simple constant, to give rise to the same non-degenerate ground state density. Therefore the electronic density uniquely determines the external potential within a constant. The corollary also holds because the Hamiltonian is uniquely determined by the ground state density. Therefore the wavefunction of any state can be determined by solving the Schrödinfger with the appropriate Hamiltonian. Among these solutions, the unique ground state solution will be the one with the lowest energy. The

theorem 1 just proves that the external potential is unique to the electron density but it still does not offer the solution to solving the many-body problem.

**Theorem 2:** For any valid external potential $V_{ext}(\mathbf{r})$, a universal functional for energy $E[n]$ can be defined in terms of the density $n(\mathbf{r})$. For any particular $V_{ext}(\mathbf{r})$,the global minimum value of this functional is the exact ground state energy of the system and the corresponding density which minimizes this functional is the exact ground state density $n_0(\mathbf{r})$.

**Corollary 2:** The knowledge about the universal functional $E[n]$ (which is same for all electron systems and independent of the external potential), is alone sufficient in determining the exact ground state energy and density of the system.

A point to note is that this functional $E[n]$ only determines the ground state properties of the system and not the excited state ones.

The total energy functional can be written as :

$$E[n] \;=\; F_{HK}[n] \;+\; \int v_{ext} n(\mathbf{r}) d\mathbf{r} \tag{3.26}$$

$$F[n] \;=\; \langle \psi | T + V_{ee} | \psi \rangle \quad (\textit{is a universal functional}) \tag{3.27}$$

Some of the limitations of DFT from the Hohenberg-Kohn theorems is that, even though they prove that there exists an exact solution of the many-body problem, they provide no guidance to determine the exact nature of this functional. Their premise is predicated on finding this functional which is dependent on the electronic density and from that, derive all the system properties. The kinetic energy term in the HK functional is a many-body interacting term and there is no known way to go directly from the electronic density to the exact many-body kinetic energy.

### 3.4.3 The Kohn-Sham approach

The Kohn-Sham (KS) approach was formulated to replace a difficult interacting many-body system with an alternative approach of many independent particle equations that can be solved in principle with all the difficult many-body interaction terms swept under the umbrella of an exchange-correlation functional of the electronic density [92]. By solving these equations one gets the ground state density and energy whose accuracy is limited only by the approximations used for the exchange-correlation functional. Some of these approximations like local density approximation (LDA) and generalized gradient approximation (GGA) accurately describe many weakly correlated systems like semiconductors, sp-bonded metals like Na and Al, some insulators and covalent/ionic bonding in molecules. However these approximations fail to describe strongly correlated materials. This has led to a strong interest improving these approaches and find better approximations for tackling strongly correlated electron systems. The Kohn-Sham approach rests mainly on the following assumption:

1. The exact ground state density of a system of $N$ interacting particles can be represented as an auxiliary system of $N$ non-interacting particles having the same ground state charge density, with an additional exchange-correlation functional of density which includes the various many-body interactions.

The set of Kohn-Sham single particle equations which is subject to an effective local potential $V_{KS}(\mathbf{r})$, such that the ground state electronic density of an interacting system equals the non-interacting system is written as:

$$[-\frac{1}{2}\nabla^2 + V_{KS}(\mathbf{r})]\phi_i(\mathbf{r}) = \varepsilon_i\phi_i(\mathbf{r}) \quad i = 1...N \tag{3.28}$$

and

$$n(\mathbf{r}) \;=\; \sum_{i=1}^{N} |\phi_i(\mathbf{r})|^2 \tag{3.29}$$

The next task is to construct the KS potential $V_{KS}(\mathbf{r})$ for the ground state electronic density $n(\mathbf{r})$ of an interacting system. This is done using the variational principle of energy as explained in the second HK theorem. The energy functional can be written as follows:

$$E[n(\mathbf{r}] \;=\; T_s[n(\mathbf{r})] \;+\; E_H[n(\mathbf{r})] \;+\; E_{xc}[n(\mathbf{r})] \;+\; \int V_{ext}(\mathbf{r}) n(\mathbf{r}) d\mathbf{r} \tag{3.30}$$

Here $T_s[n(\mathbf{r})]$ is the kinetic energy functional of the non-interacting electrons:

$$T_s[n(\mathbf{r})] \;=\; -\frac{1}{2}\sum_i \int \phi_i^*(\mathbf{r}) \nabla^2 \phi_i(\mathbf{r}) d\mathbf{r}. \tag{3.31}$$

The term $E_H[n(\mathbf{r})]$ is the Hartree functional which considers the electrostatic interactions as:

$$E_H[n(\mathbf{r})] \;=\; \frac{1}{2}\int \frac{n(\mathbf{r}) n(\mathbf{r}')}{|\mathbf{r}-\mathbf{r}'|} d\mathbf{r} d\mathbf{r}' \tag{3.32}$$

and the exchange-correlation term $E_{xc}[n(\mathbf{r})]$ which contains the rest of the many-body interactions. By computing the derivatives of each of these terms from the energy functional, one can write them in terms of the potentials. The effective KS potential is a combination of the external potential $V_{ext}(\mathbf{r})$, the Hartree term $V_H(\mathbf{r})$ and the exchange-correlation term $V_{xc}(\mathbf{r})$ and is written as:

$$V_{KS}(\mathbf{r}) = V_{ext}(\mathbf{r}) + V_H(\mathbf{r}) + V_{xc}(\mathbf{r}). \tag{3.33}$$

The exchange-correlation potential is the derivative of the exchange correlation functional with respect to the electronic density:

$$V_{xc}(\mathbf{r}) = \frac{\delta E_{xc}[n(\mathbf{r})]}{\delta n(\mathbf{r})}. \tag{3.34}$$

The term $E_{xc}[n(\mathbf{r})]$ contains all the many-body interactions such as the dynamic inter-electron Coulombic interactions and the many-electron dynamic kinetic energy correction. A few points to note about the Kohn-Sham setup is that the equation is derived from the variational principle and can be solved self-consistently.

It is important to stress that the Kohn-Sham eigenvalues are not the true eigen energies of a many body system since Koopman's theorem is not valid in DFT. However often the eigenvalues and eigenfunctions are good approximation to the quasi particles, but the physical quantity in DFT is the charge density.

### Local Density Approximation

The Local Density Approximation (LDA) was introduced by Kohn-Sham in 1965 to approximate the exchange-correlation functional. They approximated the exchange-correlation energy functional by introducing an exchange-correlation energy for a homogeneous electron gas $E_{xc}[n(\mathbf{r})]$ which locally depends on the electronic density $n(\mathbf{r})$.

$$E_{xc}[n(\mathbf{r})] \;=\; \int \varepsilon_{xc}(n(\mathbf{r}))n(\mathbf{r})d\mathbf{r}. \tag{3.35}$$

Further,

$$\frac{\delta E_{xc}[n(\mathbf{r})]}{\delta n(\mathbf{r})} \;=\; (\varepsilon_{xc}(n(\mathbf{r})) + \frac{\partial \varepsilon_{xc}(n(\mathbf{r}))}{\partial n(\mathbf{r})}) \tag{3.36}$$

and the corresponding approximation for the LDA exchange potential is**cite**:

$$V_x[n(\mathbf{r})] \;=\; -\frac{e^2}{\pi}[3\pi^2 n(\mathbf{r})]^{1/3}. \tag{3.37}$$

### Local Spin Density Approximation

So far we have not considered the electronic spin while deriving the KS equations. But DFT can also be extended to include the ground state properties of spin-polarized systems. The electronic density here can be divided into two parts depending on the electronic spins, $n \;=\; n_\downarrow + n_\uparrow$ and the energy is a functional of both these spin components $E = E[n_\downarrow, n_\uparrow]$. Therefore the exchange correlation functional in the local spin density approximation (LSDA) can be written as:

$$V_{xc}^{LSDA} \;=\; \int n(\mathbf{r})\varepsilon_{xc}(n_\downarrow(\mathbf{r}), n_\uparrow(\mathbf{r}))d\mathbf{r} \tag{3.38}$$

where $\varepsilon_{xc}$ is the exchange-correlation energy per particle in a system of homogenous electron gas.

#### Generalized Gradient Approximation

An improvement over the LDA is the generalized gradient approximation (GGA) where the gradient of the density is also considered in the exchange correlation energy functional. GGA is found to considerable improve the total energies, energy barriers and structural energy changes when compared to LDA. The exchange-correlation energy in GGA, which is the function of the electronic density and its gradient is written as:

$$E_{xc}[n(\mathbf{r})] \;=\; \int f_{xc}(n(\mathbf{r}), \nabla n(\mathbf{r}))d\mathbf{r} \tag{3.39}$$

Here $f_{xc}$ is a dimensionless, parametrized analytic function of the electronic density and its gradient. The choice of this function must be done with care since it is not derived from a physical system. Numerous forms of this function have been proposed by the three widely used ones are Becke (B88) [93], Perdew and Wang (PW91) [94] and Perdew, Burke and Enzerhof (PBE) [95, 96]. For short ranges these three functionals are quite similar, but for longer ranges, B88 and PW91 give spurious exponential decay interactions. Some of these limitations are overcome in PBE by considering a real space grid cutoff for the exchange-correlation hole and avoids these long range second order gradient expansions of density.

### 3.4.4 Non-local dispersive corrections

Inclusion of non-local dispersive interactions are paramount in describing efficiently numerous physical, chemical and biological systems. Various approximations within DFT have been proposed to treat these critical, yet subtle, van der Waal's interactions. Some of the approaches suggested are semi-empirical

corrections [97, 98, 99, 100, 101, 102, 103], non-local correlation functionals [104, 105, 106, 107, 108], double hybrid functionals [109, 99, 110] and extensions proposed with the random phase approximations [111, 112]. In this section we shall discuss about Grimme correction [99] and Klimes, Bowler and Michaelides (vdW-KBM) non-local functional [113].

### Grimme correction

The backbone of semi-empirical corrections is the addition of a non-local energy correction term ($E_{disp}$) on the Kohn-Sham DFT energy ($E_{KS}$) as

$$E_{DFT+disp} = E_{KS} + E_{disp} \tag{3.40}$$

The semi-empirical correction term is given by :

$$E_{disp} = -s_6 \sum_{i=1}^{N_{at}-1} \sum_{j=i+1}^{N_{at}} \frac{C_6^{ij}}{R_{ij}^6} f_{dmp}(R_{ij}). \tag{3.41}$$

Here $N_{at}$ is the number of atoms in the system, $C_6^{ij}$ is the dispersion coefficient of the pair-wise atomic interactions $ij$, $s_6$ is a global scaling factor and $R_{ij}$ is an interatomic distance. A damping factor $f_{dmp}$ is added to prevent the divergence of the term for small values of $r$ and can be expanded as:

$$f_{dmp}(R_{ij}) = \frac{1}{1+e^{-d(R_{ij}/R_r-1)}} \tag{3.42}$$

where $R_r$ is the atomic vdW radii. Within the formalism, the dispersion coefficient $C_6^{ij}$ determines the strength of the dispersion interactions and it has be systematically extracted based on the local environment. An advantage of these corrections is that it does not burden the computational process but the corrections become inaccurate for long range soft matter and van der Waal complexes [114].

### Non-local functionals

Inclusion of van der Waals non-local interactions within the exchange-correlation functional of DFT has been a topic of active research. In this regard, a non-local correlation energy term $E_{xc}$ is included in the conventional exchange correlation term of DFT as:

$$E_{xc} = E_x^{GGA} + E_c^{LDA} + E_c^{nl}, \tag{3.43}$$

where $E_x^{GGA}$ and $E_c^{LDA}$ are the conventional GGA exchange term and LDA correlation term within DFT and $^{nl}_{c}$ is the non-local correlation term included [113]. The simplest form of this non-local term can be written in terms of the density as [105]:

$$E_c^{nl} = \frac{1}{2}\int d^3r d^3r' n(\mathbf{r})\phi(\mathbf{r},\mathbf{r}')n(\mathbf{r}'), \tag{3.44}$$

where $\phi(\mathbf{r},\mathbf{r}')$ is some given function which depends on $\mathbf{r}-\mathbf{r}'$. We describe the derivation proposed by Dion et. al. [105] where they initially start by dividing the correlation energy into two components:

$$E_c[n] = E_c^0[n] + E_c^{nl}[n]. \tag{3.45}$$

They treat the non-local term in full potential approximation and derive the non-local correlation as:

$$E_c^{nl} = \int_0^\infty \frac{du}{2\pi} tr[ln(1-V\chi) - ln\varepsilon], \tag{3.46}$$

where $\chi$ contains the density response to a self consistent potential, $V$ is the interatomic Coulomb interaction, $\varepsilon$ is the dielectric function and $u$ is an imaginary frequency term. For our calculations we use the KBM functional [113] which builds upon the platform of [105] by introducing appropriate choices on the GGA exchange component along with the correlation components prescribed by [105].

### 3.4.5 Pseudopotentials

The fundamental idea of a pseudopotential (PP) is to replace the effect of the ionic interaction of the nucleus and the presence of core electrons by an ambient interaction of these entities as felt by the valence electrons. This approximation can be used to compute the electronic properties of valence electrons of solids and molecules since the core levels remain relatively unchanged. Detailed reviews on the evolution of PP techniques can be found in [115, 116, 87]. The motivation for using the PP method is to reduce the size of the basis set, reduction of the number of electrons involved in the calculation and include relativistic effects. The main assumption made here is that the wavefunctions of the core level electrons overlap negligibly with that of the valence electrons. There are two commonly used forms of PP- the norm conserving PP and ultrasoft PP. We here describe the fundamentals of ultrasoft PP since it is mainly used in our calculations.

#### Ultrasoft pseudopotentials

One of the main goals of PP is to simulate pseudofunctions that are "smooth" without compromising on the accuracy. In plane wave calculations, the valence electron descriptions are expanded in terms of Fourier components and cost for a calculation scales as a power of these components. Therefore one such method to increase the "smoothness" of the process is to minimize the Fourier space needed to address these valence electrons for a given accuracy. Norm conserving PP techniques strive to improve the accuracy of the calculation by forgoing some "smoothness" In the Ultrasoft PP technique (USP), accuracy is reached by transforming the problem in terms of smooth functions and an additional auxiliary function which rapidly varying ion-core. This was proposed by Vanderbilt [117] where the difference between the all electron $\phi_{R,i}$ and pseudo reference states $\tilde{\phi}_{R,i}$ on atom $R$ can be written as:

$$q_{R,ij} = \langle \phi_{R,i} | \phi_{R,j} \rangle - \langle \tilde{\phi}_{R,i} | \tilde{\phi}_{R,j} \rangle. \tag{3.47}$$

Therefore with reference to the atomic states $R$, these smooth pseudo functions $\tilde{\psi}$ ($\phi = r\psi$)are solutions to a generalized eigenvalue problem as:

$$\widehat{H}|\psi_i\rangle = \varepsilon_i \widehat{S}|\psi_i\rangle \tag{3.48}$$

with $\widehat{H}$ being the Hamiltonian and $\widehat{S}$ being the overlap operator which is written as:

$$\widehat{S} = 1 + \sum_{R,i,j} |p_{R,i}\rangle q_{R,i,j} \langle p_{R,j}|. \tag{3.49}$$

Here $p_{R,i}$ are projectors which form the basis for the pseudo reference states within the cut-off radius and zero outside.

Pseudopotentials for most of the commonly used elements are generally available on pre-generated databases. The three main steps to generate a PP are:
First one generates the atomic levels and orbitals within DFT where the atomic state is defined by the electronic configuration, the one electron states defined by the principle quantum number and angular quantum number and obtained by self-consistent solution of KS equation. The second and third steps involves the generation of the PP from the atomic results and checking the relevance of the constructed PP. These two steps involve a lot of arbitrariness and done by trial and error methods. A full core hole pseudopotential generation follows a similar route. When one generates the atomic states of a FCH PP, one considers an additional electron in the valence of the system and a corresponding hole in the core level as specified in the electronic configuration of the interested element. In this thesis we use a pre-generated PP with a core-hole created in the 1s core shell of the nitrogen atom.

## 3.5 Non-equilibrium Green's Functions

Non-equilibrium Green's function methods have been extensively used to study electronic transport through molecular junctions to predict nanoscale devices. Although the applications of Green's function techniques have ramifications through various fields of physics, we introduce the it here to mainly arrive at the DOS of a system. This is because our main focus is the theoretical treatment of the charge transfer lifetime which can be extracted from the coupling of the molecular orbitals at the interface. This coupling is reflected in the DOS of the system and the Green's function technique allows us to simulate a semi-infinite bulk (by the introduction of the self-energy operators) to accurately calculate the intrinsic Lorentzian molecular linewidth. We consider a zero-bias system with the main intention of understanding the coupling of a molecular orbital with the semi-infinite bulk substrate states. The consequent determination of the charge transfer lifetime will be discussed in detail in the next chapter. Appendix A contains a brief description of SIESTA, an electronic transport code used to treat our systems.

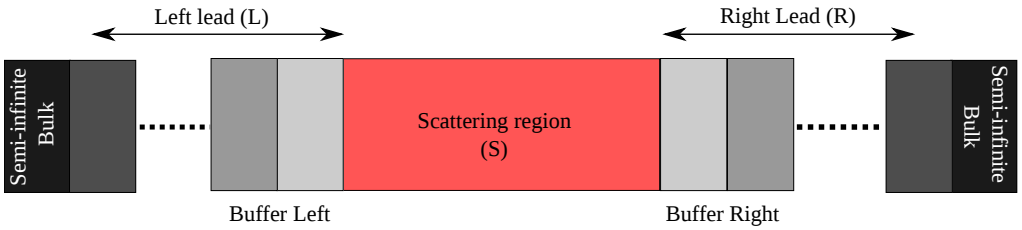


Figure 3.1: The typical setup for studying electron transport consists of a central scattering region (S) connected to two leads on either side (L and R). These leads are periodic images of the buffer regions and are coupled to a semi-infinite bulk substrate.

Suppose we divide the system of interest into three parts-The central scattering

region (S) which is sandwiched between two buffer regions connected to the two semi-infinite bulk leads (L and R) as shown in figure 3.1. We assume that the leads are perfect conductors and the electrons move ballastically in these regions. The electrons are scattered only due to the potential of the scattering region. The Hamiltonian and wavefunctions of the contacts are $H_{L,R}$ and $|\Psi_{L,R}\rangle$ respectively and that of the scattering region is $H_S$ and $|\Psi_S\rangle$. The equation of the system can be concisely represented in a matrix form of a Schrödinger equation as:

$$\begin{bmatrix} H_L & \tau_L & 0 \\ \tau_L^\dagger & H_S & \tau_R^\dagger \\ 0 & \tau_R & H_R \end{bmatrix} \begin{bmatrix} |\Psi_L\rangle \\ |\Psi_S\rangle \\ |\Psi_R\rangle \end{bmatrix} = E \begin{bmatrix} |\Psi_L\rangle \\ |\Psi_S\rangle \\ |\Psi_R\rangle \end{bmatrix} \tag{3.50}$$

where $\tau_{L,R}$ are the hopping parameters which describe the interaction between the leads and the scattering region. We assume that these hopping terms are not related to each other and there is no cross over terms between the left and right leads. The Green's function is defined as [118, 119] :

$$(E-H)G(E) \;=\; I \tag{3.51}$$

The Green's function gives the response of a system in the presence of a constant perturbation $|\nu\rangle$ in the Schrödinger equation:

$$H|\Psi\rangle \;=\; E|\Psi\rangle \;+\; |\nu\rangle \tag{3.52}$$

The response to this perturbation in terms of the Green's function is written as:

$$\begin{aligned} (E-H)|\Psi\rangle \;&=\; -|\nu\rangle \\ |\Psi\rangle \;&=\; -G(E)|\nu\rangle \end{aligned} \tag{3.53}$$

For example, expanding the third row in equation 3.50, one gets:

$$\begin{aligned} H_R|\Psi_R\rangle + \tau_R|\Psi_S\rangle \;&=\; E|\Psi_R\rangle \\ (E-H_R)|\Psi_R\rangle \;&=\; \tau_R|\Psi_S\rangle \\ \Longrightarrow |\Psi_R\rangle \;&=\; g_R(E)\tau_R|\Psi_S\rangle \end{aligned} \tag{3.54}$$

Here $g_R$ is the Green's function of the isolated R lead and can be written as $(E - H_R)g_R = I$. One should note that for an infinite lead, there are two solutions to the Green's function: the retarded and advanced solutions which correspond to the outgoing and incoming waves in the contact region. The notation used for the following section is: The retarded Green's function is $G$ and the advanced Green's function is $G^\dagger$. The capital $G$ denotes the full Green's function and the subscripts correspond to the sub-lattices of over which the Green's function operates, for example, $G_R, G_S$. The lowercase $g$ corresponds to the Green's function of isolated infinite contacts.

### 3.5.1 Self-Energy

The Green's function of the scattering region can be independently calculated without determining the Green's function of the full system. From the definition of Green's function presented above, we can write the Green's functions of the sub-lattices as:

$$\begin{bmatrix} E-H_L & -\tau_L & 0 \\ -\tau_L^\dagger & E-H_S & -\tau_R^\dagger \\ 0 & -\tau_R & E-H_R \end{bmatrix} \begin{bmatrix} G_L & G_{LS} & G_{LR} \\ G_{SL} & G_S & G_{SR} \\ G_{RL} & G_{RS} & G_R \end{bmatrix} = \begin{bmatrix} I & 0 & 0 \\ 0 & I & 0 \\ 0 & 0 & I \end{bmatrix} \tag{3.55}$$

Expanding the second column, we can work out the three equations:

$$\begin{aligned} (E-H_L)G_{LS} - \tau_L G_S &= 0 \\ -\tau_L^\dagger G_{LS} + (E-H_S)G_S - \tau_R^\dagger G_{RS} &= I \\ (E-H_R)G_{RS} - \tau_R G_S &= 0 \end{aligned} \tag{3.56}$$

The first and the third rows of equation 3.56 can be modified as:

$$\begin{aligned} G_{LS} &= g_L \tau_L G_S \\ G_{RS} &= g_R \tau_R G_S \end{aligned} \tag{3.57}$$

Substituting 3.57 in the central equation of 3.56 and expanding, one obtains:

$$-\tau_L^\dagger g_L \tau_L G_S + (E - H_S)G_S - \tau_R^\dagger g_R \tau_R G_S \;=\; I \tag{3.58}$$

from which we can find the Green's function of the scattering region as:

$$G_S \;=\; (E \;-\; H_S \;-\; \Sigma_L \;-\; \Sigma_R)^{-1} \tag{3.59}$$

Where the terms $\Sigma_L \;=\; \tau_L^\dagger g_L \tau_L$ and $\Sigma_R \;=\; \tau_R^\dagger g_R \tau_R$ are the self-energies of the left and right contact regions respectively. From these self-energy terms, we account for the interactions of the semi-infinite leads with the central scattering region. We need to calculate these self energy terms ($g_{L,R}$) which can be done easily by assuming a periodic contact region and using bulk Green's function for the semi-infinite leads.

### 3.5.2 Spectral Function

Another important aspect of the Green's function is the Spectral function. It is defined as:

$$A \;=\; i(G - G^\dagger) \tag{3.60}$$

The function $A$ contains information regarding the density of states (DOS) and of all solutions to the Schrödinger equation of a system. Let us note that for any perturbation $|\nu\rangle$, the two solutions corresponding to the retarded and advanced solutions of the Schrödinger equation can be written as $|\psi^r\rangle$ and $|\psi^a\rangle$ respectively. In terms of the retarded and advanced Greens function, we can write:

$$\begin{aligned} |\psi^r\rangle \;&=\; -G|\nu\rangle \\ |\psi^a\rangle \;&=\; -G^\dagger|\nu\rangle \end{aligned} \tag{3.61}$$

Taking the difference between these solutions, which is also a solution to the Schrödinger equation:

$$(E - H)(|\psi^r\rangle - |\psi^a\rangle) \;=\; (E - H)(G - G^\dagger)|\nu\rangle \;=\; (I - I)|\nu\rangle \;=\; 0 \tag{3.62}$$

which implies $|\psi\rangle = A|\nu\rangle$ is also a solution to the Schrödinger equation for any vector $|\nu\rangle$. The spectral function is characterized by a peak at all the solutions of the Schrödinger equation. To see this property, we expand the Green's function in terms of the basis set of eigenvectors $|k\rangle$.

$$G = \frac{1}{E + i\eta - H} = \sum_k \frac{|k\rangle\langle k|}{E + i\eta - \varepsilon_k} \tag{3.63}$$

where $\eta$ is a small imaginary part of the energy. $|k\rangle$ are the eigen vectors of $H$ with eigen energies $\varepsilon_k$. Expanding the spectral function over the chosen eigen basis:

$$\begin{aligned} A &= i\left(\frac{1}{E + i\eta - H} - \frac{1}{E - i\eta - H}\right) \\ &= i\sum_k |k\rangle\langle k|\left(\frac{1}{E + i\eta - \varepsilon_k} - \frac{1}{E - i\eta - \varepsilon_k}\right) \\ &= \sum_k |k\rangle\langle k| \frac{2\eta}{(E - \varepsilon_k)^2 + \eta^2} \end{aligned} \tag{3.64}$$

and for a limit $\eta \to 0$ we get:

$$A = 2\pi \sum_k \delta(E - \varepsilon_k)|k\rangle\langle k| \tag{3.65}$$

which is the spectral density of state. Integrating over eigen basis $k$ one obtains the total density of states.

# Chapter 4

# Excited state methods

In this chapter we shall discuss core-excited spectroscopic techniques such as x-ray photo-electron spectroscopy (XPS), near-edge x-ray adsorption fine structure (NEXAFS) and core-hole-clock (CHC) methods. The mechanism, experimental setup and the theoretical treatment of these methods are detailed here. These core-level spectroscopic techniques obtain element-specific information of the electronic structure around adsorption sites and give an insight into the adsorption system geometry, chemical bonding environment and electron transfer dynamics. The core-hole is usually initiated by absorption of a high energy x-ray photon from a synchrotron whose energy is tuned to the ionization energy of interested energy levels. The subsequent decay processes which occur after the excitation and dynamic relaxation also form the basis of various spectroscopic techniques.

## 4.1 X-ray photo-electron spectroscopy

X-ray photo-electron spectroscopy (XPS) is a surface-sensitive quantitative spectroscopic technique which is based on the creation of a core-hole via ionization and provides a method to study the electronic, geometric and chemical properties

of the system. In this technique, photons with sufficient energy are absorbed on a sample causing the ejection of the core-level electrons. If the energy of the absorbing photon is larger than the binding energy of that sample, the excess energy is converted into the kinetic energy of the emitted electron which is analyzed in a detector. Kai Siegbahn and his research group in Uppsala (Sweden) initiated the development of electron spectroscopy for chemical analysis (ESCA)[120] now known as XPS.

### 4.1.1 XPS Mechanism

These photo-electron spectroscopic techniques work on the of photoelectric effect which was explained by Albert Einstein in 1905. Here an incident beam of mono-energetic photons are directed towards the sample. If the energy of the incident photons are greater than the binding energy of the sample, the electrons are excited and emitted from the sample with a kinetic energy based on the laws of energy conservation. The energy conservation of the XPS process can be written as

$$h\nu = E_{BE} + E_{KE} + \phi \tag{4.1}$$

where $E_{BE}$ is the binding energy of the electron, $E_{KE}$ is the kinetic energy of the electron at the detector, $\phi$ is the work function which depends on the sample and the spectrometer. Since the binding energy of the core electron is characteristic for elements in a certain chemical environment, XPS allows for a determination of the atomic compositions of a sample or the chemical state of a certain element as well as electronic structure and band structure. The binding energy is defined as the difference between the energy of the ionized system $E^+$ and that of the ground state $E^0$:

$$E_{BE} = E^+ - E^0 \tag{4.2}$$

The sensitivity of this technique to chemical environments is reflected in the

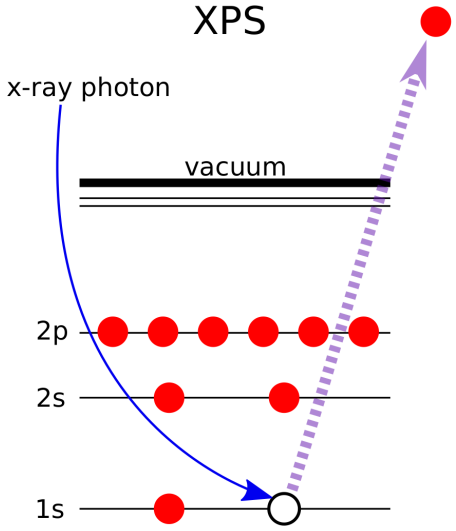


Figure 4.1: The schematic of XPS mechanism shows the creation of a core hole and photo-ionization of a core-level electron.

changes of the binding energy (which is called core level shifts - CLS) which can be used to differentiate the nature of bonding of the same species.

### 4.1.2 Theoretical methods to evaluate CLS

First principle electronic structure calculations using DFT is found to be a useful tool in linking the CLS measured from photo-emission spectroscopic experiments and the local bonding environment of systems of interest. There are two models which are often proposed to predict the CLS within DFT. They are the initial state approximation and ΔSCF approximation. One should note that both these methods are static approximations with a well defined final state and that they neglect the dynamic processes involved in the photo-emission process [121, 122]. In the initial state method, the effect of the core-hole on the valence electrons of

the system is neglected when calculating the final energy of the system. The CLS calculated in this method only reflects the local bonding environment on the core electron before the photo-emission process takes place. Changes in the environment affect the potential the core-electron experiences and this is reflected in the total energy of the system. Mechanisms such the charge transfer dynamics, local charge density and hybridization of the valence states are found to affect the chemical shift due to the change in the electrostatic potential in the core region [123].

In the ΔSCF method, the effects of the valence relaxation after core ionization has taken place and reflecting the screening effects due to the creation of a positive hole in the core shell of the system are considered. The final energy of the system after core excitation $E_f^+$ can be calculated self-consistently assuming that the valence electrons are in the ground state (in the presence of the core hole) and that there are no changes in the system geometry after the introduction of the core hole. The binding energy is then calculated explicitly from 4.2. The core-excited final state calculations are carried out by constructing a core-hole pseudopotential by reducing the occupation of the core state appropriately [124, 125]. In this thesis, we use the ΔSCF method while studying the electronic and magnetic properties of core-excited organic molecules adsorbed on graphene based substrates and look at the electron transfer dynamics associated with these systems.

## 4.2 Near Edge X-ray Adsorption Fine Structure

Synchrotron based spectroscopic techniques contribute significantly in understanding the electronic, physical and chemical properties of materials. One such technique is near edge x-ray adsorption fine structure (NEXAFS) which has been

well studied. NEXAFS can reveal information about the electronic structure and molecular orientation of adsorbed molecules. It probes the absorption of photons by excitation of core-level electrons to the unoccupied bound states or the continuum states. The NEXAFS spectrum shows the dependence of the cross-section of photo-absorption with respect to photon energies and probe the regions from just below the ionization level up to around 50 eV above it [126]. The Figure 4.2 shows a schematic of core-shell excitation of a diatomic molecule (along with its effective potential) with its electronic states and the corresponding NEXAFS spectrum. The step-like spectrum results from the photo-absorption and core-level excitation of an electron to the continuum or the unoccupied final states. A resonant transition occurs when the incoming photon energy matches the energy difference between the initial bound core state and the unoccupied state. Close to the ionization threshold, these transitions are masked by the Rydberg states. The unoccupied molecular orbitals in Figure 4.2 are named $\pi^*$ and $\sigma^*$ which is typical for diatomic molecules. One should also note that the creation of a core-hole shifts these energy levels to lower energies due to the electron–hole Coulomb interaction. The width of these resonant transitions to unoccupied orbitals would depend on the resolution of the detector (leading to a Gaussian broadening), the core-hole XPS linewidth, the charge transfer lifetime of that excited state if the electron transfer of the core-electron is possible (which is a Lorentzian and reflects the orbital symmetry of that orbital with the substrate) and some phononic and vibrational effects of the molecule (which results in some asymmetric broadening). Resonances which lie in the continuum, like the $\sigma^*$ states, have a much larger broadening which is a combination of the lifetime of that state and the vibration of the molecule along the bond direction. The peaks associated to the Rydberg orbitals usually occur between the $\pi^*$ peaks and the ionization potential and are typically sharp and quenched. This is due to the large spatial extension

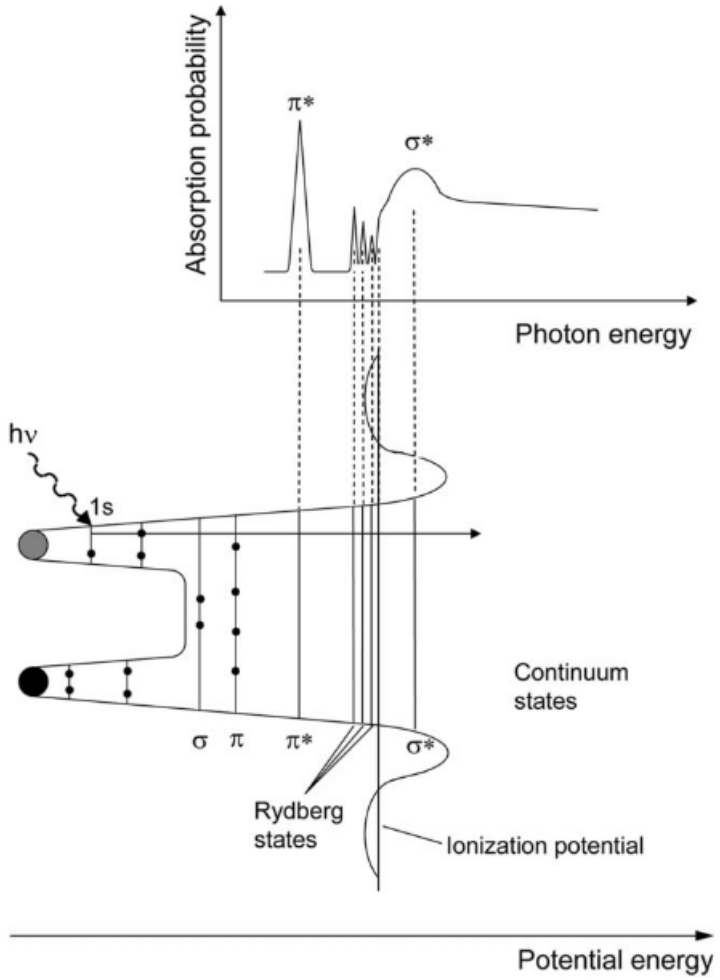


Figure 4.2: The schematic of NEXAFS mechanism (K-shell spectrum) for a diatomic molecule potential. The Rydberg states, continuum states and the unfilled molecular states are also reflected in the adsorption spectrum. The schematic was taken from [126]

of these orbitals. An experimental review of the NEXAFS process and setup is detailed in [126].

Studying the molecular orientation on thin films can also be accomplished by NEXAFS technique. The intensity of the resonances in NEXAFS peaks depend

strongly on the incoming photon field and the transition dipole moment of molecular orbitals [127]. Therefore the molecular orientation on a surface overlayer can be determined by studying the intensity variation of the NEXAFS transitions for different angles of polarization of the probing photon field and the sample surface plane. Hence, this procedure is efficient in determining the tilt angles of adsorbates with respect to the normal [128, 129]. For example, in the case of a planar aromatic hydrocarbons, the information of the orientation of the $\pi$ molecular states fixes only the polar angle with respect to the surface normal in these methods. The effect of the azimuthal angle of the incoming electric field on the NEXAFS of a system, was computationally studied by Fratesi et. al. [130].

The theoretical implementation of NEXAFS is setup within Kohn-Sham DFT where the photo-absorption of a core-level electron from its ground state to a core-excited one is written as the total energy difference between the two states for a $N$ electron system.

$$h\nu \;=\; E_{Tot}(N, n_i = 0, n_f = 1) \;-\; E_{Tot}(N, n_i = 1, n_f = 0) \tag{4.3}$$

The first term of the right is the total energy of the core excited final state $f$ with an initial state ($i$) occupation $n_i$ is zero and the final state occupation $n_f = 1$ representing the excited electron in the previously unoccupied orbital. The second term is the ground state total energy with the initial occupation $n_i = 1$ and an unoccupied final state. The core-level is treated statically due to its localized character. From the transition state approach devised by Slater [131] and using Janak's theorem [132], equation 4.3 can be rewritten in terms of the Kohn-Sham eigen energy values $\varepsilon_i$ and $\varepsilon_f$ at half filling as

$$h\nu \;=\; \varepsilon_f(N, n_i = 1/2, n_f = 1/2) \;-\; \varepsilon_i(N, n_i = 1/2, n_f = 1/2) \tag{4.4}$$

where $\varepsilon_i$ and $\varepsilon_f$ are the KS Eigen values of the initial and final levels respec-

tively. A disadvantage of this method is that it requires an electronic structure calculation for every final state in order to include the continuum states. This was overcome by Triguero et. al. [133] when he proposed the Transition-Potential (TP) approach. The state-by-state calculations of the transition-state approach is circumvented by neglecting the partial occupation in the final state $f$ and is called half core hole (HCH) approximation [134, 135].

$$h\nu \;=\; \varepsilon_f(N, n_i = 1/2, n_f = 0) \;-\; \varepsilon_i(N, n_i = 1/2, n_f = 0) \tag{4.5}$$

The spectrum is computed by diagonalizing the matrix elements of the Hamiltonian constructed using the HCH potential. The transition amplitudes are calculated taking into account the Fermi's golden rule and is given by the dipole operator oriented along the direction of photon-field polarization and evaluated between the initial and final KS states. Although in this thesis we do not go into detail in NEXAFS calculations, this serves an a useful tool in analyzing and interpreting molecular geometries of experimental results.

## 4.3 Core-Hole-Clock Spectroscopy

Most of the organic electronic device architectures involve interfaces formed between an organic overlayer and an electrode. The charge transfer dynamics at these interfaces play a vital role in determining the performance of these devices [136]. Understanding and quantifying the relevant timescale of the charge transfer processes would play a vital role in engineering such devices. Most of the time resolved spectroscopic techniques such as the pump-probe methods, where an initial laser pulse instigates the system dynamics (pump) and a second pulse (probe) studies the evolution of the dynamics after a small time delay. The bottle-neck of this method lies in the width of the initial laser pump and the time delay between

the two pulses [137]. The core-hole-clock (CHC) technique differs from the conventional pump-probe methods in two key aspects:

1. The lifetimes of an excited state are worked out based on the intensities of core-excitation and decay with reference to the intrinsic core-hole lifetime. The measurement here is carried out in the energy domain instead of the time domain and is often referred as excitation-decay.

2. Since the core-electrons are involved in this method, atomic distinction is possible which is unique to such core-spectroscopic techniques.

3. The resulting core-hole acts as a perturbation and the system molecular orbital symmetries must be taken into account.

Some detailed reviews of this technique with reference to organic/inorganic interfaces can be found in refs [138, 139, 140, 141]. Figure 4.3 shows the different photo-excitation and various possible decay channels involved in the CHC technique. Figure 4.3 (a) is a direct excitation model where an electron from the valence of the system is photo-excited to vacuum. Figure 4.3 (b) Shows a core-level excitation which is photo-emission of a core level electron to vacuum where it is detected by an analyzer. Figure 4.3 (c) is the resonant photo-excitation where a core electron is is excited to an unoccupied molecular orbital (eg. LUMO shown in the figure). Following the excitation processes, the decay channels available for de-excitation are auto-ionization processes (Figure 4.3 (d) and (e)) and charge transfer process Figure 4.3 (f). When the core-excited overlayer is moderately isolated from the substrate and if the photo-excited electron does not transfer to the substrate before the core-hole lifetime, the decay channels usually available are the auto-ionization ones, namely spectator decay and participator decay. During the spectator decay (Figure 4.3 (d)), the photo-excited electron remains in one of the unoccupied states and does not participate in the de-excitation process directly. It indirectly influences the other electrons decay with some Auger-like processes

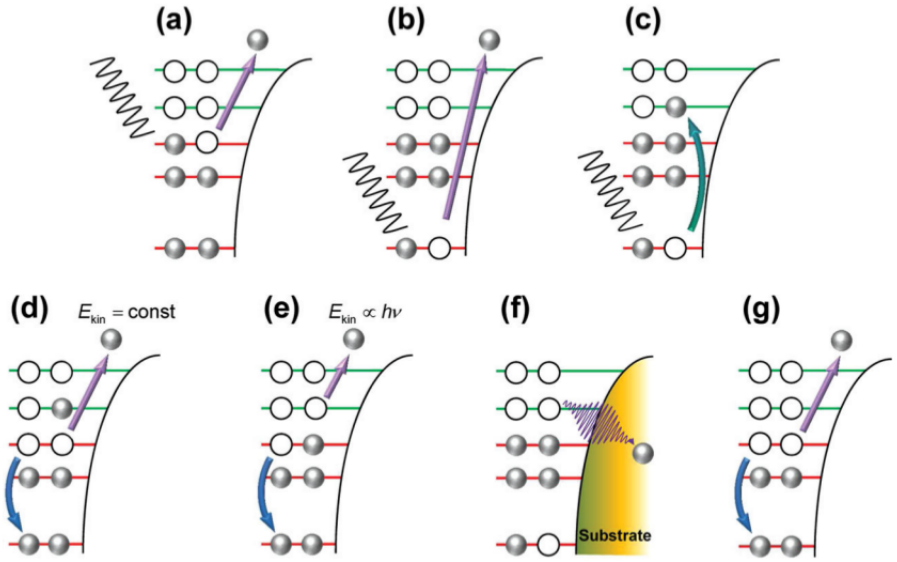


Figure 4.3: The schematic of photo-excitation and de-excitation processes which follows a core-level excitation. (a) Direct photo-excitation where emission of an electron is initiated by excitation of a valence state (b) core-level excitation (c) Resonant excitation where a core electron is excited to LUMO (d) Spectator decay (resonant Auger) (e) Participator decay (resonant photo-emission) (f) Charge transfer of the core-excited electron into the substrate states (g) Normal Auger decay which would follow (f) or (b). the figure is taken from [136].

which increases the kinetic energy of the emitted Auger electron by providing an electrostatic screening. This leads to the emergence of new resonant Auger-like features with lower binding energy and constant kinetic energy beside the normal Auger feature. Another case one could expect is the participator decay (Figure 4.3 (e)) where the photo-excited electron, which initially had filled an unoccupied state, participates in the decay process and fills the core hole. Further, the emission of an occupied electron with an excess kinetic energy (the difference between the final occupied state of the participator and the core hole) and leaves the system with a hole in one of the previously occupied states. The final state of

a participator decay is similar to the configuration the system attains after direct photo-emission seen in Figure 4.3 (a). But since this decay process is assisted by the resonant photo-emission of the core hole, there is a larger cross-section for the valence electron which leads to an enhancement of the peaks associated with the occupied (and now photo-emitted) electronic state in the emission spectrum. Unlike the spectator case where the binding energy is shifted, in the participator decay, the binding energy of the resonant photo-emission peak remains constant across the absorption threshold. The third and equally interesting decay channel is when the molecular over is strongly coupled with the substrate states. The probability of the electron transfer to the substrate states within the core-hole lifetime is very high (Figure 4.3 (f)). When this occurs, the participator and the spectator decay channels are significantly quenched and the core-hole decays via normal Auger process (Figure 4.3 (g)).

### 4.3.1 Calculating the charge transfer lifetime

After setting up the the excitation processes and the decay channels, we now discuss the method to extract the charge transfer lifetimes. The character of the decays can be described by the exponential decay laws where the decay rate $dN/dt$ is proportional to the number of systems available in the excited final state.

$$\frac{dN}{dt} \;=\; -\frac{\Gamma}{\hbar}N(t) \tag{4.6}$$

where $\frac{\Gamma}{\hbar} \equiv \tau$ is the decay time. $\Gamma$ is interpreted as the imaginary part of the self-energy [142] and is proportional to the decay rate and inversely proportional to the decay time ($\tau$). This quantity is also a reflection of the coupling of the core-excited state with the substrate and is proportional to the total intensity of the measured spectrum. The solution of equation 4.6 is given by

$$N(t) \;=\; N_0 e^{-t/\tau} \;=\; N_0 \exp\Big(-\frac{\Gamma}{\hbar}t\Big) \tag{4.7}$$

Where $N_0$ is the initial number if excited (unstable) systems prepared at an arbitrary time zero and $N(t)$ is the number of systems left in the excited state after a time $t$. The probability of the non-decayed states after excitation within the time interval $T$ is given by

$$P(T) \;=\; 1 - \int_0^T \frac{\Gamma}{\hbar} \exp\Big(-\frac{\Gamma}{\hbar} t\Big) dt. \tag{4.8}$$

The charge transfer lifetime can be setup as $\tau_{CT} \equiv \frac{\hbar}{\Gamma_{CT}}$ and the core-hole lifetime $\tau_C \equiv \frac{\hbar}{\Gamma_C}$ [143]. From the definitions setup in equation 4.8 one can write the probability for no occurrence of the charge transfer within time $T$ as

$$P_{NoCT}(T) \;=\; 1 - \int_0^T \frac{\Gamma_{CT}}{\hbar} \exp\Big(-\frac{\Gamma_{CT}}{\hbar} t\Big) dt. \tag{4.9}$$

and similarly the probability of the occurrence of the core-hole is

$$P_C(T) \;=\; \int_0^T \frac{\Gamma_C}{\hbar} \exp\Big(-\frac{\Gamma_C}{\hbar} t\Big) dt. \tag{4.10}$$

Equation 4.9 refers to a situation where no charge transfer happens and equation 4.10 reflects a case where core-hole decay occurs. It remains general in terms of explaining which decay channels are activated. Considering the conditional probability of a sequence where the core excited system decays at a time $T$ with no charge transfer occurring within this time interval:

$$P_C^{NoCT}(T) \;=\; \int_0^T \frac{\Gamma_C}{\hbar} \exp\Big(-\frac{\Gamma_C}{\hbar} t_1\Big) \;\times\; \left[1 - \int_0^{t_1} \frac{\Gamma_{CT}}{\hbar} \exp\Big(-\frac{\Gamma_{CT}}{\hbar} t_2\Big) dt_2\right] dt_1 \tag{4.11}$$

And as $T \to \infty$, for a system where the excited system has certainly undergone decay, equation 4.11 simplifies to

$$P_C^{NoCT} \;=\; \frac{\Gamma_C}{\Gamma_C + \Gamma_{CT}} \tag{4.12}$$

The fraction of intensities from Equation 4.12 tells us the fraction of spectral intensities which are sue to decay processes other than charge transfer which occurs

before the decay of the core-hole. Therefore the remaining fraction in the spectrum would be the probability of charge transfer within the core home decay and is given by

$$P_C^{CT} = \frac{\Gamma_{CT}}{\Gamma_C + \Gamma_{CT}}. \tag{4.13}$$

Equation 4.13 can be rewritten in terms of the decay times as

$$P_C^{CT} = \frac{\tau_C}{\tau_C + \tau_{CT}}. \tag{4.14}$$

Since $\Gamma_C$ is proportional to the Auger transition which takes into account both the resonant and non-resonant decay channels, the magnitude of relevant to $\Gamma_{CT}$ emerges from the intensity ratios. Also, since this is a general presumption and we do not define the exact final excited state, all cases of dynamic resonant charge transfer are included within the considered approximation. The equations 4.13 - 4.14 in terms of the intensity rations can be written as

$$P_C^{CT} = \frac{I_{Aug}}{I_{Aug} + I_{res}}. \tag{4.15}$$

Here $I_{Aug}$ is the intensity of the normal Auger process and $I_{res}$ is the resonant transfer intensity of the autoionization components. The charge transfer lifetime can then be written as

$$\tau_{CT} = \tau_C \frac{1 - P_C^{CT}}{P_C^{CT}} \tag{4.16}$$

In practical cases when the normal Auger and the autoionization peaks overlap strongly, the resolution of these components become challenging. In such a case, the participator decay channel of an isolated system (such as multilayer molecules) ($I^{iso}$) shows an intensity proportional to the total spectral intensity and for a coupled system ($I^{coup}$) this participator channel intensity decreases. The difference between these intensities $I^{iso} - I^{coup}$ correspond to the charge transfer process. This relationship in terms of the charge transfer lifetimes can be written from eq. 4.15 and eq. 4.16 as

$$\tau_{CT} = \tau_C \frac{I^{coup}}{I^{iso} - I^{coup}} \tag{4.17}$$

**Computational methodology to calculate charge transfer lifetime**

The computational methodology to extract the charge transfer lifetime can be mainly classified into three steps as shown in Figure 4.4. Initially, the geometry of the system is relaxed to reach the most stable configuration. The calculation of the interfacial ground state energies confirms the stability of the system and its electronic properties can checked by appropriate visualization of the system DOS and projections onto the molecular orbitals. We then use this stable system configuration to perform a core-hole calculation making an assumption that the presence of the added core hole alters only the electronic aspects of the system but not the geometric ones. The influence of the core hole is introduced by using a full core hole pseudopotential in the appropriate molecular orbital. Details of the pseudopotential method is described in the previous chapter when dealing with the theoretical aspects of DFT. We now electronically relax the system in the presence of the core hole to understand its effect on the energy level alignment of the system. Cases particular to our research work have been dealt in depth in the following chapters. The charge transfer lifetime is the time taken for an electron which is resonantly excited to a molecular orbital to be transfered to the substrate. This primarily depends on the coupling of the molecular states with that of the substrate. The core hole generated acts mainly as in environment which influences this orbital alignment. The molecular coupling with the substrate states is seen in the broadening of the molecular states upon adsorption and further reflected in the orbital alignment upon core level excitation. A strong molecular coupling with the substrate leads to a large broadening in the molecular energy levels which in turn decreases the charge transfer lifetime. The relation of the lifetime with the full width at half maximum can be calculated from the expression shown in Figure 4.4 [144]. Therefore with relevant assumptions such as excluding phononic perturbations, many-body dynamic interactions and considering a final static state of

the decay process, we are able to effectively estimate the charge transfer lifetime which is comparable with core-hole-clock experiments.

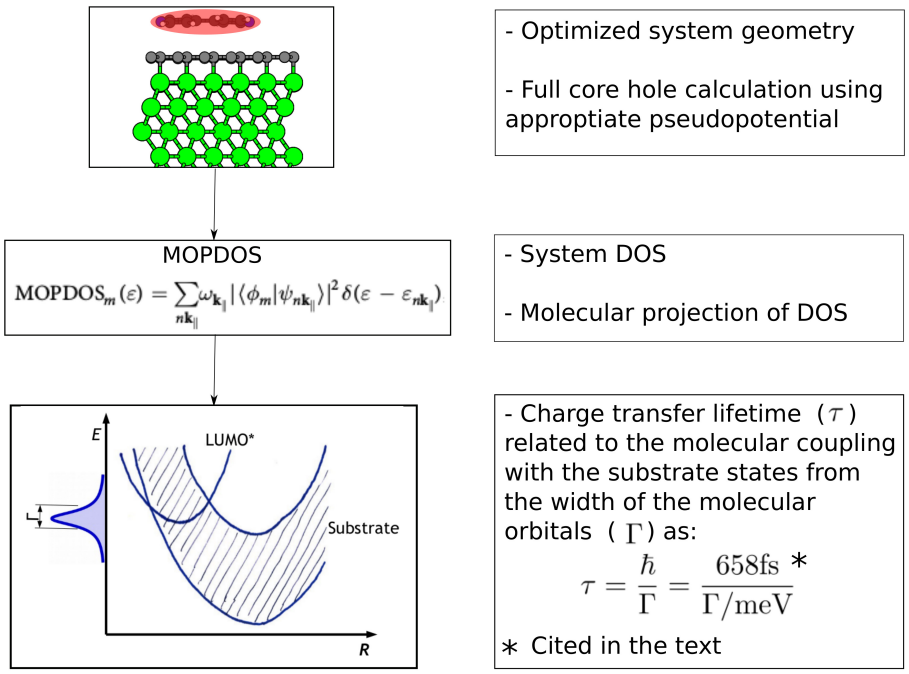


Figure 4.4: The schematic to show the methodology used to computationally extract the charge transfer lifetime.

## 4.4 Ultrafast bidirectional charge transfer

A possible charge transfer channel that may occur in certain cases is when, upon molecular core excitation, a previously unoccupied molecular orbital shifts partially below the Fermi level. In such a scenario, one observes a bidirectional charge transfer process occurring where an electron is transfered initially from the substrate to the molecule which later de-excites (given that this occurs within the core-hole lifetime). This was initially observed experimentally in [145] and was studied extensively [146, 147]. In this section, we plan to elaborate on this

concept and discuss the nomenclature of superparticipator peaks and extraction of charge transfer lifetime in such cases.

This is relevant because in our studies of bipyridine/graphene/metal interfaces which is discussed in chapter 6, we find a similar phenomena occurring and it is of interest to provide a summary of this mechanism here. Previously we have studied various decay channels such as the auto-ionization processes and the charge transfer process. When we have a molecule/substrate interface and core-excite an electron on the molecule, the creation of a core hole results in the shift of the molecular energy levels to lower values (close to the substrate Fermi level) in order to screen the positive core hole. If the excited electron is in the molecular LUMO (LUMO*) and the LUMO* remains above the Fermi level of the substrate, the electron which occupies the LUMO* can decay into the substrate within the core-hole lifetime as long as LUMO is coupled to the substrate states [148].

However a case may arise (example: bipyridine/Au(111)[146], pyridine/Au(111) [147], bipyridine/graphene/Ni(111), bipyridine/bilayer graphene/Ni(111) (our studies), etc) where, upon core-excitation of an electron to an unoccupied molecular state (or continuum state), a significant portion of LUMO* drops below the Fermi level. In such a case, the molecular LUMO* gets filled by an electron from the substrate even if the core electron is still present in one of the higher lying unoccupied molecular orbitals (like LUMO+1, 2.. etc). This leads to a characteristic spectral line which arises due to the decay of LUMO* which is independent of the incident photon energy. This process is denoted a superparticipator decay. The bidirectional nature of this process is due to the initial charge migration from the substrate to the molecular LUMO* and the subsequent decay of the excited electron, provided these processes occur within the core-hole lifetime. This also

leads to loss of the phase information on the core-excited LUMO* electron due to its interaction with the substrate and therefore the decay of the LUMO* electron is not similar to the direct photo-emission pathway.

The bidirectional charge transfer mechanism can be worked out from a similar logic used in the previous section. The two possible scenarios that can be presented are resonant core-excitation to LUMO or excitation to a free electron continuum state. The highlight of this transfer mechanism is that, upon core-excitation, the molecular LUMO shifts partially below the Fermi level. Let us first consider the case where the the core-electron is excited to LUMO. A fraction of LUMO which now shifts below the Fermi level is denoted as $x$. The probability of such a system to decay before the charge transfer process occurs $P_{NoCT}$ can we written as

$$P_{NoCT} = x + \int_0^\infty \frac{\Gamma_C}{\hbar} e^{-\Gamma_C t/\hbar}(1-x)\left[1 - \int_0^t \frac{\Gamma_{CT}}{\hbar} e^{-\Gamma_{CT} t'/\hbar} dt'\right] dt, \qquad (4.18)$$

which further simplifies to

$$P_{NoCT} = x + (1-x)\frac{\Gamma_C}{\Gamma_{CT}+\Gamma_C}, \qquad (4.19)$$

where $\Gamma_{CT}$ and $\Gamma_C$, as defined in the previous section, are inversely related to the charge transfer and core hole decay times respectively as $\tau_{CT} = \hbar/\Gamma_{CT}$ and $\tau_C = \hbar/\Gamma_C$. The probability that charge transfer does not occur increases as a larger part of LUMO shifts below the Fermi level and this is reflected in the value of $x$. Therefore only the term $1-x$ is seen to reflect the charge transfer probability in equation 4.18. Therefore one can write the probability of charge transfer occurring within the core hole lifetime as

$$P_{CT} = \int_0^\infty \frac{\Gamma_C}{\hbar} e^{-\Gamma_C t/\hbar}\left[(1-x)\int_0^t \frac{\Gamma_{CT}}{\hbar} e^{-\Gamma_{CT} t'/\hbar} dt'\right] dt, \qquad (4.20)$$

and can be written as

$$P_{CT} = (1-x)\frac{\Gamma_{CT}}{\Gamma_{CT}+\Gamma_C}. \tag{4.21}$$

We see here that when the LUMO is completely above the Fermi level ($x$=0), equations 4.19 and eq 4.21 revert back to conventional CHC expressions of eq. 4.12 and eq. 4.13. When $x$=1, the LUMO is fully below the Fermi level and no charge transfer can occur and the participator intensity in this case is similar to that of an isolated system. These probabilities can be related to the RPES intensities from a coupled system ($I_p$, $I_{Auger}$ and $I_{Raman}$ are the participator, normal Auger and spectator shifted Auger/Raman Auger intensities respectively) as

$$\frac{P_{NoCT}}{P_{CT}} = \frac{I_p + I_{Raman}}{I_{Auger}} \propto \frac{\Gamma_C + x.\Gamma_{CT}}{(1-x)\Gamma_{CT}}. \tag{4.22}$$

The charge transfer time $\tau_{CT}$ can then be written as

$$\tau_{CT} = \tau_C \left[\frac{I_p}{I_{Auger}}.(1-x) - x\right]. \tag{4.23}$$

The charge transfer time in terms of coupled and isolated systems can be written as

$$\tau_{CT} = \tau_C \left(\frac{I^{coup}}{I^{iso}-I^{coup}} - \frac{xI^{iso}}{I^{iso}-I^{coup}}\right), \tag{4.24}$$

where $x$=0, eq. 4.24 is same as the conventional CHC as in eq. 4.17.

The alternate case would be when the core electron is excited to the continuum. In such a case, when the previously unoccupied LUMO partially shifts below the Fermi level by $x$, there is a probability that it can get populated from the substrate within the core hole decay time. This opens up a superparticipator channel along with the normal Auger and the electron transfer dynamics is reflected in the relative intensities of these two pathways. The probability of the back transfer from the substrate to occur can be written as

$$P_{BT} = \int_0^\infty \frac{\Gamma_C}{\hbar} e^{-\Gamma_C t/\hbar}\left[x\int_0^t \frac{\Gamma_{BT}}{\hbar} e^{-\Gamma_{BT}t'/\hbar}dt'\right]dt, \tag{4.25}$$

and this can be simplified as

$$P_{BT} = x\frac{\Gamma_{BT}}{\Gamma_{BT}+\Gamma_C}. \tag{4.26}$$

The probability of no backtransfer occurring from the substrate is written as

$$P_{NoBT} = (1-x) + x\int_0^\infty \frac{\Gamma_C}{\hbar}e^{-\Gamma_C t/\hbar}\left[1-\int_0^t \frac{\Gamma_{BT}}{\hbar}e^{-\Gamma_{BT}t'/\hbar}dt'\right]dt, \tag{4.27}$$

and can be written as

$$P_{NoBT} = (1-x) + x.\frac{\Gamma_C}{\Gamma_{BT}+\Gamma_C}. \tag{4.28}$$

The probability ratio can be written from eq. 4.26 and eq. 4.27 as

$$\frac{P_{NoBT}}{P_{BT}} = \frac{\Gamma_C+(1-x)\Gamma_{BT}}{x\Gamma_{BT}} = \frac{\tilde{\tau}_{BT}}{x} + \frac{1-x}{x}. \tag{4.29}$$

$\tilde{\tau}_{BT} = \frac{\tau_{BT}}{\tau_C}$ is a dimensionless quantity. In eq. 4.29, there are two unknown quantities $x$ and $\tau_{BT}$. In terms of the RPES intensities, the probability ratio can be written as

$$\frac{P_{NoBT}}{P_{BT}} = \frac{I_p^{iso}-I_{sp}^{coup}}{I_{sp}^{coup}}, \tag{4.30}$$

which can be translated to

$$\tilde{\tau}_{BT} = \frac{x-I_{sp}^{coup}/I_p^{iso}}{I_{sp}^{coup}/I_p^{iso}}. \tag{4.31}$$

By defining relevant fractions $f = I_p^{coup}/I_p^{iso}$ and $\beta = I_{sp}^{coup}/I_p^{coup}$, the direct charge transfer time can be obtained as

$$\tilde{\tau}_{CT} = \frac{f-x}{1-f}, \tag{4.32}$$

and the backtransfer time is

$$\tilde{\tau}_{BT} = \frac{x-\beta f}{\beta f}, \tag{4.33}$$

A detailed review of these processes are discussed in [138] and the equations for bidirectional transfer process has been worked out in detail in the supplementary material of [147].

# Chapter 5

# Organic molecules on graphene

In this chapter we discuss the effect of adsorption of organic molecules on graphene and understand how the adsorption character of these molecules with graphene influence the magnetism in the system upon molecular core-level excitation. The three molecules studied here are pyridine, picoline radical and pyridine radical, each having a unique adsorption behavior upon interaction with graphene. We find the induction/suppression of magnetism in these systems when the N-1s core level of the molecule is photo-excited [149].

## 5.1 Introduction

Graphene, as introduced in detail in Chapter 1, is a two dimensional crystalline allotrope of carbon with honeycomb lattice structure and has been extensively studied since its discovery in 2004 [1, 28, 51, 5]. It displays a unique electronic band structure where the valence and conduction bands intersect at $K$ points of the first Brillouin zone forming the Dirac cones [150]. Several interesting properties such as ballistic transport [151], long mean free path at room temperature [152], high charge carrier mobility with massless relativistic carriers called Dirac Fermions

[17] and anomalous integral and half integral quantum Hall effect [153, 154, 155] are displayed by graphene due to its linear dispersion of bands at the Fermi level and the absence of bandgap (making graphene a semi-metal). Due to these properties, graphene and its composites are seen as ideal candidates for efficient gas sensors [156, 16], novel spintronic devices [157] and transparent electrodes for photo-voltaics [158, 159]. Free standing graphene, due to its bipartite lattice structure does not display any intrinsic magnetism and this limits its applications in magneto-electronics and active spintronics. In chapter 1, while discussing the magnetic properties of graphene, we also explain several recent methods studied to induce magnetism in graphene. One of the methods to induce magnetism in graphene is by covalent adsorption of molecules, which we shall discuss in this chapter.

We also study relevant time dependent effects on the magnetism of graphene-related systems in this chapter. Recent studies in ultrafast magnetization, also called femtomagnetism, is an important topic of current interest. This was first investigated by Beaurepaire et al., who showed that a rapid demagnetization is induced in Ni by using femtosecond optical pulses [160]. In ferromagnetic thin films by using near-infrared femtosecond laser pulses, it is possible to disentangle the spin and orbital components of the magnetic moment and to probe this by femtosecond resolved X-ray magnetic circular dichroism (XMCD) [161]. Another recent advancement in XMCD allows the direct measurement of transient magnetic moments in copper caused by the injection of spin polarized current from an adjacent ferromagnetic cobalt. It was found that the transients of these spin resolved currents for graphene coupled with magnetic cobalt occurred within a few femtoseconds [162]. Core-level excitations in electron energy loss spectroscopy (EELS) can also be employed to study the magnetic moment in graphene induced

by adsorption of transition metal dopants at defect sites [163].

The core hole clock spectroscopy [164] is a technique which allows one to determine charge transfer times from adsorbed molecules on graphene interfaces [146] which are applicable in several fields like photovoltaics and light emitting diodes[165, 166, 167, 168, 169]. There is a necessity to provide proper description of the dynamic properties of the system under study to fully understand and exploit the experiments, but one should note that core-hole-clock method is also capable of performing spin-resolved measurements by either creating resonances by circularly polarized light or using spin-resolved detection of the emitted electrons [170, 171].

The motivation for this part of the work was to understand the effect of core level excitations of adsorbed molecules on graphene, aiming at the limit where only one molecule in a diluted array of adsorbed species is core-excited. We take into account three molecules namely pyridine ($C_5H_5N$), 4-picoline radical ($C_6H_6N$) and pyridine radical ($C_5H_4N$), which are prototypes of different couplings with graphene. Interaction of pyridine with graphene is dominated by van der Waals forces, that of pyridine radical is mainly via chemisorption, while 4-Picoline radical is affected by both van der Waals forces and covalent bonding and represents an intermediate case between pyridine and pyridine radical. We evaluate the electronic properties for the molecules where the N atom is ionized and compare them to the ground state ones. We investigate how the electrons of the system relax around the core hole, inducing or suppressing magnetism in the valence shell depending on the type of adsorption.

In the following section we outline the computational methodology. Then, the

results of our models will be presented and discussed in detail followed finally by the conclusions.

## 5.2 Simulation Details

We perform first principles calculations based on density functional theory (DFT) [92, 86, 88] within the generalized gradient approximation (GGA) framework using Perdew-Burke-Ernzerholf (PBE) exchange correlation functional [172, 173] and a plane wave basis set as implemented in the Quantum Espresso platform [174]. The van der Waals interactions play an important role in the adsorption mechanism of these organic molecules and Grimme correction [99] is included to explain this accurately. The chosen $5\times7$ surface periodicity of the graphene substrate ensures low adsorbate concentration of $6.69 \times 10^{-3}$Å$^{-2}$ and negligible inter-molecular interactions. A vacuum region of 15 Å is set to minimize the interaction between graphene layers along the z-axis orthogonal to graphene. The plane wave kinetic energy cut-off is 42 Ry and the convergence on the energy and force are $10^{-4}$ a.u. and $10^{-3}$ a.u. respectively. The Brillouin zone is sampled using a $3\times2\times1$ $\Gamma$-centered k-point grid for system relaxation and total energy calculations. A $18\times12\times1$ $\Gamma$-centered k-point grid is chosen to calculate the density of states. The simulation settings are tested for free standing graphene and its lattice constant was found to be 2.462 Å, which is in very good agreement with the experimental value of 2.46 Å[175].

For the excited state calculations, we use a pseudo-potential with a full core hole (FCH) created at the N 1s orbital of the molecule. We always consider a globally neutral system, where an additional electron is given to the system valence shell[144, 176]. Physically, this corresponds to the X-ray absorption at the edge

or to the static final state of a photo-emission experiment assuming that the valence shell relaxes fully around the core hole. In the latter case, a further electron is attracted to the molecular region from the surrounding graphene. This cannot occur in the calculation since the neighboring cells are also excited due to periodic boundary conditions. Hence the necessity to add an electron to the valence shell to make the most representative model of the physical case, where very few molecules are excited simultaneously. This also provides a more effective convergence with respect to unit cell size as thoroughly demonstrated recently[176].

## 5.3 Pyridine on graphene

Pyridine is a class of heterocyclic organic molecule which belongs to the benzene family with a chemical formula $C_5H_5N$. One of the methyl groups of benzene is replaced by a nitrogen atom to form pyridine. The relaxed gas phase structure of pyridine is shown in figure 5.1. We have numbered the nitrogen atom, the inequivalent carbons and the hydrogen atoms attached to them. The bond angles and the bond lengths are also summarized in the figure. Pyridine is a conjugated planar molecular system with 6 electrons forming a delocalized $\pi$ ring. The electronic density is not evenly distributed due to the negative inductive effect of the nitrogen atom, which is also reflected in the smaller bond length of N-C atoms. All the atoms in pyridine are $sp^2$ hybridized with a lone pair of electrons on the nitrogen atom projecting out of the ring in plane with the $\sigma$ bonds of the ring. The gas phase molecular orbitals of pyridine from HOMO-2 to LUMO+1 are summarized in figure 5.2. HOMO mainly comprises of $\sigma$ molecular orbitals which are in plane with the molecule. LUMO is mainly built from $\pi$ orbitals and out of the molecular plane. The ground state density of states for the gas phase system is shown

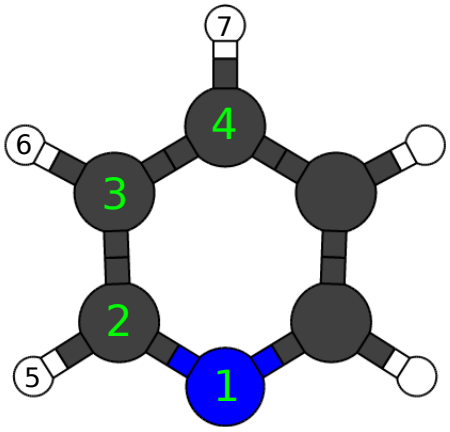


Figure 5.1: The relaxed atomic structure of gas phase pyridine molecule. The relevant bond lengths and bond angles are tabulated.

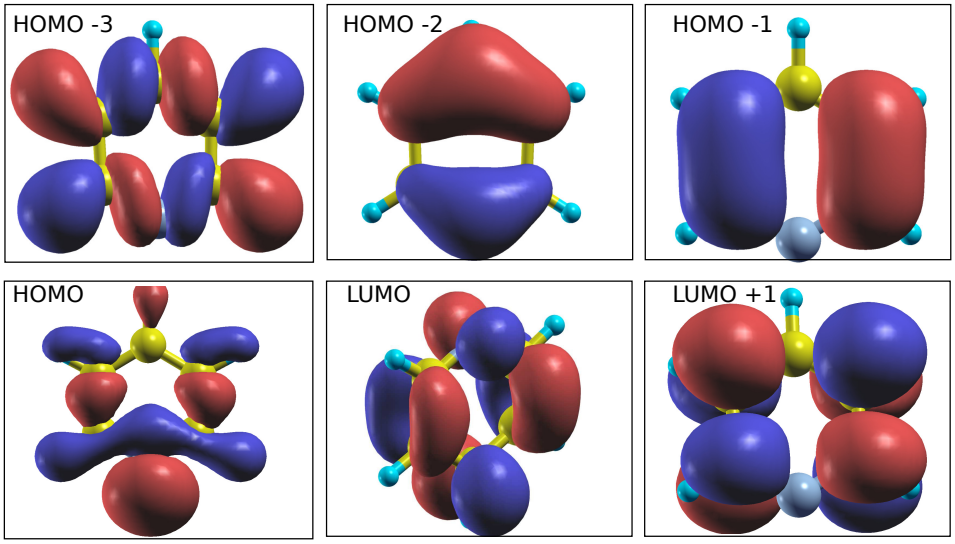


Figure 5.2: The gas phase molecular orbitals of pyridine from HOMO-2 to LUMO+1 are shown.

in figure 5.3. A fictitious gaussian broadening is used with a full width at half maximum (FWHM) of 0.1132 eV. We now look at pyridine on graphene system.

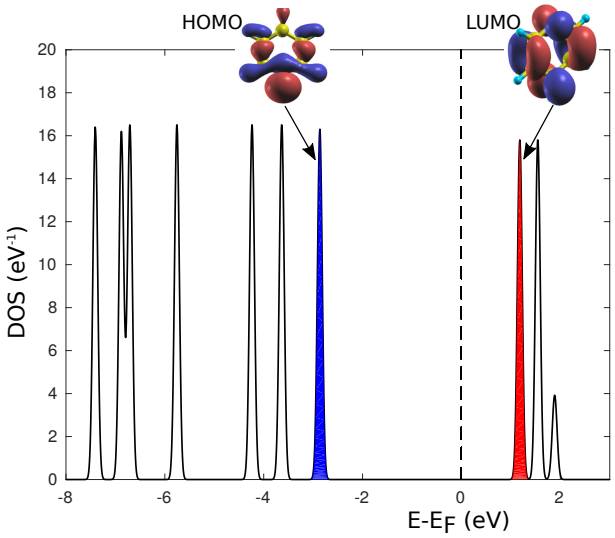


Figure 5.3: The ground state density of states of gas phase pyridine. The insets show the molecular orbitals at HOMO and LUMO of pyridine.

Pyridine interacts weakly via van der Waal's forces when adsorbed on graphene. We start by finding the most stable adsorption configuration of this system. Figure 5.4 shows the possible adsorption configurations considered taking into account the translational and rotational degrees of freedom. The configurations are named based on the orientation of pyridine on graphene. If the pyridine ring is parallel to graphene, the prefix "Par" is used and "Per" when the molecule is perpendicular to the graphene plane. Depending on whether the N atom of pyridine is above one of the two inequivalent carbon atoms of graphene or at the center of the graphene ring the suffix "TopA/B" and "Cent" is used. We begin by relaxing the system to calculate the adsorption energies and the adsorption bond lengths which give us an insight on the relative stability of these systems during the adsorption process. The adsorption energy is defined as $E_{ads} = E_{g+m} - E_g - E_m$. Here $E_{g+m}$ is the total energy of the optimized molecule-graphene system, $E_g$ and $E_m$ are the total

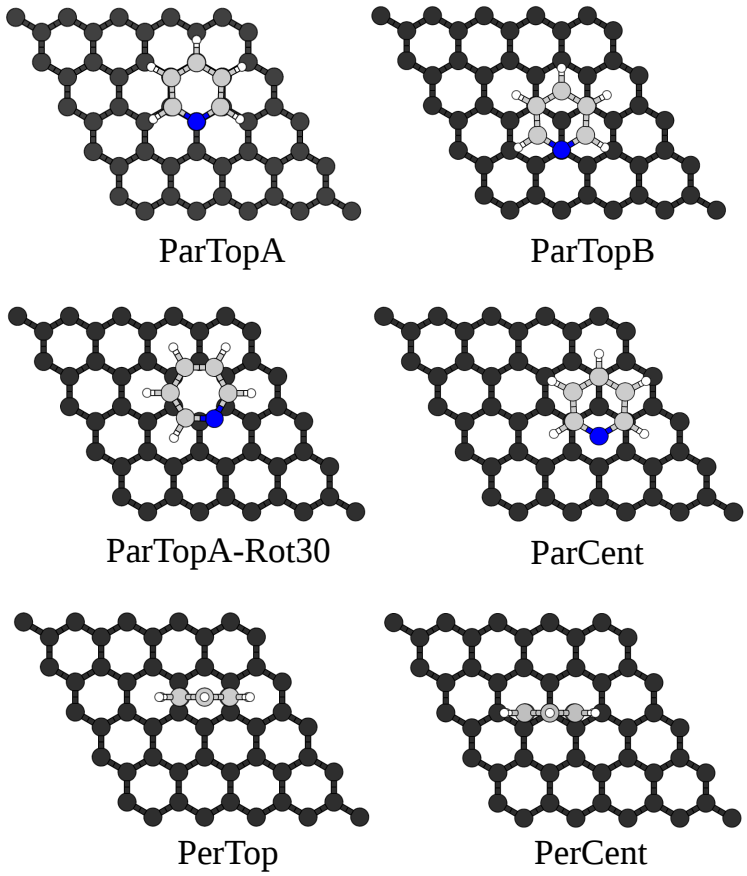


Figure 5.4: The various adsorption configurations of pyridine on graphene.

energies of the isolated graphene substrate and of the gas phase molecule/radical, respectively. The adsorption energies ($E_{ads}$) and the graphene-molecule bond distances ($a_{gm}$) are summarized in Table 5.1. We see from Table 5.1 that pyridine placed parallel to graphene, with its N atom at the center of a graphene ring, is the most stable configuration at low molecular concentration (ParCent configuration from Figure 5.4 ) and its interaction with the substrate is dominated by van der Waals forces. These results are supported by various experimental and theoretical studies of closed shell organic molecules adsorbed on graphene [177, 178, 179]. Our most stable configuration displays the pyridine ring symmetrically located with its nitrogen atom at the center of the graphene ring and oriented similar to

| Configuration | $E_{ads}$ (meV) | $a_{gm}$ (Å) |
|---|---|---|
| ParTopA | -544 | 3.34 |
| ParTopB | -593 | 3.20 |
| ParTopA-rot30 | -537 | 3.49 |
| ParCent | -599 | 3.20 |
| PerTop | -411 | 3.07 |
| PerCent | -428 | 2.89 |

Table 5.1: The adsorption energies ($E_{ads}$) and graphene-molecule bond lengths ($a_{gm}$) are tabulated for the various configurations of pyridine on graphene.

AB stacking found in graphite. Another arrangement on graphene in which the nitrogen atom is above one of the carbon atoms of graphene has similar adsorption energy (ParTopB from Figure 5.4), just 6 meV less stable. A small energy difference between these configurations [179] points to high molecular diffusivity. If we neglect the van der Waals interactions, the adsorption strength is underestimated by one order of magnitude while the adsorption bond length is seriously overestimated. We proceed to further analyse the relevant properties of this stable configuration - ParCent.

To understand the electronic and magnetic properties of the system, we plot the total density of states (DOS) and that projected onto the molecular orbitals (MOPDOS). The latter is evaluated as [144],

$$\mathrm{MOPDOS}_m(\varepsilon) = \sum_{n\mathbf{k}_{||}} \omega_{\mathbf{k}_{||}} |\langle \phi_m | \psi_{n\mathbf{k}_{||}} \rangle|^2 \delta(\varepsilon - \varepsilon_{n\mathbf{k}_{||}}), \tag{5.1}$$

where $\varepsilon_{n\mathbf{k}_{||}}$ and $\psi_{n\mathbf{k}_{||}}$ are the Kohn-Sham eigenvalues and eigenvectors, respectively, and $\mathbf{k}_{||}$ samples the surface Brillouin zone with weights $\omega_{\mathbf{k}_{||}}$, and we represent the Dirac $\delta$ function by a Gaussian function. The molecular states $|\phi_m\rangle$

have been evaluated for isolated species taking spin-compensated solutions for the ground state or core-excited one, depending on the case of interest. The dangling bonds of the radicals were saturated with H atoms. The overlaps between wave functions, $\langle \phi_m | \psi_{n\mathbf{k}_{||}} \rangle$, are eventually computed via an atomic basis representation. Further information regarding the implementation of MOPDOS is explained in the appendix B.

For pyridine on graphene configuration, the ground state DOS and its projec-

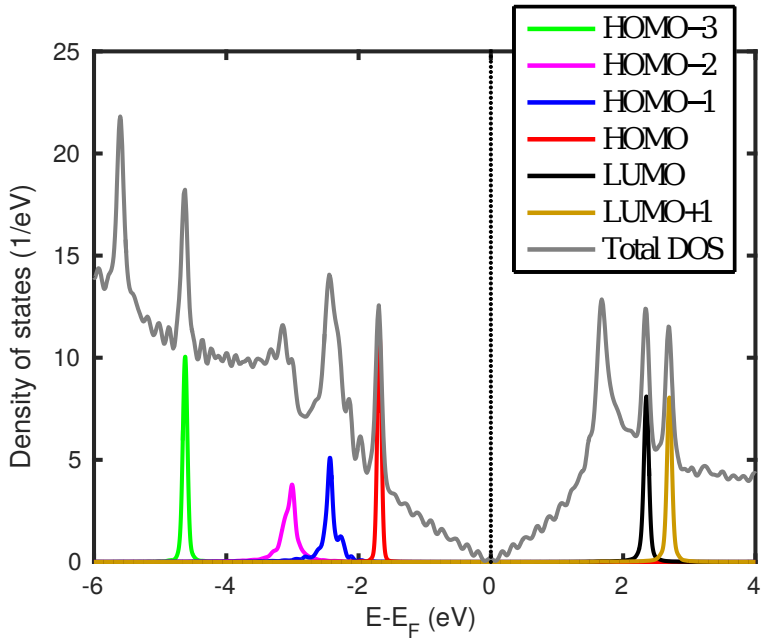


Figure 5.5: Ground state DOS and DOS projected onto the molecular orbitals for pyridine on graphene. The plot was done with a Gaussian broadening (full width at half maximum) of 0.14 eV.

tions onto the molecular orbitals of pyridine is shown in Figure 5.5. Since the molecule is physisorbed and the interaction is dominated by van der Waals forces, we do not see any significant change in the DOS when compared to that of free standing graphene but for the addition of states contributed by the molecule. The Dirac point of graphene remains at the Fermi level and is not significantly per-

turbed. Since pyridine is a closed shell system with even number of electrons in the valence band, the system remains non-magnetic upon molecular adsorption. Projection of the molecular orbitals of the total system onto the molecular orbitals of pyridine reveals the position of the resonant energy levels of pyridine. The Kohn-Sham HOMO-LUMO band gap of pyridine amounts to about 4 eV and this is supported by other studies using DFT [179].

We now study the electronic and magnetic properties of the system when a hole

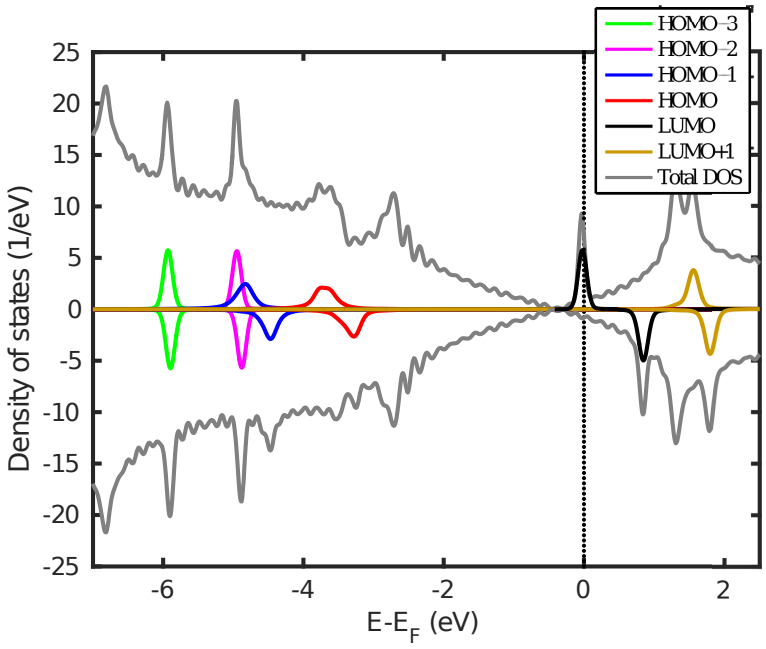


Figure 5.6: The N 1s core excited DOS and DOS projected onto the molecular orbitals for pyridine on graphene. The plot was done with a Gaussian broadening (full width at half maximum) of 0.14 eV.

in the N 1s orbital of the molecule is created and one electron is added to the valence shell, as discussed in simulation details. The total DOS and the MOPDOS of pyridine is shown in Figure 5.6. The attractive potential (created by the core hole) results in a shift of the molecular orbitals to lower energies. One can observe that the Dirac point of graphene in the region of the excited molecule also shifts by

about 0.4 eV to accommodate a fraction of the screening charge. The additional valence electron is mostly located in the LUMO of the molecule just below the Fermi level creating a spin polarized configuration with 1$\mu$B magnetic moment localized on the molecule. We remark that this magnetic configuration would occur upon 1s→LUMO excitation or, in case of photoionization, after the time needed to transfer an electron from graphene to the molecule to screen the core hole. As demonstrated by recent experiments for bipyridine molecules on graphene [146], such electron transfer can occur within the lifetime of the core excitation that, for N and C K shells, is of few femtoseconds [143]. After the core hole de-excites, the evolution of the valence system would depend on the specific final state of the de-excitation and the LUMO would possibly shift to higher energy with electron transfer back to graphene.

We also analyse the spatial charge distribution at the molecular LUMO in the two spin-polarized solutions which arise upon core excitation. This is done by the energy-integrated local density of states (ILDOS) and is defined as:

$$ILDOS(\mathbf{r}) = \int_{E_{min}}^{E_{max}} \sum_{n\mathbf{k}_{||}} \omega_{\mathbf{k}_{||}} \mid \psi_{n\mathbf{k}_{||}}(\mathbf{r}) \mid^2 \delta(E - \varepsilon_{n\mathbf{k}_{||}}) dE, \tag{5.2}$$

where the energy range ($E_{min}$ to $E_{max}$) is chosen to include the molecular LUMO in either the spin-up or spin-down cases. Upon core-excitation, since the spin-up LUMO shifts to the Fermi level where it encounters the Dirac point of graphene, it decouples significantly. This is seen in Figure 5.7 (a) which mainly comprises of the molecular LUMO and almost no states of graphene. The spin-down solution of LUMO is unoccupied and remains above the Fermi level where it couples with the substrate states. This is seen in Figure 5.7 (b) where the molecular LUMO along with the states of the substrate are clearly visible.

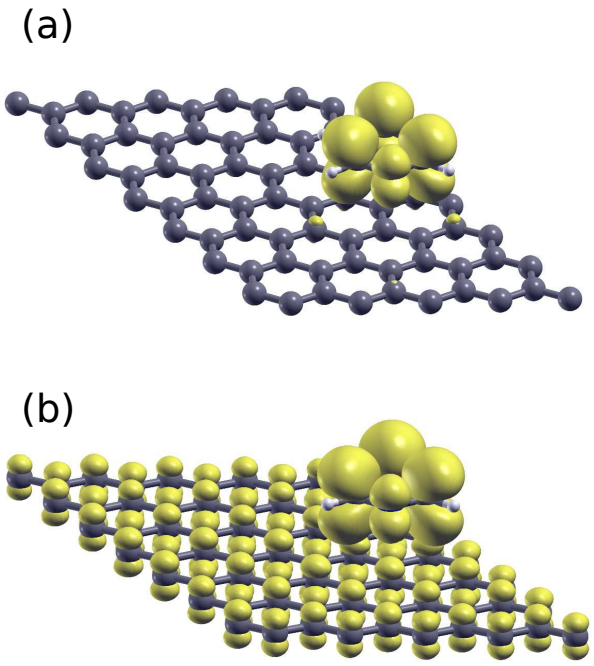


Figure 5.7: The energy integrated local DOS around the core-excited LUMO for (a) spin-up and (b) spin-down solutions.

## 5.4 Picoline and pyridine radicals on graphene

To understand the effect of the adsorption character of core excited organic molecules on the electronic and magnetic properties of graphene, we consider two radicals contrary to the pyridine case. We look at 4-picoline radical ($C_6H_6N$) and pyridine radical ($C_5H_4N$), each with a slightly different adsorption character when interacting with graphene. Pyridine radical mainly interacts via strong covalent bonding with graphene. Picoline radical is considered as an intermediate case between pyridine and pyridine radical where the interaction with the substrate is affected by both van der Waals forces and covalent bonding. The most stable structural configuration of these molecules on graphene is shown in Figure 5.8. In the case of 4-picoline (4-Methlypyridine) radical (where we have removed one of the hy-

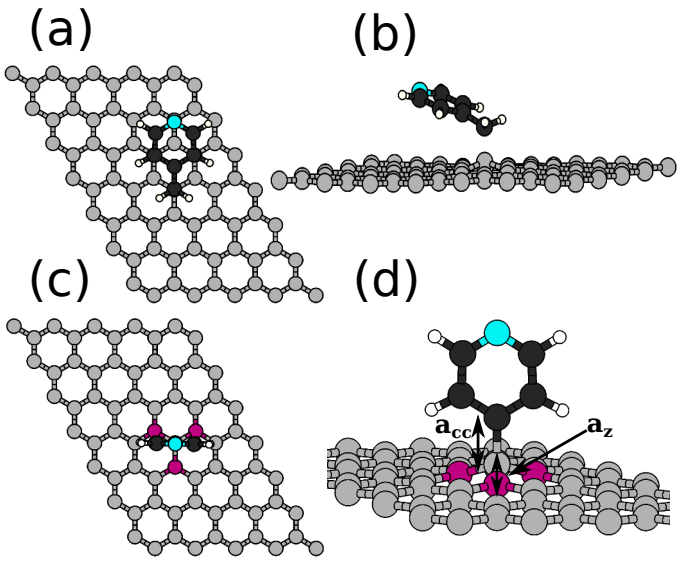


Figure 5.8: The top view and the side view of picoline radical on graphene (a)-(b) and pyridine radical on graphene (c)-(d) in their relaxed configurations. The gray and black spheres represent C atoms of graphene and of the molecule, respectively. The blue spheres stand for N and smaller white ones for H atoms. The perspective view shown in (d) highlights the localized distortion in the graphene lattice when it covalently bonds with pyridine radical. There, $a_{cc}$ represents the molecule-graphene bond length and $a_Z$ is the displacement of the carbon atom of graphene covalently bonded to the radical, as measured with respect to its nearest neighbours.

drogen atoms of the methyl group) which forms a covalent bond with the free $p_z$ orbitals of graphene as shown in Figure 5.8 (a) and (b). For this system, van der Waals forces also play an important role to access the minimum energy configuration since the pyridine $\pi$ cloud remains almost parallel to graphene, at an angle of $\sim 14^\circ$ and at an average distance of 3.16 Å with respect to the substrate plane. Pyridine radical system, when adsorbed on graphene, forms a covalent bond and orients itself perpendicular to the graphene plane as seen in Figure 5.8 (c). Figure

| Configuration | $E_{ads}$ (eV) | $a_{cc}$ (Å) | $a_Z$ (Å) |
|---|---|---|---|
| 4-Picoline radical | -0.51 | 1.64 | 0.41 |
| Pyridine radical | -0.22 | 1.58 | 0.54 |

Table 5.2: The adsorption energies ($E_{ads}$), graphene-molecule bond length ($a_{cc}$) and graphene carbon atom shift ($a_Z$) are tabulated for picoline and pyridne radicals adsorbed on graphene.

5.8 (d) shows the perspective view of this configuration. A localized deformation of the graphene lattice due to covalent interaction with the molecule lifts the carbon atom of graphene [180] by a quantity $a_Z$, defined as the height difference of the bonding carbon atom of graphene with respect to its nearest neighbours. This is visualized clearly in the Figure 5.8 (d) along with the graphene-molecule bond length ($a_{cc}$). These values are summarized in Table 5.2 along with the adsorption energy $E_{ads}$ for the two systems. The results for the adsorption energies are better understood by taking pyridine radical as a reference. Picoline radical, in comparison, shows a larger value of $a_{cc}$ and smaller value of $a_Z$, consistent with its lower reactivity. The more negative computed value of $E_{ads}$ is due to a stronger van der Waal's interaction of its almost planar $\pi$ cloud. In comparing pyridine molecule (addressed in the previous section) versus pyridine radical, we remark that in the case of covalently bonded systems on graphene, the deformation of the substrate requires a large energy cost that significantly lowers the adsorption energy: almost by 1 eV in similar systems[181]. Our adsorption energy value for pyridine radical is comparable to that of other radicals published therein. On the contrary, vdW-bonded pyridine does not suffer this deformation cost and is stabilized by a larger dispersion interaction, hence the overall larger value of $E_{ads}$ as seen in Table 5.1.

We now proceed to plot the ground state DOS of picoline radical/graphene and

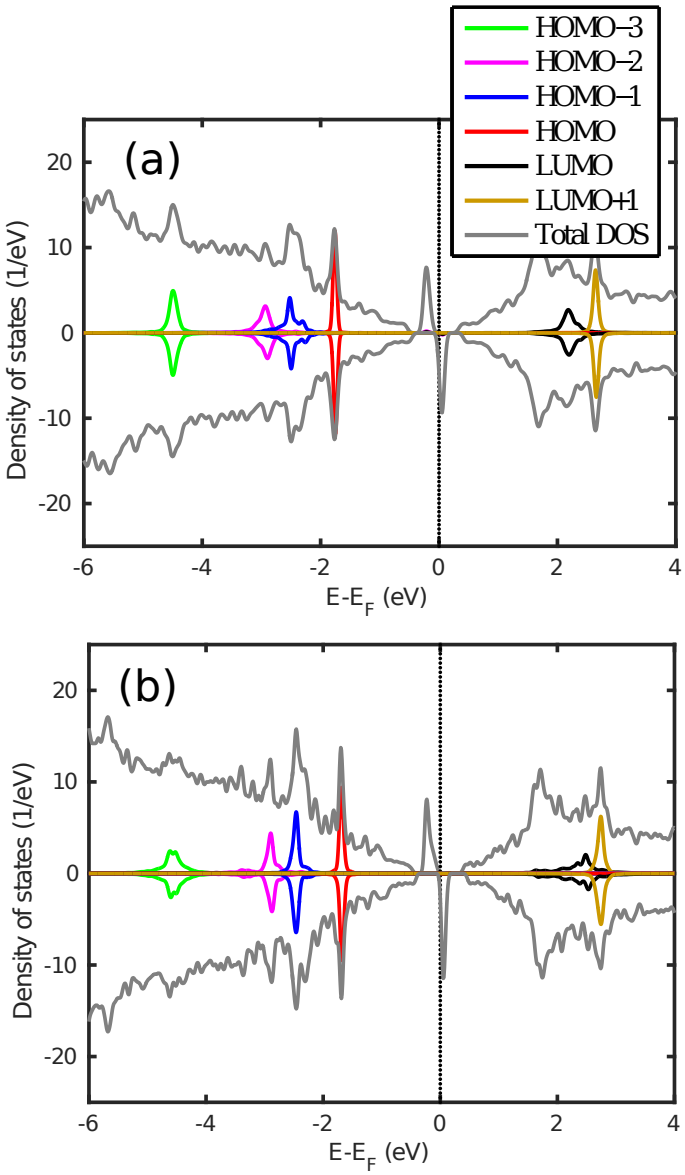


Figure 5.9: The ground state DOS and the molecular projections for (a) picoline radical on graphene and (b) pyridine radical on graphene. The plot was done with a Gaussian broadening (full width at half maximum) of 0.14 eV.

pyridine radical/graphene and the projections of the total DOS onto the molecular orbitals as shown Figure 5.9 (a)-(b) respectively. We recall from the introduction of this chapter that covalent adsorption of species bound to a C atom of graphene

induces magnetism in the ground state of the system, as the respective $p_z$ orbital is taken out of the $\pi$ electron network [45, 180, 181]. This opens a band gap whose value depends on the size of the unit cell used in the calculation. Two localized spin-dependent mid gap states at energies above and below the Fermi level appear and the system gains $1\mu$B magnetic moment. The molecule does not contribute directly to the formation of such states and magnetism is localized around the bonding site on graphene but on the other sublattice [181]. Consequently in the results shown in Figure 5.9 (a) and (b) for 4-picoline and pyridine radicals,respectively, the MOPDOS's reveal that the molecule does not contribute directly to the formation of mid gap states. The main effect on the orbitals of the now-saturated molecule is coupling with the states of the substrate and consequent state-dependent broadening. It is important to realize that different magnetic configurations could be obtained at larger molecular coverage. In particular, adsorption of a second molecule nearby is preferred at the other graphene sublattice and would result into a non-magnetic solution. Adsorption on the same sublattice would lead to ferromagnetic coupling between the two species, but is energetically unfavorable. At large distances between adsorbates, local magnetism would eventually be preserved [180]. Whenever periodic superlattices of covalently bonded species could be formed, long range magnetic order under a magnetic field may be found.[182]

Upon N 1s core excitation, the presence of the core hole creates an attractive potential and the molecular energy levels shift to lower energy values to screen the positive core hole. In the case of covalently bonded 4-picoline radical and pyridine radical, the system is magnetic in the ground state. Upon photo-ionization and relaxation of the valence shell around the core hole, the additional valence electron joins the one formerly in the midgap state and the system valence becomes spin

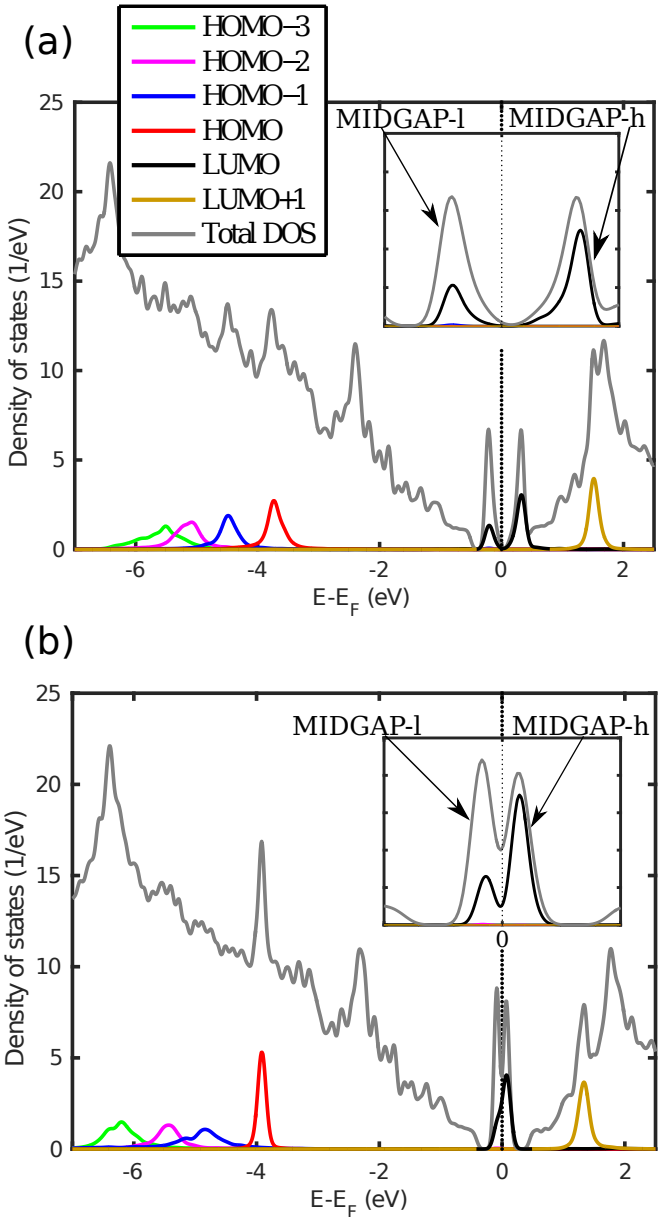


Figure 5.10: The core-excited DOS and the molecular projections for (a) picoline radical on graphene and (b) pyridine radical on graphene. The plot was done with a Gaussian broadening (full width at half maximum) of 0.14 eV.

degenerate. It remains so until the excited hole decays with a lifetime of a few femtoseconds. It is seen for the picoline and pyridine radical cases in Figure 5.10

(a) and (b) respectively, that the LUMO of the molecule shifts down to the Fermi level. There, it hybridizes with the mid gap states of graphene, forming two mixed states at lower and higher energy that we name MIDGAP-l and MIDGAP-h, respectively. We confirm this hybrid LUMO-MIDGAP states by plotting the spatial charge density chosen to include the MIDGAP-l/h states in Figure 5.11. The IL-

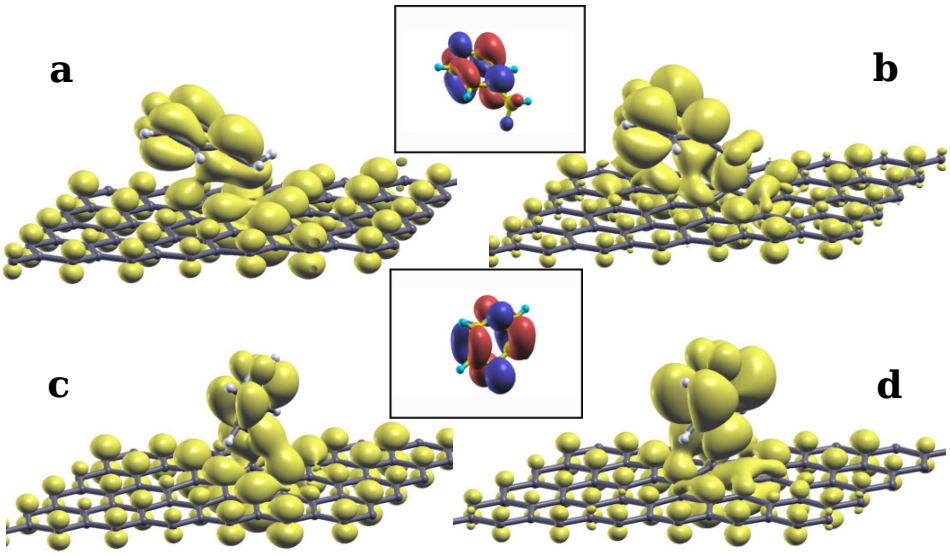


Figure 5.11: Panels (a,b) plot the MIDGAP-l and MIDGAP-h states, respectively, formed by hybridizing the midgap state of graphene with the LUMO of core-excited 4-picoline radical, and showing mostly bonding and anti-bonding amplitude contours, respectively. Panels (c,d) show the same states for a core-excited pyridine radical. Gas phase LUMO for 4-picoline and pyridine are plotted in the insets.

DOS of the occupied MIDGAP-l and the unoccupied MIDGAP-h are plotted in Figure 5.11 (a) and (b), respectively, for the picoline radical, and in Figure 5.11 (c) and (d) for the pyridine radical. The LUMO for gas phase 4-picoline and pyridine molecules are also displayed as insets, confirming that the molecular orbital

contributing to these states is indeed the LUMO, consistently with the projections seen in Figure 5.10 (a) and (b). By examining the relative heights of the peaks in Figure 5.10 (a) and (b) we see that the MIDGAP-l state is derived mainly from the mid gap states of graphene, with smaller weight on the molecule. On the contrary, a lower graphene contribution is displayed on MIDGAP-h which is mainly made up of the LUMO of the molecule.

Additionally, since the pyridine ring is almost parallel to graphene for 4-picoline radical, its LUMO with $\pi$ symmetry couples strongly with the facing $p_z$ orbitals of graphene which constitute the midgap states. This results in a larger energy splitting between the hybrid MIDGAP-l and MIDGAP-h states (0.55 eV) seen in the MOPDOS of Figure 5.10 (a), which is indicative of efficient electron transfer between LUMO and midgap states [183]. Conversely, for the pyridine radical adsorbed normal to graphene, coupling with the midgap state is significantly reduced even though it is not completely forbidden by symmetry, and we find a lower energy splitting between the hybrid MIDGAP-l and MIDGAP-h states (0.14 eV) in Figure 5.10 (b). The same electronic configuration discussed above can be realized by a 1s$\rightarrow$LUMO excitation involving a minority spin core electron. In case a majority 1s state is excited into the valence shell, the spin of the added electron and of the mid gap state sums up leading to a system with 2 $\mu_B$ magnetic moment, eventually occupying singly both MIDGAP-l and MIDGAP-h with the same spin. Such a configuration is less stable than the non-magnetic case by 0.36 eV. Relaxation towards the spin-compensated solution could occur by resonant transfer of two electrons with majority and minority spin to and from the surrounding graphene, respectively, provided this is faster than the core-hole lifetime.

A further difference between the three adsorption cases can be understood by

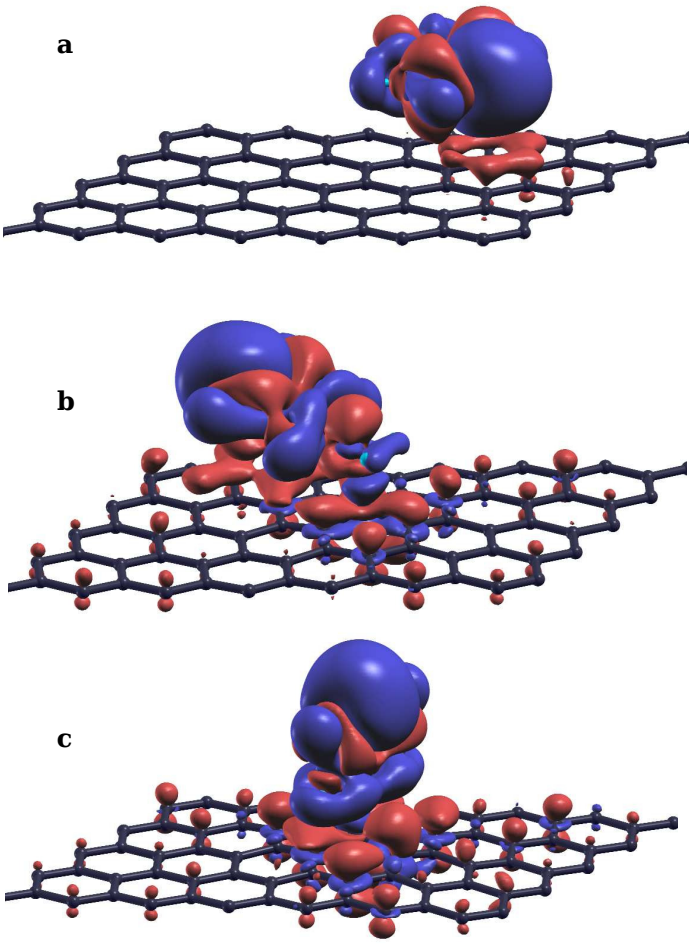


Figure 5.12: Screening charge for (a) pyridine, (b) 4-picoline radical and (c) pyridine radical. The isovalue is 0.0034 e/Å$^3$ and regions of electron accumulation/depletion are depicted in red and blue regions, respectively.

calculating the screening charge which is defined as $\Delta\rho = \rho_{FCH} - \rho_{GS}$ (here $\rho_{FCH}$ and $\rho_{GS}$ are electron density of the system in the core excited and the ground state, respectively), whose integral would amount to additional electron which is added to the valence after the creation of the core-hole. When we consider the screening charge of the physisorbed case shown in 5.12 (a), it is seen that the screening is mainly concentrated in the molecular region upon core excitation and the filling

of LUMO can be appreciated. One can also partition $\Delta\rho$ on the basis of Löwdin population analysis [184, 185] in terms of its projection onto the molecular orbitals and we find that 70% of the added charge can be attributed to the atoms of the molecule and the remaining 30% to graphene. This is in agreement with the occupation of states seen in Figure 5.12 (a).

In the case of the chemisorbed molecules, we have a more pronounced participation by the graphene substrate to the screening: one switches from the spin-polarized mid gap state occupied by one electron, to the spin-degenerate hybrid one. MIDGAP-l depicted in Figure 5.7 (a) and (c), is now doubly occupied. The participation of graphene to the screening charge is moderately larger for pyridine radical than for 4-picoline radical. This can be seen visually by comparing $\Delta\rho$ and noticing that larger charge lobes on graphene are depicted in Figure 5.12 (c) than in Figure 5.12 (b). Correspondingly, the projection of $\Delta\rho$ on the atoms of the molecule amounts to 63% for the 4-picoline radical and 59% for the pyridine radical cases.

Finally we would like to stress that the magnetism observed in these cases deal with a local phenomena without expecting a possible long range magnetic order. with advances in core-level excitation techniques, it is conceivable to detect the local spin balance of the system when the charge transfer occurs from a core-excited molecular LUMO to the substrate states [146]. This can be done by measuring the electron intensity just above the absorption edge and detect the spin state of the low kinetic energy photo-emitted electrons in concurrence with the spin resolved high intensity photoelectrons which emerge due to the charge transfer from the molecular LUMO. The difference between these spin resolved intensities should be detectable in principle, but these experiments are surely at

the limit of todays technology. There have been recent coincidence measurements of the photo- and Auger-electron emissions which have been used to study the local magnetic behavior of ferromagnetic[186] and antiferromagnetic[187] materials, which is done by exploiting the interaction of the relative electron spins and the angular dependence of the emitted electrons. In the case of a distribution of chemisorbed radicals, networks of spin chains could be obtained by long range magnetic order[182]. By the process described in this chapter, the destruction of magnetic correlation in the femtosecond time domain could be induced by core excitation of a few adsorbates under X-ray irradiation.

## 5.5 Conclusions

In this chapter we have discussed the electronic and magnetic properties of ground state and core-excited organic molecules on graphene from first principles. It is shown that the adsorption mechanism plays a vital role in either inducing or suppressing local femto-magnetism in the valence shell of the system within the core-hole lifetime. For a physisorbed system where the interaction is mainly dominated by the van der Waal's forces, the ground state remains non-magnetic but becomes magnetic whe a molecular core electron is excited. The system remains in this magnetic state until the electron de-excites via one of the several decay channels. An opposite behavior can be appreciated when molecules are covalently bonded to graphene and the substrate is initially magnetic in the ground state. Here magnetism is suppressed upon core electron excitation. The LUMO of the molecule hybridizes with the mid gap states of graphene forming spin-compensated bonding and anti bonding combinations. The valence shell remains non-magnetic until the core electron de-excites. Since the time scale of the magnetism we are dealing with is in the order of a few femtoseconds, we find the induction/suppression of a

femtomagnetism in these systems. Detecting this transient magnetism occurring in a femtosecond time scale definitely pushes the boundaries of current experimental techniques. One could think of spin resolved core-hole-clock experiments or other innovative techniques to capture this phenomena. This theoretical study provides fundamental insight into the nature of magnetism in 2-D interfaces.

# Chapter 6

# Organic molecules on graphene/Nickel(111)

In this chapter we discuss the charge transfer lifetimes of N 1s core-excited organic molecules adsorbed on graphene/Ni(111) and bilayer graphene/Ni(111) interfaces. These two cases studied are motivated based on the variable coupling of the graphene layers with metallic Ni. Epitaxial graphene hybridizes strongly with Ni whereas in the case of bilayer graphene the only the bottom layer of graphene interacts strongly with Ni leaving the top layer relatively decoupled. The charge transfer lifetime of core-excited bipyridine adsorbed on these two cases are theoretically calculated and our calculations are validated by experimental core-hole-clock measurements performed by our collaborators (Dr. Dean Cvetko and group) at the Elettra synchrotron.

## 6.1 Introduction

Graphene has been extensively introduced in chapter 2 and chapter 4. Graphene based photo-electronics involve the interaction of graphene with metal electrodes

[188]. Graphene on metals can be synthesized in large area films by chemical vapour deposition[69, 66, 189, 190, 191, 192]. These interfaces play a cruicial role in synergizing graphene within the device architecture. Graphene/nickel(111) interface is found to have the closest lattice match when compared to all transition metals[193]. The interfacial properties of this system is also significant from a fundamental point of view as the effect of Ni substrate alters the electronic and magnetic properties of graphene upon adsorption[194]. Understanding the charge transfer dynamics of these interfaces with organic molecules is paramount in designing efficient graphene based organo-electronic devices[195, 196].

A variety of experimental techniques have been proposed to probe the unoccupied energy levels and study the charge transfer dynamics at the interface such as Core-hole-clock (CHC) spectroscopy[197, 164, 136], two-photon photoemission spectroscopy[198, 199], inverse photoemission spectroscopy[200] and time resolved pump-probe methods[137]. Most of these conventional pump-probe techniques involve an initial short laser (pump) pulse which initiates the core excitation and a second (probe) pulse to study the time evolution of the charge dynamics. The time resolution of these techniques depend on the width of the perturbative laser pulses and the time delay between them[201, 202].

Recent advances in synchrotron-based CHC spectroscopy surpasses these limitations to successfully probe ultrafast charge transfer dynamics at device interfaces. This technique uses the intrinsic core-hole lifetime as a reference to indirectly probe the charge transfer process with resolution in the sub-femtosecond and even the attosecond time scale[203]. In the standard CHC spectroscopy we excite an electron from a chosen molecular core level and populate a particular molecular empty orbital. Provided that the molecular orbital is coupled to the sur-

rounding, the core-excited electron can delocalize from the site of excitation. The spectroscopic details of the core-hole decay, which takes place on the timescale of a few femtoseconds, consequently depend on the localization of the core-excited electron. By measuring Auger emission following the core-hole decay, we can identify the branching of the decay channels in the presence (versus absence) of the core-excited electron. This branching ratio may then be converted into the time scale for the excited electron delocalization.

Several theoretical models within density functional theory (DFT) have been proposed to to probe the charge transfer dynamics at the interface and to extract the elastic resonant charge transfer lifetime. It is necessary to go beyond a finite cluster or a slab model to a semi infinite bulk continuum to truly capture the elastic lifetime without introducing artificial confinement effects[204, 205]. This is implemented by calculating the surface Green's function and the semi-infinite substrate is coupled to the bulk continuum via self energy operators. Due to a fairly localized core-hole, the excited state of the system can be calculated statically for a physically relevant final state and the elastic resonant charge transfer lifetimes can be extracted based on the coupling of the molecular states with that of the substrate[206].

## 6.2 Bipyridine on free-standing graphene

In this section we start by analysing the structural and electronic properties of gas phase 4,4'-bipyridine (BP), the organic molecule which is used in the subsequent excited state calculations. Next we discuss the adsorption configurations of BP adsorbed on free standing graphene (BP/FSG). The structural, electronic and magnetic properties of BP/FSG in the ground state and core-excited one is

studied using a plane-wave code - Quantum Espresso. The method used to calculate core-excited charge transfer lifetimes is explained with a discussion about the drawbacks of this method and in the next section we employ the non-equilibrium Green's function approach to more accurately study these lifetime values.

### 6.2.1 Simulation Details

To address the adsorption of bipyridine on pristine graphene, we make use of ab-initio DFT platform called Quantum Espresso [207]. The system is setup within Generalized Gradient Approximation using Perdew-Burke-Ernzerholf (PBE) exchange correlation functional [95, 96] and a plane wave basis set. Grimme correction is used to take into account non-local van der Waals interaction [208]. Bipyridine is adsorbed on a $5\times7$ graphene supercell periodic in the $x-y$ plane and a vacuum separation of 15 Å in the $z$ direction. The plane wave kinetic energy cut-off is 42 Ry and the convergence on the energy and force are $10^{-4}$ a.u. and $10^{-3}$ a.u. respectively. The Brillouin zone is sampled using a $15\times14\times1$ $\Gamma$ - centered k-mesh for calculating the system energy and $90\times84\times1$ $\Gamma$ centered mesh for the density of states calculations corresponding to a $1\times1$ unit cell. The excited state calculations are done using a pseudopotential with a full core hole (FCH) at the N 1s orbital of the molecule. The FCH calculation is performed considering a globally neutral system with the positive core balanced by an additional electron in the valence band. The peaks of the molecular orbitals upon projection is usually a pseudo-Voigt profile with a user defined external Gaussian broadening convoluted with the intrinsic Lorentzian broadening which occurs due to molecular coupling. In our calculations we have introduced a known external Lorentzian broadening whose width adds up with the intrinsic Lorentzian width of the molecular states. This width can later be extracted and we can fit the intrinsic Lorentzian peak and

calculate the lifetime.

### 6.2.2 Gas phase bipyridine

The relaxed structure of gas phase 4,4'-Bipyridine $(C_5H_4N)_2$ along with the relevant bond lengths (d*mn*) and bond angles (a*lmn*) are shown in Figure 6.1. Isolated BP molecule in gas phase can be considered as two pyridyl ring linked by a single bond in a twisted conformation [209]. The relaxed molecular structure is in good

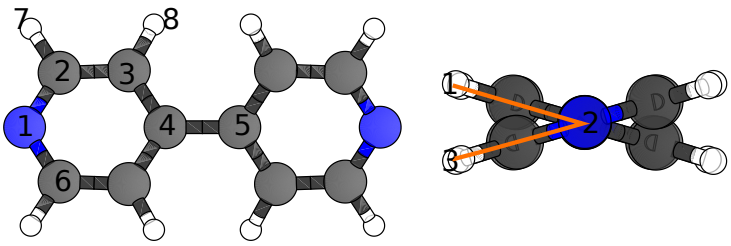


d12 = 1.34 Å
d16 = 1.34 Å
d23 = 1.39 Å
d34 = 1.40 Å
d45 = 1.48 Å
d27 = 1.09 Å
d38 = 1.09 Å

a612 = 116°
a127 = 116°
a123 = 123°
a723 = 120°
a238 = 120°
a234 = 120°
a834 = 121°
a345 = 122°

t123 = 32°

Figure 6.1: The relaxed structure of gas phase 4,4'-bipyridine in the top and side view, with the relevant bond lengths (d*mn*) and bond angles (a*lmn*) are summarized. From the side view, the torsional angle between the pyridine rings (t*lmn*) is shown.

agreement with previously published results [209]. We find the relaxed gas phase torsional angle between the two pyridyl rings to be 32° and one must note that this conformation lies in a shallow energy landscape between 30-40 degrees and is in agreement with several expterimental and theoretical studies [210]. The gas phase

molecular orbitals of BP is plotted in Figure 6.2. From the molecular orbitals one

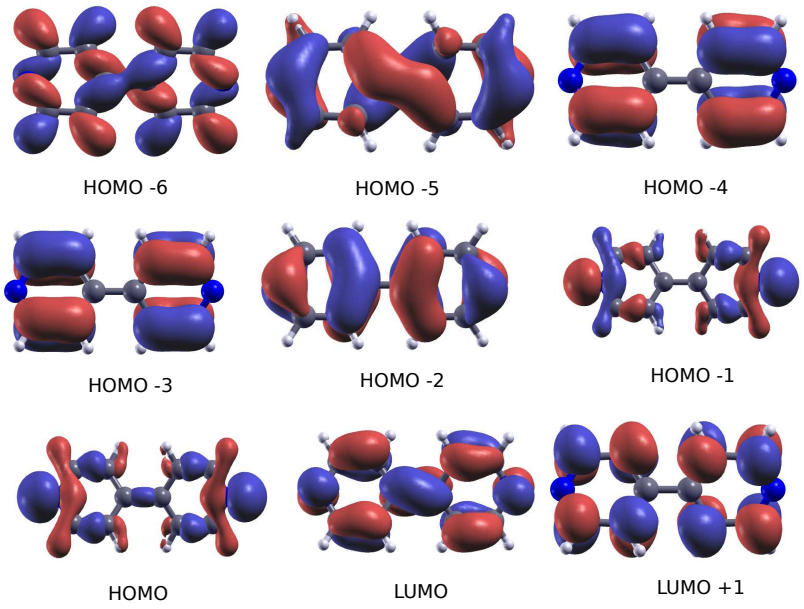


Figure 6.2: The gas phase molecular orbitals of BP from HOMO-6 to LUMO+1 are plotted.

can see that HOMO and HOMO-1 form $\sigma$ bonding/anti-bonding molecular orbitals and LUMO consists of $\pi$ orbitals. Molecular orbital symmetry plays a key role in the hybridization of the state with the substrate and this is illustrated in the following sections. We also plot the electronic density of states (DOS) for gas phase BP in Figure 6.3.

### 6.2.3 Adsorption structure on graphene

We now study the possible adsorption configurations of BP on free standing graphene (FSG) shown in 6.4. The nomenclature of these configurations are based on the position of the N atoms with respect to the graphene substrate and the axis connecting these N atoms with respect to the configuration of graphene below (armchair/zigzag graphene). The classification depends on whether the N atom of

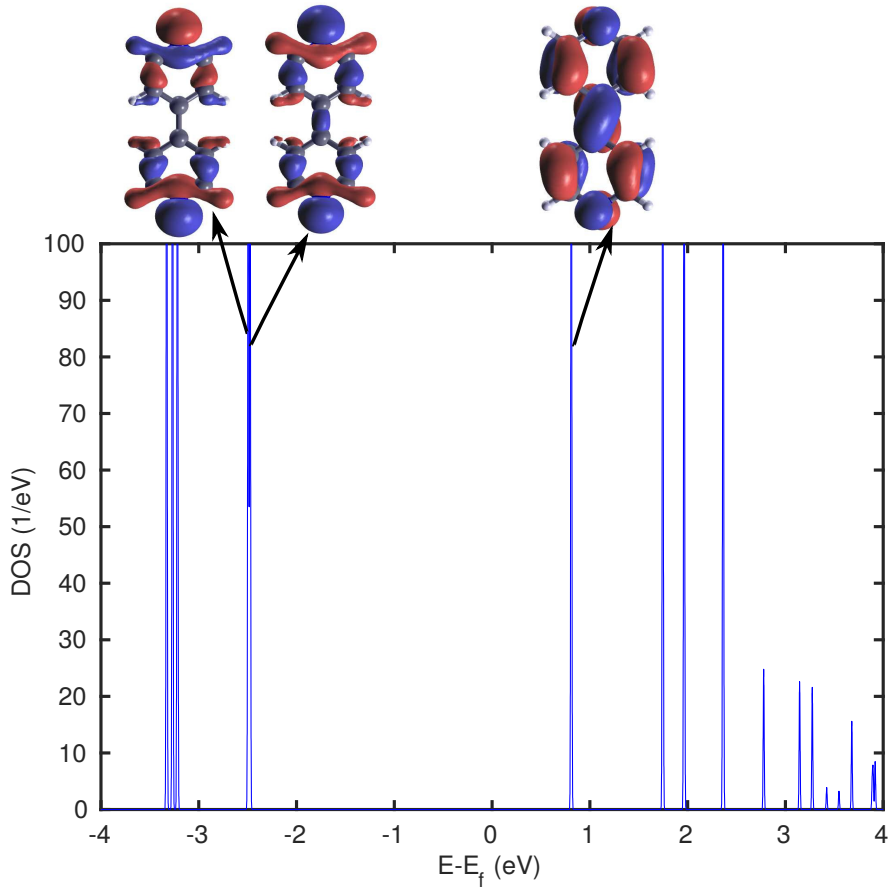


Figure 6.3: The gas phase DOS of BP shows HOMO and HOMO-1 are almost degenerate. The molecular orbitals are of σ bonding/anti-bonding character. The LUMO and its gas phase molecular orbital is also indicated. A small Gaussian broadening of 0.001 eV is used for these plots to highlight these nearly degenerate orbitals.

the molecule adsorbs at the center of the graphene ring (Center- C) or on top of a carbon atom of graphene (Top- T). By taking into account the translation and rotational degrees of freedom, the three adsorption geometries considered are CC-ZigZag, CT-Armchair and TT-Armchair which is shown in Figure 6.4(a,b,c) respectively. The adsorption energies $E_{ads}$, the graphene-molecule bond length

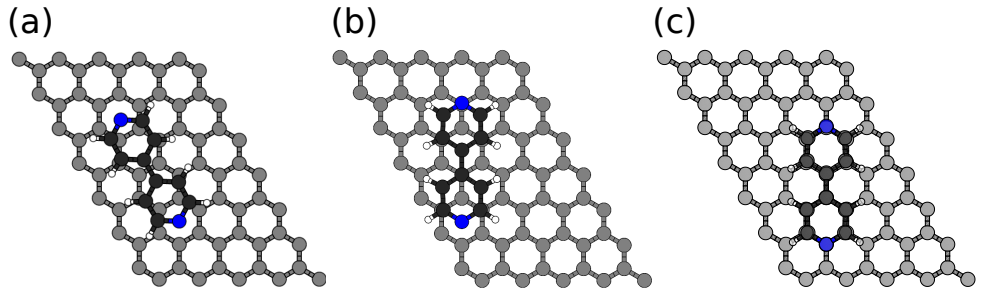


Figure 6.4: The adsorption configurations of BP/FSG are named based on the position of the N atom of BP with respect to graphene and the axis joining the the two N atoms of the molecule either transverse an armchair or zigzag configuration of graphene below. (a) CC-Zigzag: the two N atoms are at the center of the graphene ring and the axis joining the N atoms transverse a zigzag graphene configuration. (b) CT-Armchair: One of the N atoms is at the center of the graphene ring and the other on top of a C atom of graphene. The axis passes through an Armchair configuration of graphene. (C) TT-Armchair: The two N atoms are on top of graphene C atoms and the axis passes through an Armchair configuration of graphene.

$a_{gm}$ and the torsional angle of the molecule upon adsorption θ are summarized in the Table 6.1. The adsorption energy is defined as $E_{ads} = E_{g+m} - E_g - E_m$. Here $E_{g+m}$ is the total energy of the optimized molecule-graphene system, $E_g$ and $E_m$ are the total energies of the isolated graphene substrate and of the gas phase molecule respectively. The adsorption bond length $a_{gm}$ is defined as the distance between the average graphene plane with respect to the N-N axis of the molecule. The torsional angle θ is the angle made between the pyridyl rings of the molecule. The most stable configuration of BP/FSG is the one where the N atoms of the molecule is at the center of the graphene ring and the other on top of a C atom of graphene, with its axis passing over an armchair configuration of graphene. An interesting point here is that the molecule flattens considerably upon adsorption.

| Configuration | $E_{ads}$ (meV) | $a_{gm}$ (Å) | θ° |
|---|---|---|---|
| CC-Zigzag | -752 | 3.23 | 9.5 |
| CT-Armchair | -782 | 3.09 | 9.2 |
| TT-Armchair | -679 | 3.34 | 9.7 |

Table 6.1: The adsorption energies ($E_{ads}$), graphene-molecule bond length ($a_{gm}$) and the torsional angle (θ°) is tabulated for the various configurations of bipyridine on graphene.

The gas phase torsional angle of 33° is reduced significantly to 9° upon adsorption on graphene. We utilize this configuration as a starting point when we study the adsorption of BP on graphene/metal substrates which will be discussed in the following sections.

### 6.2.4 Ground and excited state electronic properties

We now study the electronic and magnetic properties of this system in the ground and N 1s core-excited states. This is done by calculating the DOS of the system and projecting it onto the molecular orbitals of BP as defined in the previous chapter. Figure 6.5 (a) shows the ground state DOS plots of BP/FSG. One can see that due to a weak van der Waals interaction of the molecule with the substrate, the Dirac point of graphene at the Fermi level is well preserved. The total DOS BP/FSG in the ground state is very similar to that of pristine graphene except for the addition of states from the molecule. Upon projection of the total DOS onto the molecular orbitals, the Kohn-Sham band gap (the distance between the HOMO and LUMO) is $\sim$ 3.2 eV which is in close agreement with the gas phase molecule band gap 3.3 eV seen in Figure 6.3. This reaffirms the weak molecular interaction

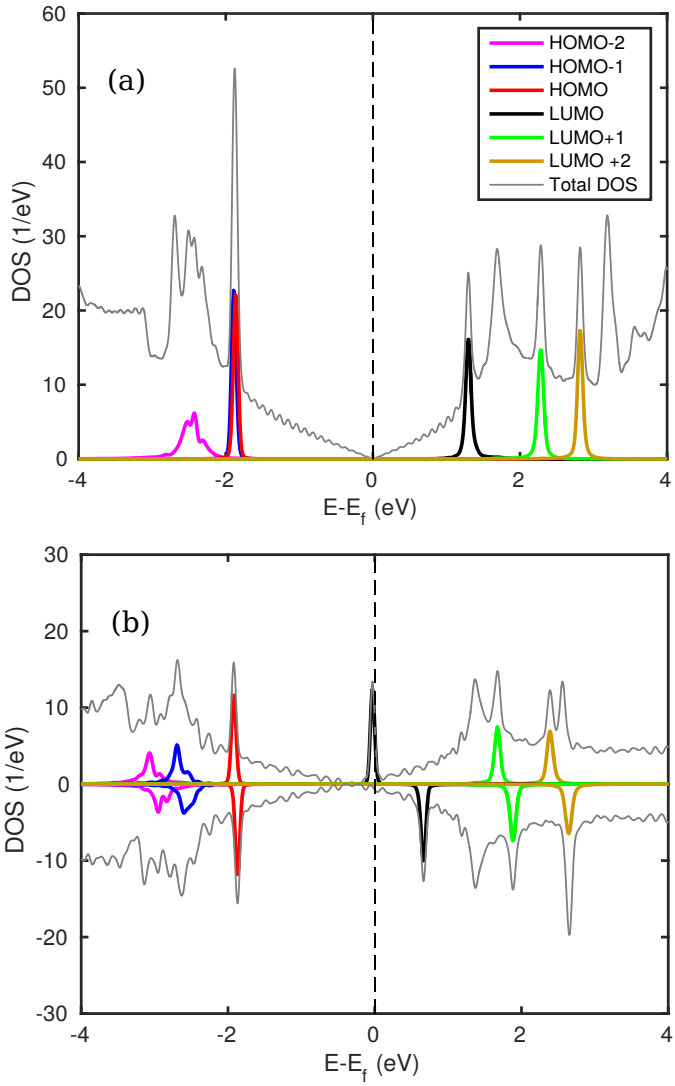


Figure 6.5: The total system DOS and its projections onto the molecular orbitals of BP in the ground state (a) and the N 1s core-excited state (b) is shown. We use a Lorentzian broadening of 0.04 eV is used for the molecular projections.

with graphene. The HOMO and HOMO-1 are very close in energy as seen in the gas phase case. The system in the ground state is non-spin polarized and the dynamics of this phenomenon is explained in the previous chapter. Figure 6.5 (b) shows the N 1s core-excited DOS of BP/FSG. It is seen that upon core-excitation,

the molecular orbitals shift to lower energy values for screening the positive core hole. The valence of the system now has an additional electron which is accommodated in the LUMO of the molecule. The LUMO shifts to the Fermi level and the system reaches a spin-polarized solution with a spin-up LUMO fully occupied and a spin-down LUMO unoccupied and above the Fermi level. The system now becomes magnetic with a $1\mu$B magnetic moment on the molecule. HOMO and HOMO-1 which were degenerate in the ground state split to different energies upon core-excitation.

## 6.3 Bipyridine on graphene/metal interfaces

We now examine the effect on the charge transfer lifetime of N 1s core-excited bipyridine (BP) layer formed on two different graphene systems; the epitaxial graphene (EG) with strong electronic coupling to the Ni(111) substrate and the bilayer graphene (BLG), where the outermost graphene layer is effectively decoupled from the substrate beneath, thus closely resembling that of a freestanding graphene [211].

### 6.3.1 Simulation Details

In this section we discuss the numerical setup used simulate the properties of bipyridine (BP) molecules on graphene/metal interface and to extract the resonant charge transfer lifetime from the molecular orbitals in the presence of core-level excitations. For this purpose, we model a semi-infinite substrate to better describe a bulk continuum of electronic states. We utilize the Green's function formalism within density functional theory (DFT) [212, 213] as implemented in the SIESTA/TranSIESTA [214, 215] quantum transport package. A break-junction

setup employed for the calculations of molecules adsorbed on a semi-infinite substrate which better describes the bulk continuum as shown in Figure 6.6. A 9

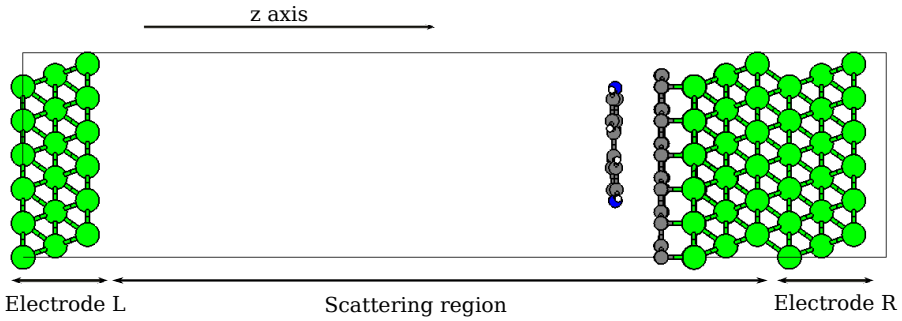


Figure 6.6: The break junction setup shows three layers of Ni as electrodes on either sides which are coupled to bulk continuum by self energy operators. The central scattering region is asymmetric with the molecule adsorbed on one side and the two regions are decoupled by a large vacuum separation of 35Å.

layer periodic Ni slab in the form of an asymmetric break-junction setup with 6 layers on one side and three layers on the other. The three leftmost and rightmost layers of Ni seen in Figure 6.6 are the electrodes which couple to the bulk by self-energy operators. The central asymmetric scattering region consists of three layers of Ni with epitaxial/bilayer graphene and bipyridine adsorbed on these surfaces. The two regions are separated by a large vacuum region of 35 Å along the transport direction to ensure minimal interaction between the periodic images and an almost constant electrostatic potential between the asymmetric leads. Along the $x-y$ plane, we setup a periodic $6\times6$ surface supercell to simulate low coverage of molecular adsorption. The top and side views of BP/EG/Ni and BP/BLG/Ni are shown in Figure 6.7 (a-b) and (c-d) respectively. We adopted

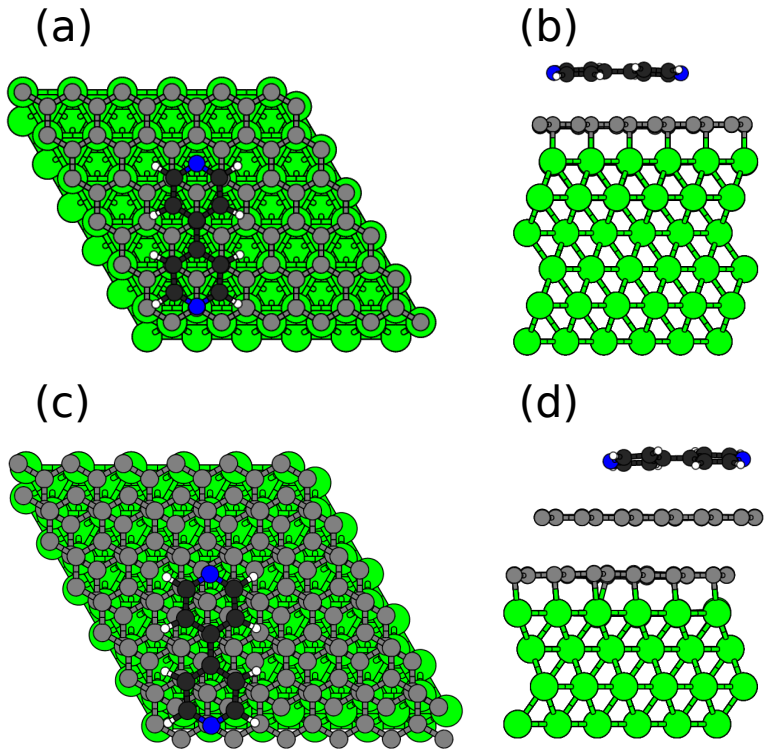


Figure 6.7: (a) The top view of the system geometry shows the 6×6 supercell with bipyridine adsorbed on epitaxial graphene/Ni(111) (BP/EG/Ni) substrate and (c) bipyridine on bilayer graphene/nickel(111) (BP/BLG/Ni). The side view for the BP/EG/Ni (b) and BP/BLG/Ni (d) shows a part of the break junction setup where the molecule is adsorbed. The last three layers of Ni is coupled to a bulk electrode.

a fully non-local van der Waals exchange-correlation functional as proposed by Klimes, Bowler and Michaelides (vdW-KBM) [113] with a real space grid cutoff of 300 Ry. A localized basis set consisting of double zeta polarized orbitals is used for all the atoms in the system. A Γ-centered Monkhorst-Pack k point mesh corresponding to a 36×36 mesh in the 1×1 Ni(111) unit cell is used to sample the surface Brillouin zone. We assume a close epitaxial matching of graphene lattice with that of the Ni(111) surface, given the small lattice mismatch of free-standing graphene with nickel (less than 1.5 %, with a lattice constant of 2.51 Å

in agreement with previous calculations [216]). Following previous studies of graphene on Ni(111) [217, 218, 64, 219], we modeled EG/Ni in the atop/fcc-hollow configuration, where the nomenclature refers to the underlying Ni sites. For BLG/Ni, a second graphene layer was added with C atoms stacked in the AB configuration with the graphene underneath. The top layer of graphene is in the hollow configuration with respect to the nickel substrate where the top most nickel atom aligns at the center of the graphene. Given the fairly large unit cells and the dispersive nature of the interaction with graphene, the adsorption site of bipyridine is chosen on the basis of our analysis for the molecule on free standing graphene (BP/FSG). Taking into account translational and rotational degrees of freedom, the most stable configuration of the molecule is when one of the N atom is above a graphene atom and the other at the center of a graphene hexagon. This is further optimized for BP/EG/Ni and BP/BLG/Ni with results shown in Figure 6.7. An average molecule-graphene distance of BP/EG/Ni is 3.04 Å (3.06 Å for BP/BLG/Ni) is computed. The molecule flattens upon adsorption reducing the torsional angle between the phenyl rings from a gas phase value of 37° to 11° and 18° for BP/EG/Ni and BP/BLG/Ni respectively.

To model the electronic properties of these systems in presence of a core-level excitations as in the experiments, we replace the standard pseudopotential of the N atom with one having a full core hole (FCH) in the 1s orbital. The FCH calculation is performed considering a globally neutral system with the positive core balanced by an additional electron in the valence band. This efficiently simulates the final state of x-ray resonant photo-absorption or a photoemission experiment where the valence shell relaxes around the core hole and an electron from the substrate is attracted towards the molecular region [206, 176, 147]. The Green's function approach has been previously employed to study the charge transfer dynamics

with considerable success [220, 138, 206, 147]. The density of states projected onto a localized molecular state $\phi(r)$ can be computed in terms of the Green's function of the surface as

$$\begin{aligned}\rho_\phi(E) &= \frac{1}{\pi}\Im[G_{\phi\phi}(E)] \\ &= \frac{1}{\pi}\Im[\int dr \int dr' \phi^*(\mathbf{r}) G(\mathbf{r},\mathbf{r}',E)\phi(\mathbf{r}')]\end{aligned} \tag{6.1}$$

The dynamics of the population of a localized state $\phi(r)$ can be accurately described by $\rho_\phi(E)$ and the full width at the half maximum (fwhm, $\Gamma$) at these projected peaks gives the resonant lifetime of an electron initially populating that particular state as $\tau = \hbar/\Gamma$.

### 6.3.2 Epitaxial graphene on Ni(111)

We are now in a position to study the electronic and magnetic properties of graphene/metal systems. The first system considered in epitaxially grown graphene on Ni(111) (EG/Ni) surface. Atop/fcc-hollow configuration is found to be the most stable structure as discussed in the previous section and the structure is shown in Figure 6.8. Next we proceed to study the electronic properties of EG/Ni. This system has been well studied previously [217, 218, 64, 219] and our intention is to check the robustness of our setup before proceeding with molecular adsorption on such systems. The bulk Ni DOS (shaded region) and the total DOS of $1\times1$ EG/Ni projected onto the molecular orbitals of graphene is shown in Figure 6.9 . It is seen from Figure 6.9 that graphene hybridizes strongly when adsorbed on Ni(111). The strong coupling of EG with the states of nickel leads to opening of bandgap in graphene and this breaks the symmetry and leads to large midgap-like states at the Fermi level [56]. This nomenclature has been borrowed from the midgap states that is seen in graphene when molecules are covalently adsorbed [181]. The

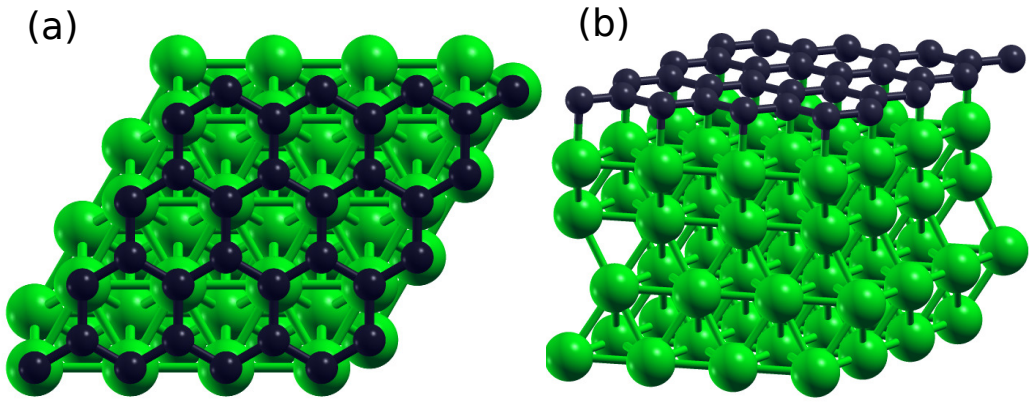


Figure 6.8: (a) The top view and (b) the side view of epitaxial graphene/Ni(111) in the relaxed Atop-FCC configuration.

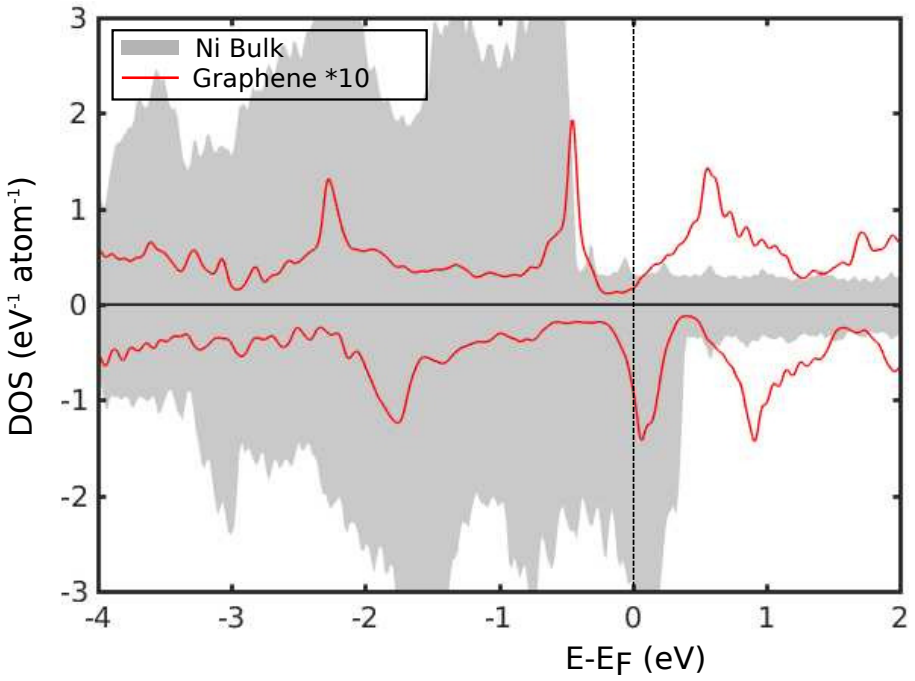


Figure 6.9: The bulk DOS of Ni and DOS of $1\times1$ EG/Ni projected onto the orbitals of epitaxial graphene. The DOS plots use a Gaussian broadening of 0.08eV.

upper and lower panels in Figure 6.9 refer to the spin-up and spin-down solutions respectively. The spin-up and the spin-down band structures of this system are

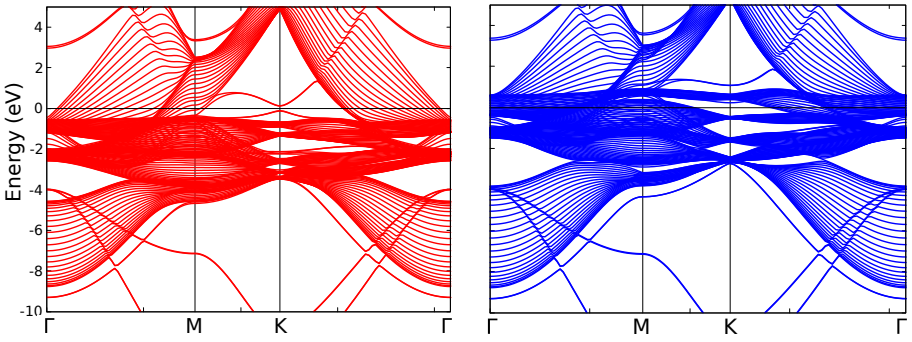


Figure 6.10: The band structure plot of epitaxial graphene/Ni(111) for the (a) spin-up and (b) spin-down solutions along $\Gamma - M - K - \Gamma$.

also plotted in Figure 6.10 (a) and (b) respectively. This not only shows the magnetic configuration of Ni but also reflects the induction of magnetism in graphene upon strong coupling with the Ni substrate. At the $k$ point corresponding to the Fermi level in Figure 6.10 (a), we see the opening of bandgap in graphene which is in good agreement with previous results [219]. Therefore, to summarize this section, the strong interaction of graphene with Ni(111) leads to large mid-gap like created at the Fermi level.

### 6.3.3 Bilayer graphene on Ni(111)

We now examine bilayer graphene on Ni(111) (BLG/Ni), which presents an interesting contradiction with EG/Ni. In the BLG/Ni case, the bottom layer of graphene which is in contact with Ni strongly hybridizes forming the large 'midgap like' states as seen in the previous section. But the top layer of graphene remains relatively decoupled from the Ni substrate and a close approximation to freestanding graphene [211]. The stable configuration of this system (which has been discussed earlier) is Atop-FCC configuration of the bottom layer of graphene with Ni and the top layer forms an AB stacking with the graphene below. The top and the

side views of BLG/Ni is shown in Figure 6.11. The nature of interaction of bilayer

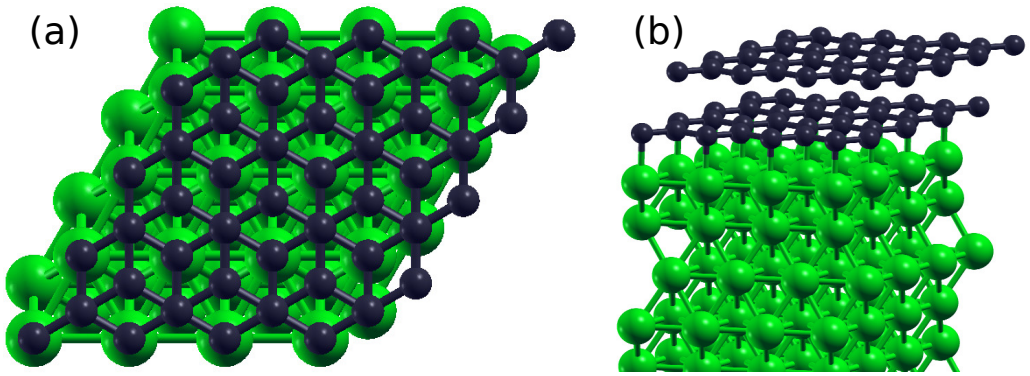


Figure 6.11: The (a) top and (b) the side views of relaxed structure of bilayer graphene on Ni(111).

graphene with Ni(111) becomes more appearant by looking at the DOS of this system which is plotted in Figure 6.12. Here we plot the bulk Ni DOS (the shaded region, the projections of the $1\times1$ BLG/Ni onto the molecular orbitals of bottom layer of graphene (dotted black curve) and top layer of graphene (red curve). It is clear from the DOS that the bottom layer of graphene, which is in contact with Ni hybridizes strongly with the orbitals of Ni and form large midgap-like states close to the Fermi level. But the top layer of graphene weakly interacts with the substrate and relatively undisturbed. The top layer does feel a weak dipole upon interaction and contributes small states close to the Fermi level. In the next section we shall study the effect of core-excitation of an adsorbed molecule in these two cases and calculate the charge transfer lifetime to better understand the effect of the substrate.

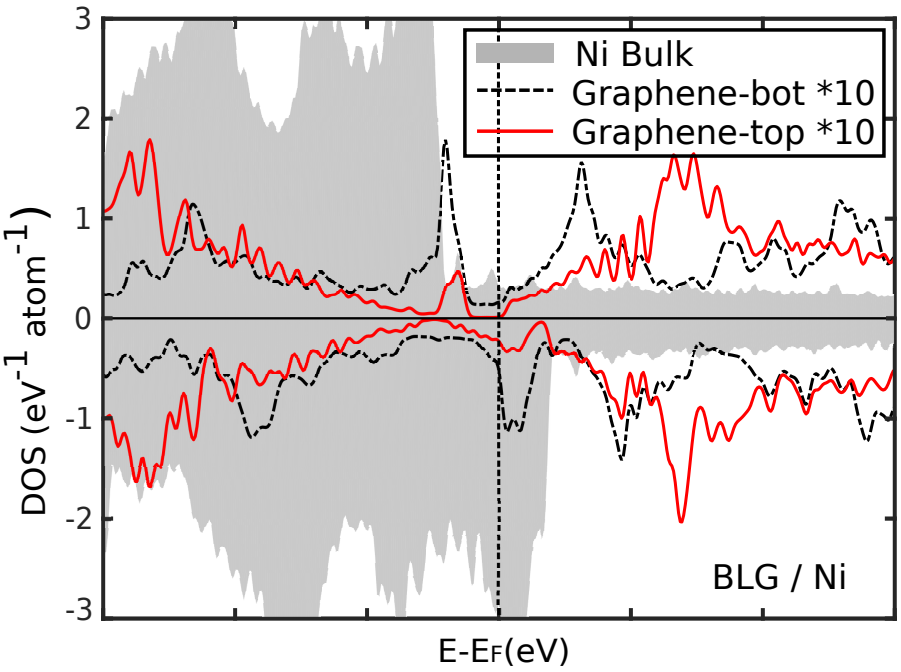


Figure 6.12: The bulk DOS of Ni and DOS of $1\times1$ BLG/Ni projected onto the orbitals of epitaxial graphene. The DOS plots use a Gaussian broadening of 0.08eV.

### 6.3.4 Bipyridine on epitaxial graphene/Ni(111)

From the section on BP/FSG, it is clear that BP interacts weakly via van der Waals forces with the substrate. The initial relaxed configuration of bipyridine on epitaxial graphene/Ni(111) (BP/EG/Ni) is shown in Figure 6.7 (a-b). To understand the electronic properties of this system and extract the charge transfer lifetime we plot the DOS and its projection on the molecular orbitals of BP. In Figure 6.13 we plot the total DOS of the system, its projections on graphene and the projections onto the ground and the N 1s core-excited states of BP molecular orbitals. From the projections on graphene we see the presence of large mid-gap like states close to the Fermi level which arise due to the strong electronic coupling the $p_z$ states of graphene with the $d_{z^2}$ orbitals of Ni(111). When BPY is adsorbed on EG, the electronic DOS of the graphene layers is minimally altered due to the dominant

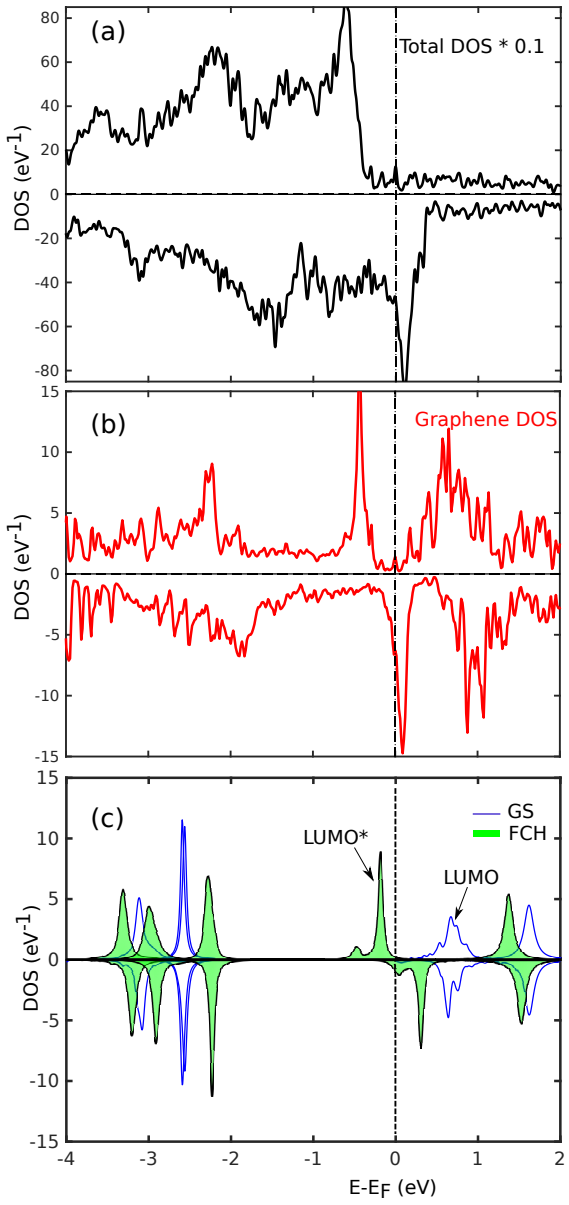


Figure 6.13: (a) The total GS DOS of BP/EG/Ni, (b) The projections onto graphene layer, (c) The projections onto the ground state (unshaded blue) and the N 1s core-excited state DOS of BP molecular orbitals. The DOS uses a Gaussian broadening of 0.04 eV and the BP molecular orbital projections use a Lorentzian broadening of 0.04 eV.

dispersion character of the interaction. This is reflected in the well-defined peaks seen in the DOS of the full system, upon projection on the individual molecular orbitals of bipyridine, that is reported as unshaded curves in Figure 6.13 (c). HOMO and HOMO-1 orbitals upon adsorption are similar to gas phase BP reaffirming the weak interaction. The molecular LUMO, in the ground state is at 0.7 eV. The width of the molecular LUMO in the ground state is $\Gamma$=161 meV. One can also note that even though the substrate is spin-polarized the molecule in the ground state remains non-magnetic.

To study the charge transfer dynamics of this system as can be measured by the core-hole-clock method discussed in section 6.3.6, we need to include the influence of the core-hole in the simulation as this is fundamental for the alignment of the molecular energy around the Fermi level and its filling. To this purpose, the total DOS of the N 1s core-excited system, projected on the molecular orbitals of bipyridine, is plotted in Figure 6.13 (c) (shaded curves). The effect of the core hole is seen in the shift of the molecular orbitals to lower energies to screen the positive charge. The additional core-excited electron is accommodated in the molecular spin-up LUMO which now shifts to the Fermi level. The molecule gains a 1$\mu$B magnetic moment until the core-electron de-excites. The LUMO at the Fermi level (LUMO*) hybridizes strongly with the midgap-like states of graphene and the intrinsic width is 20 meV. The corresponding theoretical lifetime of the core-excited electron at LUMO* is $\sim$ 33 fs.

### 6.3.5 Bipyridine on bilayer graphene/Ni(111)

Now we study the electronic properties of bipyridine on bilayer graphene/Ni(111) (BP/BLG/Ni). This system is an experimentally viable contradictory case to

BP/EG/Ni. As we saw in the section about BLG/Ni, the bottom layer of graphene hybridizes strongly with Ni but the top layer remains fairly decoupled. Adsorption of bipyridine on the top layer of graphene is a close approximation of BP/FSG which is experimentally challenging to construct. We say this system is in contrast to the BP/EG/Ni case because the charge transfer lifetime directly depends on the width of the molecular orbitals (which is a consequence of the orbital-substrate coupling). Since FSG has no states at the Fermi level, the molecular LUMO effectively decouples and has 0 width (and infinite charge transfer lifetime theoretically). Since the top layer of bilayer graphene is an approximation to FSG, one can expect that the states of graphene close to the Fermi level are significantly smaller when compared to EG/Ni. Upon core-excitation, one would expect to see a significant decoupling of the molecular LUMO* and a much larger charge transfer lifetime value when compared to BP/EG/Ni.

The Figure 6.14 shows the total DOS of the system, its projections onto the bottom and top layers of graphene and the projections onto the ground and the N 1s core-excited states of BP molecular orbitals. We have already established the adsorption mechanism of bilayer graphene on Ni. When BP is adsorbed on this substrate, the weak interaction of BP doesnot significantly change the DOS of the substrate. The LUMO of BP in the ground state, the unshaded curves seen in Figure 6.14 (d), is at 1.4 eV. There is a shift of 0.7 eV with respect to the ground state LUMO of BP/EG/Ni. This shift of molecular orbitals in BP/BLG/Ni towards lower binding energies can be attributed to the stronger screening of the bottom layer of graphene. The LUMO of BP/FSG also occurs at similar energy value of 1.3 eV which affirms the resemblance of bilayer graphene system with that of free standing one and that these energy offsets are relatively orbital independent. The width $\Gamma$ of the LUMO in the BP/BLG/Ni case is 89 meV and for BP/FSG is 31 meV. These values when compared to BP/EG/Ni ( $\Gamma$=161 meV) highlights the

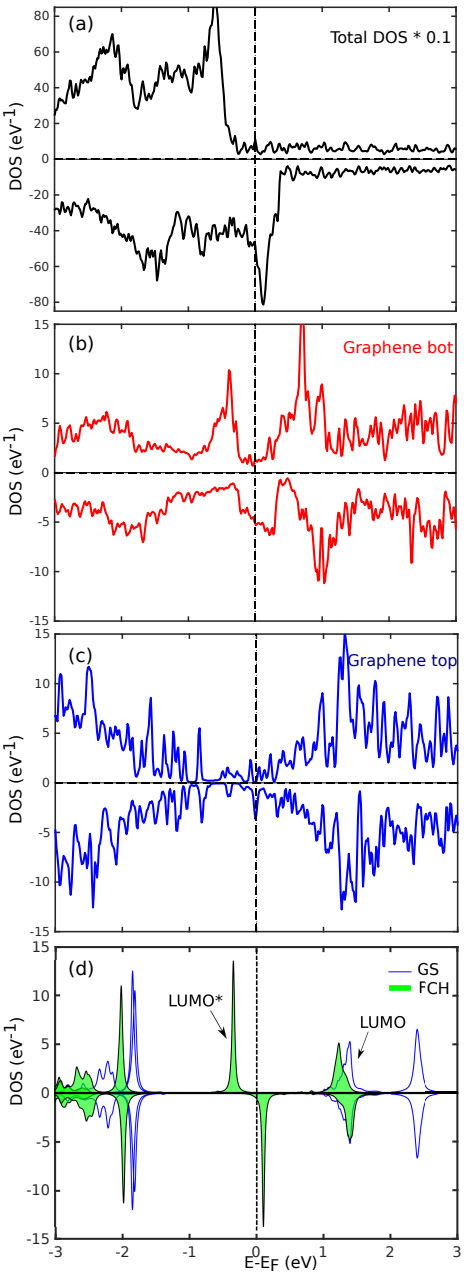


Figure 6.14: (a) The total GS DOS of BP/BLG/Ni, (b) The projections onto bottom graphene layer, (c) Projections onto top layer of graphene, (d) The projections onto the ground state (unshaded blue) and the N 1s core-excited state DOS of BP molecular orbitals. The DOS uses a Gaussian broadening of 0.04 eV and the BP molecular orbital projections use a Lorentzian broadening of 0.04 eV.

finer details about the decrease in the electronic coupling as we move from the BP/EG/Ni to BP/FSG cases.

Upon N 1s core-excitation of the molecule, as seen in the previous cases, the molecular orbitals shift to lower energy values to screen the positive core hole. The spin-up LUMO is occupied and shifts to the Fermi level. Since the molecule is mainly interacting with the top layer of graphene (which is in close resemblance to FSG and has very few states close to the Fermi level), we see that the molecular LUMO significantly decoupling from the substrate. This decoupling leads to a decrease in the width of LUMO and an increase in the charge transfer lifetime. The intrinsic width $\Gamma$ of LUMO* amounts to 6 meV (20 meV) for BP/BLG/Ni (BP/EG/Ni), corresponding to a resonant lifetime of $\sim$ 116 fs ($\sim$ 33 fs). Therefore we can see a clear effect of a substrate which interacts strongly with graphene on the charge transfer lifetimes of physisorbed organic molecules on them.

The local density of states integrated around the LUMO$^*$ of bipyridine for the two cases is plotted in Figure 6.15. A visual distinction between the two cases is the charge density on graphene. We see that for BP/BLG/Ni case, the LUMO$^*$, which upon excitation shifts to the Fermi level, finds very few states of graphene to couple with unlike the case of BP/EG/Ni. This is clearly visible when comparing Figure 6.15 (a) and (b). We also plot the LUMO of gas phase bipyridine molecule in the inset to reconfirm that it is indeed the LUMO of the molecule which exists at the Fermi level upon core excitation of the molecule.

We would also like to point out that the limiting case is that of bipyridine adsorbed on pristine graphene, that we present to further clarify the above results. Here, due to the unique DOS of graphene with the presence of the Dirac cone at the Fermi level (and therefore the absence of substrate states at the Fermi level) as

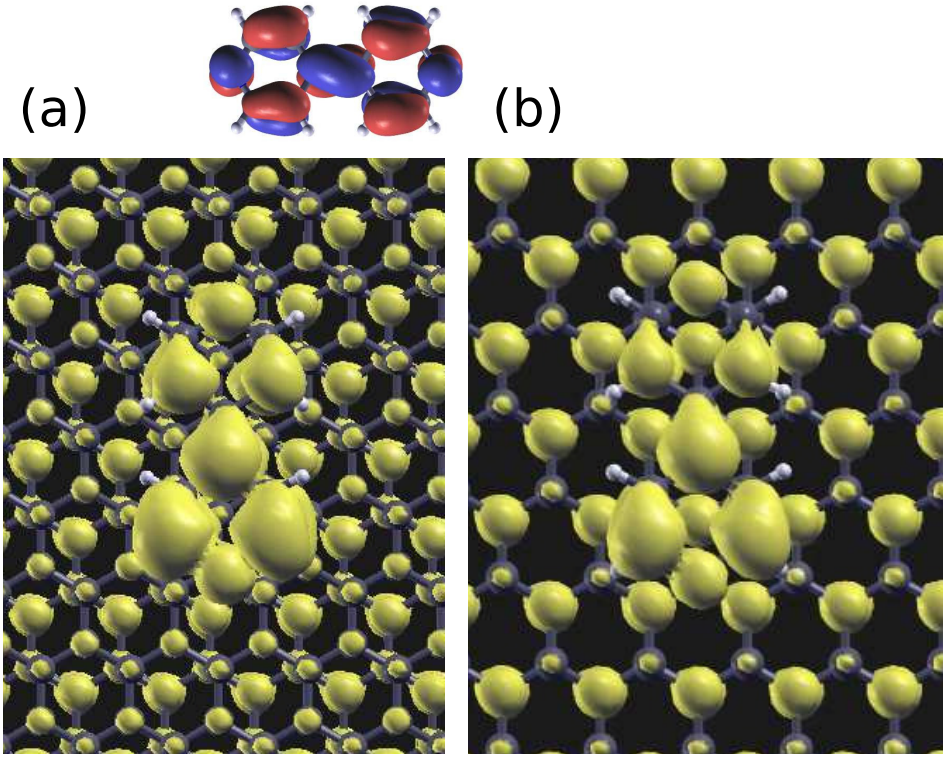


Figure 6.15: The integrated local density of states around LUMO* for (a) BP/BLG/Ni and (b) BP/EG/Ni with an isovalue of 0.0005e/Å$^3$ is depicted. The inset shows the gas phase LUMO of bipyridine.

seen in Figure 6.5 (b), the theoretical modeling predicts a completely uncoupled LUMO* upon core excitation with an infinite resonant lifetime. As seen in Figure 6.5 (a), molecular states of bipyridine on pristine graphene in the ground state have very similar energies to BP/BLG/Ni case (Figure 6.14 (d)). Due to the weak interaction of the molecule with graphene, the Dirac point is not significantly perturbed by adsorption. But upon photo-emission of a core level electron and complete relaxation of the valence shell, the molecular orbitals move to lower energies as seen in the previous cases, with a spin-majority LUMO* mostly below the Fermi level to accommodate an additional electron. The LUMO* now encounters the Dirac point of graphene where no states are found, so it completely decouples from the

substrate producing, in principle an infinitely sharp state with $\tau = \infty$ (this hypothetical picture is only approximately reproduced in actual simulations because of finite size of the surface unit cell). Clearly, this neglects all dynamical effects in evaluating Kohn Sham eigenvalues for the final state time-independent Hamiltonian, as well as phononic perturbation and lattice defects that would influence a measured lifetime, yielding to the overestimated theoretical value. The pathological cases of Kohn Sham eigen values for systems with very low DOS are reflected in the transfer lifetimes.

### 6.3.6 Experimental Results

In this section we present the experimental evidence supporting our calculations performed by our collaborators Dr. Dean Cvetko (DC), *et.al.* at the Elettra Synchrotron in Trieste, Italy and the figures reported here are courtesy of DC. The characterization of the system is performed using near-edge x-ray absorption fine structure (NEXAFS) and x-ray photoemission spectroscopy (XPS). The experimental setup used to study the the resonant charge transfer lifetimes of these systems are by the means of X-ray resonant photo-emission (RPES) and core-hole-clock (CHC) spectroscopy.

#### Sample preparation and characterization

Graphene layers on Ni(111) substrate was prepared under ultra high vacuum conditions (UHV) by ethylene deposition and subsequent annealing, following procedures reported in [221]. The Ni(111) and graphene/Ni(111) substrates have been characterized by XPS and UV photo-emission. All experiments were performed at the ALOISA and HASPES beamlines of the IOM laboratory at Elettra

synchrotron in Trieste. Coupling of graphene with Ni substrate was monitored by angle resolved UV photo-emission with He II photon line at 40.8 eV. Characteristic dispersion of the graphene $\pi$ band along the $\Gamma - K$ and $\Gamma - M$ was used to identify the prevalent presence of EG/Ni and BLG/Ni phases. 4,4'-bipyridine molecules were evaporated from a temperature controlled Knudsen cell. The C 1s, N 1s and Ni 3p X-ray photo-emission was used to check the chemical composition of the BP molecular film. Near edge absorption fine structure (NEXAFS)

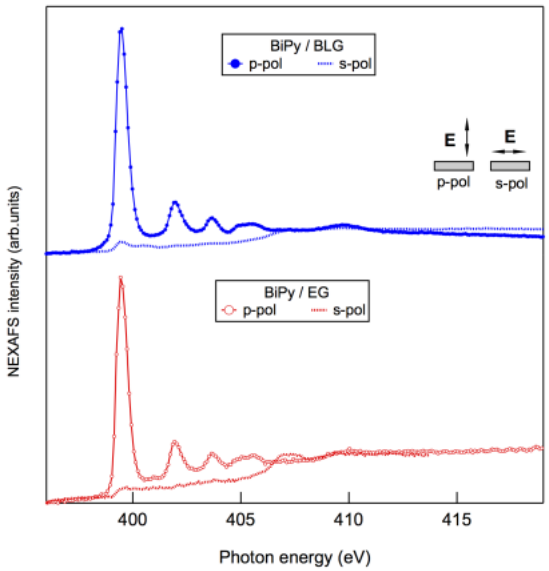


Figure 6.16: NEXAFS spectra in p-polarization (continuous lines) and s-polarization (dashed lines) for BP/BLG/Ni (blue color, upper panel) and BP/EG/Ni (red color, lower panel). The direction of the electric field in the two polarizations is depicted in the inset.

of C and N K-edges was used in *s-pol* (electric field parallel to the surface) and in *p-pol* (electric field normal to the surface) to measure the molecular adsorption geometry. As seen in figure 6.16, BP/EG/Ni and BP/BLG/Ni monolayer films display a very strong and almost identical linear dichroism of the N1s $\rightarrow$ LUMO transition, from which an almost flat lying adsorption geometry at an average

angle of 16° (BP/EG/Ni) and 20±3° (BP/BLG/Ni) can be deduced, taking into account both tilt and twist of the molecule. These are in good agreement with theoretically calculated values of 11° and 18° respectively. Figure 6.17 shows the

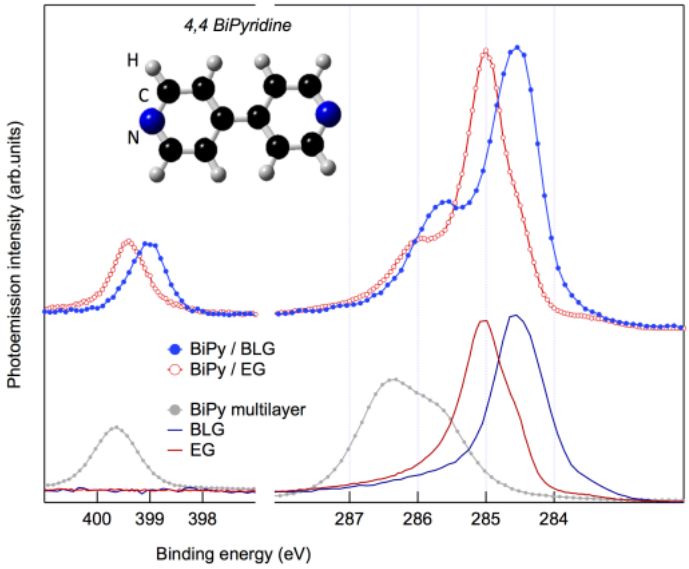


Figure 6.17: Lower panel: Carbon 1s XPS from bare EG/Ni (red curve) and BLG/Ni (blue curve), as well as N1s and C1s XPS from bipyridine multilayer (black markers). Upper panel: N1s and C1s XPS of bipyridine monolayer on EG (red markers) (BP/EG/Ni) and BLG (blue markers) (BP/BLG/Ni). The bipyridine molecular structure is shown in the inset.

C1s and N1s x-ray photo-emission spectra (XPS) for both EG and BLG systems, before (lower panel) and after (upper panel) adsorbing bipyridine. The C1s peaks for EG and BLG cases before adsorption of bipyridine are at 285 eV and 284.6 eV binding energies respectively. The XPS spectrum of BP multilayer film is also shown in figure 6.17 (Black markers) which shows a single N1s peak at 399.8 eV and C1s doublet at 285.6 and 286.4 eV belonging respectively to 4 C atoms next to N ones and to the 6 remaining carbons within the BP molecule. BP/EG/Ni and BP/BLG/Ni spectra (figure 6.17 upper panels) are qualitatively similar to the BP

multilayer apart from the rigid shift to lower binding energies. This shift amounts to 0.4 eV for both N1s and C1s core levels and is in agreement with the C1s shift seen for clean EG/Ni and BLG/Ni main peaks. We recall that this shift to lower energies can also be appreciated from the ground state DOS plots of BP/EG/Ni and BP/BLG/Ni. This indicates that the modified electronic structure between the the EG/Ni and BLG/Ni phases are equally reflected in the energy level offset of orbitals upon molecular adsorption.

**Electron transfer dynamics**

The electron transfer dynamics of BP/EG/Ni and BP/BLG/Ni are studied by resonant photo-emission spectroscopy (RPES). Figure 6.18 (a)-(b) shows RPES for BP multilayer and BP/EG/Ni respectively, in the form of intensity color map of the photon energy (vertical axis) versus the electron kinetic energy (bottom axis). These maps are comprised of photo-emission scans taken at a series of incident photon energies tuned across the N K absorption edge. Non-resonant components in the photo-emission spectra (due to direct photo-emission from the BP orbitals and also from the substrate) has been measured below the resonant edge (at hν=395 eV) and subtracted from all spectra throughout the entire photon range. As the photon energy is scanned through the LUMO resonance (hν=394 eV) of the photo-emission spectra, in addition to the broad Auger line peaked at 385 eV, sharp resonant photo-emission peaks coinciding with the direct photo-emission from the molecular orbitals (HOMO-n, n=0,1,2..., indicated in figure 6.18 (b) by vertical black arrows) are also seen. These are called *participator* resonances, where the excited electron participates in the decay of the core-hole and an Auger electron from the filled molecular orbital is elastically emitted. Single RPES spectra for multilayer and BP/EG/Ni, taken at the LUMO resonance (hν=394 eV) are respectively shown in the lower panels of the figure 6.18.

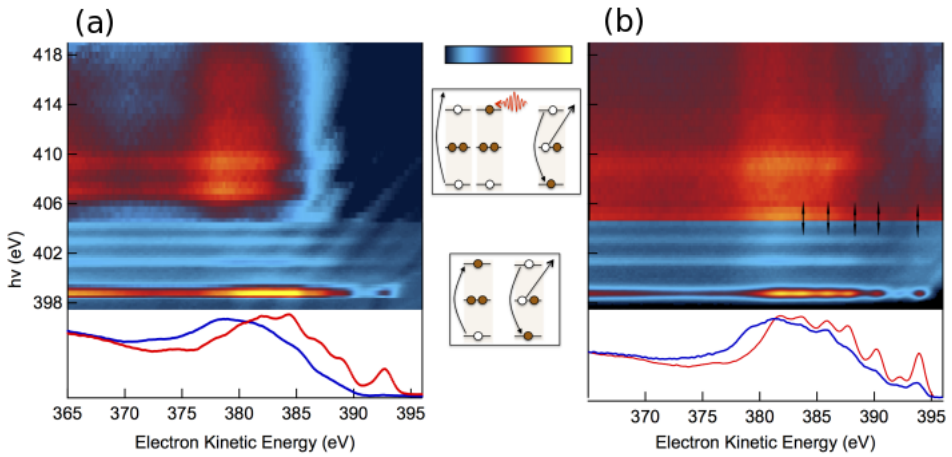


Figure 6.18: (a) Nitrogen K-edge RPES map for BP multilayer and (b) BP/EG/Ni. Single resonant photo-emission scans at N 1s$\rightarrow$ LUMO$^*$ resonance (h$\nu$=399.3 eV) and above the edge (h$\nu$=414eV) are shown in the bottom panels. Additional Auger-like features, observed above the edge (h$\nu$ $>$ 405 eV) for the BP/EG/Ni in (b) but not for the BP multilayer (a) correspond to the super participator decay of the N1s core hole, where an electron is transferred to the LUMO$^*$ from the EG/Ni. The energy level diagram of super participator and participator peaks are illustrated in the inset.

Note that the single RPES spectra taken at the LUMO resonance are quite similar for both multilayer BP and BP/EG/Ni and they resemble non resonant, direct photo-emission spectra of the respective systems. Quite different spectral features may be observed for photon energies above the absorption edge (e.g. for h$\gamma$ $>$405 eV, also shown in the lower panels of figure 6.18 (a-b). In particular, for BP/EG/Ni system, almost identical photo-emission peaks as measured at LUMO resonance are observed throughout the photon range. These may be seen by the vertical spectral lines in the 2D map of figure 6.18(b), as they appear at constant kinetic energy. They coincide with the participator peaks at the LUMO resonance.

These features, termed as *super participator* (SP) peaks, are characteristic of fast electron injection from the substrate to the LUMO* , as LUMO* aligns below the Fermi level during the core hole lifetime [147]. As a consequence of the substrate, the electron transferred to the LUMO* may participate in the core-hole decay of the molecule giving rise to identical, non-dispersing RPES spectra throughout the entire photon energy. By analyzing the intensity of SP and P peaks relative to the participator intensity of the multilayer BP, we can obtain the charge injection time of $\tau_{EG} = 4fs \pm 1fs$, as detailed in [146]. The direct comparison of the nitrogen

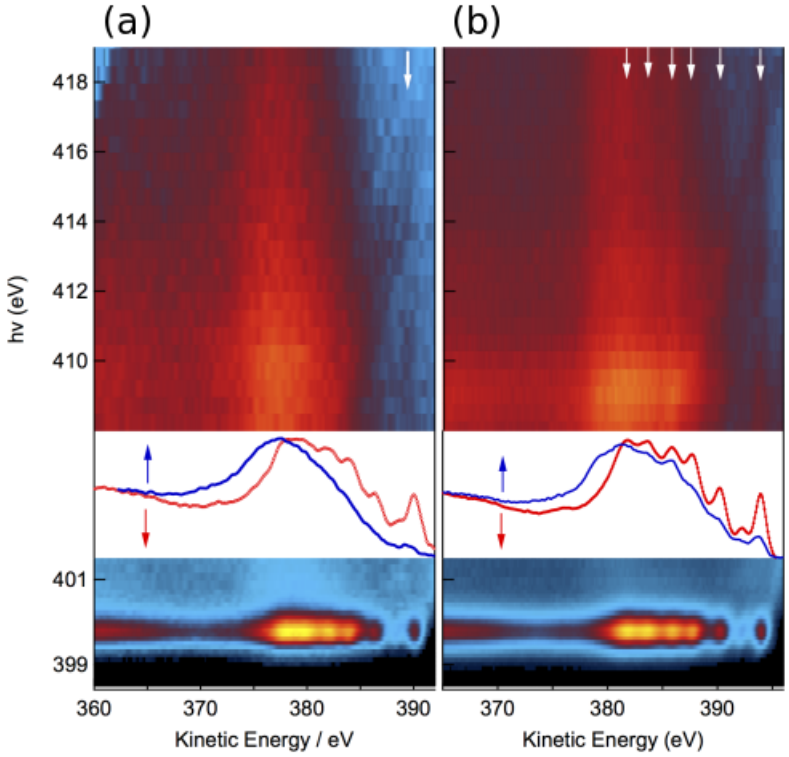


Figure 6.19: Direct comparison of N K-edge RPES maps for (a) BP/BLG/Ni and (b) BP/EG/Ni. Single resonance PE scans (red color, hν= 399.3 eV) and above the absorption edge (blue color, hν=414 eV) are shown in the middle panels.

RPES maps for BP/EG/Ni with BP/BLG/Ni systems are shown in figure 6.19. An almost identical resonant spectrum is seen at the LUMO resonance for both these

cases but the superparticipator lines above the ionization edge in the BP/BLG/Ni are strongly attenuated. The relative intensity of the SP lines in the BP/BLG/Ni is almost completely quenched yielding $\tau_{BLG} = 30fs \pm 5fs$. This indicates that the electron transfer times at the organic/graphene interface is strongly slowed due to the poorly interacting graphene layers.

## 6.4 Conclusions

The two cases of bipyridine adsorbed on bilayer graphene/Ni and epitaxial graphene/ Ni(111), which differ by the coupling of graphene with the metal substrate, have been studied and the resonant charge transfer times at the interface has been computed theoretically. These values have been further validated by our experimental collaborators (DC et. al.) by performing core-hole-clock measurements. In the case of bilayer graphene/Ni, the layer of graphene in contact with the metal couples strongly with the substrate and its electronic structure is significantly influenced, similar to epitaxial graphene/Ni. But its top layer remains relatively uncoupled and presents properties quite similar to that of free standing graphene. The molecular electronic properties in the case of BP/BLG/Ni displays a rigid shift to lower energies (seen in the MOPDOS) when compared to that of BP/EG/Ni signifying a decoupling of the top graphene layer from the Ni substrate. We find that upon core excitation of a N 1s orbital of bipyridine, the molecular orbitals shift to lower energies to screen the core hole. The LUMO* shifts to about the Fermi level and becomes partially occupied attracting electrons from the substrate. For bipyridine on graphene/Ni(111), the substrate states at the Fermi level couple strongly with the molecular LUMO* and fast charge transfer time of $\sim$ 33 fs is calculated. On bilayer graphene/Ni, the molecular LUMO* now encounters the relatively undisturbed Dirac cone of graphene and remains less coupled to sub-

strate states. This increases the resonant charge transfer lifetime to $\sim$ 116 fs. A key aspect of this study is understanding the nature of molecular coupling on a substrate and its relationship on the charge transfer lifetime. The presence of a core hole acts as a perturbation on the system and the electronic properties of the system are a response to this. The logical extension of this study would be to include phononic and many body effects to capture the dynamics of the molecular coupling. The static state approximation under which this study was performed builds a fundamental understanding of the charge transfer processes with relevant applications in organo-electronic devices.

# Chapter 7

# Conclusions

Graphene based devices are envisioned to play a key role in the future of electronics. In this thesis we contribute towards understanding the fundamental properties of organic/graphene interfaces. We study the electronic, magnetic and conductive properties of graphene based systems from first principle calculations using DFT. In the first part of this work, we deal with the electronic and magnetic properties of ground and core-excited organic molecules adsorbed on graphene. Pyridine physisorbs via weak van der Waals forces on graphene and in the ground state the system is non-magnetic. Upon N 1s core excitation of the molecule, the molecular energy levels shift to lower energies to screen the positive core hole. The system considered in neutral with an additional electron added in the valence band. This corresponds to photo-emission of the core electron and backtransfer of an electron from the substrate which is accommodated in the molecular LUMO. When the valence shell relaxes around the core hole, the spin-up LUMO gets filled and shifts below the Fermi level and the spin down LUMO remains unoccupied and above the Fermi level. This leads to a spin polarized solution until the core electron decays which is in the order of a few femtoseconds (the typical core-hole lifetime). Therefore we see a femtosecond induction of magnetism

(with a 1$\mu$B magnetic moment on the molecule) when a physisorbed molecule adsorbed on graphene is core-excited. In contrast, when organic molecules are chemisorbed on graphene(like picoline radical or pyridine radical), in the ground state the system is magnetic due to the spin-dependent midgap states on graphene. These midgap states arise due to the loss of the $p_z$ orbitals of graphene when it covalently bonds with the organic radical. The magnetic moment on graphene is localized around the adsorption site and is present on the inequivalent C atoms of graphene alternate to the one participating in the adsorption. Upon core-excitation of the molecule, the molecular LUMO which is now partially occupied with the backtransfered electron and shifts to the Fermi level. Here it hybridizes with the midgap states of graphene and forms a fully occupied bonding molecular orbital (MIDGAP-l) and an unoccupied anti-bonding solution (MIDGAP-h). This leads to a non-spin polarized solution until the decay of the core-hole. Therefore, in core-excited chemisorbed molecules on graphene, we see a suppression of magnetism in graphene on a femtosecond timescale. Since the time scale of the magnetism we are dealing with is in the order of a few femtoseconds and considering the recent advances in femtomagnetism and ultrafast measurements for adsorbed molecules, this work provides an interesting insight into the behavior of magnetism in 2-D graphene systems.

We then proceed to study the electronic couping of graphene (and bilayer graphene) with a metal substrate and the effect of N 1s core-excited organic molecules adsorbed on them. These systems are of interest because most organic overlayers need to be coupled to a metal electrode at a device level and the charge transfer dynamics at these interfaces play a crucial role in determining the device performance. N 1s core electron of 1,1'- bipyridine is photoexcited and adsorbed on bilayer graphene/Nickel(111) and epitaxially grown graphene on Ni(111). In

the case of bilayer graphene/Ni(111), the $p_z$ orbitals of the graphene layer hybridizes strongly with the $d_z^2$ orbitals of Ni surface. This leads to strong "midgap" like peaks in the DOS, contributed by the bottom graphene layer at the Fermi level. The top layer of graphene remains relatively uncoupled from the substrate and the DOS of the top layer shows very few states close to the Fermi level. The adsorption of a weakly interacting bipyridine molecule does not significantly distort the substrate electronic structure. Upon N 1s core-excitation of the molecule, the molecular LUMO shifts to the Fermi level and is partially occupied with a backtransfered electron. The LUMO decouples strongly from the substrate since there are very few states of the top layer graphene at the Fermi level and increases the lifetime of the state significantly ( 116 fs). But in the case bipyridine on epitaxial graphene/Ni(111), the strong hybridization of graphene with the underlying nickel substrate significantly distorts the electronic structure of graphene generating states close to the Fermi level. The core-excited LUMO* of the molecule strongly couples with these states resulting in a substantially smaller lifetime ( 33 fs). We also consider an ideal case of bipyridine on free standing graphene. It is known that free standing graphene has no states at the Fermi level due to the presence of the Dirac cone. When the core-excited LUMO* shifts to the Fermi level in this case, it completely decouples from the substrate and theoretically has $\infty$ lifetime. This hypothetical picture is only approximately reproduced in actual simulations because of finite size of the surface unit cell. Although our calculations neglect all dynamical effects in evaluating Kohn Sham eigenvalues for the final state time-independent Hamiltonian, as well as phononic perturbation and lattice defects that would influence a measured lifetime, we can successfully predict the trend of these lifetimes. This is confirmed experimentally by performing core-hole-clock spectroscopy for these two systems. For the case of bipyridine/bilayer graphene/Ni(111) the experimentally measured charge transfer lifetime is 30 fs

and for bipyridine/epitaxial graphene/Ni(111) it is 5 fs. Thus we clearly demonstrate the effect of substrate on the charge transfer dynamics of organic molecules on graphene.

From our studies, one can understand and appreciate the nuances of charge transfer dynamics and energy level alignment at organic molecule/graphene interfaces. The interaction of graphene with metallic substrates further accentuates this fundamental understanding and provides valuable information to move towards graphene based organo-electronics.

# Appendices

# Appendix A

## Numerical codes adopted

### Quantum Espresso

Quantum Espresso (QE) - Quantum opEn Source Package for Research in Electronic Structure Simulation and Optimization is a full *ab initio* package for calculating the electronic structure and linear response methods like phonon dispersion curves, dielectric constants and also third order anharmonic perturbation theory calculations [174]. It also contains quantum molecular dynamics codes like Car-Parinello molecular dynamics (CPMD) and first principle molecular dynamics (FPMD). It is also equipped to perform excited state calculations like x-ray absorption spectra and time dependent density functional perturbation theory.

Following the Born-Oppenhimer approximations, QE can solve the KS equations self-consistently for static nuclear positions. The system wavefunctions are represented here by a plane wave basis set. The static inner core of the system represented by the ionic potential (nuclei and the core electrons) is approximated by a pseodupotential (PP). The PP's can be described by separable norm-conserving PP's [222], Ultrasoft PP's [223, 117] or Projector-augmented wave (PAW) [224] sets. Various exchange-correlation functionals within the frame-

work of local density approximation (LDA) or generalized gradient approximations (GGA) are available [225]. Further extension to Hubbard $U$ corrections, meta-GGA's [226] and hybrid functionals are included to explain non-local interactions [227, 228]. The code follows a periodic boundary condition which effectively treats infinite crystalline systems using supercells and also efficient in converging large aperiodic extended systems such as liquids and amorphous solids [174]. The self consistency is achieved by the modified Broyden method [229] and the k-points are sampled either from the input or automatically detected based on the crystal symmetries starting from a uniform grid [230, 231]. For metallic systems various broadening techniques such as Gaussian, Lorentzian, Fermi-Dirac, Methfessel–Paxton [232], and Marzari-Vanderbilt cold smearing [233] are implemented. The structural optimizations are performed by Broyden-Fletcher-Goldfarb-Shanno (BFGS) [234] algorithm or damped dynamics.

## Spanish Initiative for Electronic Simulations with Thousands of Atoms (SIESTA)

SIESTA is a first principle density functional method to perform efficient electronic structure calculations and *ab initio* molecular dynamics calculations for large extended systems. The efficiency of SIESTA is due to the use of localized basis sets and algorithms which scale linearly for suitable systems. This method uses the standard norm-conserving PP's the local basis sets are generated from the linear combination of atomic orbitals which includes multiple zeta and polarization orbitals. The use of these linear combination of atomic orbitals (LCAO) basis sets reduces computational costs. Along with the Born-Oppenhimer approximation, exchange-correlation functionals are treated within local spin density and generalized gradient approximations. The atomic coordinates and supercell sizes are relaxed using mainly conjugate gradient minimization [235]. To exchange-

correlation potentials and matrix elements are calculated by projecting the basis functions and electronic density on real space grids. The energy functionals here are modified so that their minimization produces orthogonal wavefunctions similar to the ones obtained from KS solutions, but this is done without explicit orthogonalization which reduces computational costs.

# Appendix B

## Molecular Orbital Projected Density Of States (MOPDOS)

We describe here the procedure to compute the Molecular Orbital Projected Density of States (MOPDOS) that we have recently implemented in the `molecularpdos.x` code within the Quantum ESPRESSO distribution [174]. As we used in the current framework, the aim is to single out the contributions to the density of states of an adsorbed system coming from the orbitals of the free molecule. In more general terms, one can analyze the electronic structure of a given system named "A" (here, the molecule/graphene interface) in terms of the energy levels of a part of it named "B" (here, the molecule). This approach may also be used to analyze a complex molecule in terms of its subunits, or a different electronic configuration (say, A is the molecule with a core-level excitation while B is the same but in the ground state as we did to study excitations of pentacene [236]).

If we indicate by $|\psi^A_{n_a\mathbf{k}}\rangle$ the eigenvectors of system A and by $\varepsilon^A_{n_a\mathbf{k}}$ its eigenvalues (same for system B), where $\mathbf{k}$ is the k-vector in the Brillouin zone with weight $\omega_\mathbf{k}$, the MOPDOS of system A, projected onto the $n_b$-th orbital of system B and evaluated at the energy $E$ reads:

$$MOPDOS_{n_b}(E) = \sum_{n_a\mathbf{k}} \omega_\mathbf{k} \, |\langle \psi^B_{n_b\mathbf{k}} | \psi^A_{n_a\mathbf{k}} \rangle|^2 \, \delta(E - \varepsilon^A_{n_a\mathbf{k}}). \tag{1}$$

The eigenstates are computed by separate `pw.x` calculations for A and B; for consistency, the same unit cell and **k** sampling should be used. A shortcoming of the plane wave representation is that direct evaluation of the overlap integral $|\langle\psi^B_{n_b\mathbf{k}}|\psi^A_{n_a\mathbf{k}}\rangle|^2$ requires handling the full states for the two systems, which can be computationally demanding already for a moderately large unit cell (of the order of $10^6$ plane waves or real space points in the case presented here, for each **k** and orbital). Our implementation instead goes through a more efficient local basis set representation of the system. Let us indicate by $|\phi^{nlm}_I\rangle \equiv |\phi_\nu\rangle$, with $\nu = (I,n,l,m)$, the atomic wavefunction of atom $I$ with quantum numbers $n$, $l$, and $m$. The number of such states, $N_\phi$, is generally much smaller than that of plane waves making the calculations more manageable (here, $N_\phi \approx 300$). Hence we can approximate the eigenfunctions in terms of this local basis set:

$$|\psi^A_{n_a\mathbf{k}}\rangle \approx \sum_\nu P^A_{n_a\mathbf{k},\nu}|\phi_\nu\rangle \tag{2}$$

$$|\psi^B_{n_b\mathbf{k}}\rangle \approx \sum_\nu P^B_{n_b\mathbf{k},\nu}|\phi_\nu\rangle \tag{3}$$

where the coefficients $P$ are the complex projections of the Kohn-Sham eigenstates onto the local basis, $P^A_{n_a\mathbf{k},\nu} = \langle\phi_\nu|\psi^A_{n_a\mathbf{k}}\rangle$ and similarly for B. The above expressions are approximate since the local basis set does not span completely the original Hilbert space (see, e.g., the "spilling" [237]) but this is often of no concern to a qualitative analysis. Within Quantum ESPRESSO, the coefficients $P$ are computed by the `projwfc.x` code in a standard calculation of the DOS projected onto atomic orbitals and are stored in the file `atomic_proj.xml`. The execution of `projwfc.x` has to be performed for systems A and B separately.

The orbital overlaps in Eq. (1) are eventually computed from Eqs. (2) and (3) as:

$$\langle\psi^B_{n_b\mathbf{k}}|\psi^A_{n_a\mathbf{k}}\rangle = \sum_\nu (P^B_{n_b\mathbf{k},\nu})^* P^A_{n_a\mathbf{k},\nu}. \tag{4}$$

Notice that the index $\nu$ in the summation should identify the same atomic state in

the two systems for the local orbitals which are common for the two systems only. So, if system B is a subsystem of A, we have $N_\phi^A > N_\phi^B$ and the summation runs over $N_\phi^B$ states. We remark that, for an adsorbed radical, where the dangling bond is saturated by the surface, system B is most effectively taken as the radical saturated by an hydrogen atom whose atomic state should not be included in Eq. (4). In all cases, the fraction of atomic states to be used can be specified in input by appropriate variables (`i_atmwfc_beg_full/part` and `i_atmwfc_end_full/part`), as illustrated by the following sample input for a pyridine radical adsorbed on $5 \times 7$ graphene:

```
&INPUTMOPDOS
  xmlfile_full='full/atomic_proj.xml'
  i_atmwfc_beg_full=1
  i_atmwfc_end_full=28
  xmlfile_part='part/atomic_proj.xml'
  i_atmwfc_beg_part=2
  i_atmwfc_end_part=29
  i_bnd_beg_part=15
  i_bnd_end_part=16
  ... plotting ranges
  ... broadening parameters
/
```

The full system (A) has 75 C atoms (70 from graphene and 5 from the molecule) and 1 N atom with 2s and 2p orbitals and 4 H atoms with 1s orbitals for a total of $N_\phi^A = 75 \times 4 + 1 \times 4 + 4 \times 1 = 308$, 280 from graphene and 28 from the radical. The saturated molecule (B) has one H atom more hence $N_\phi^B = 29$ atomic orbitals. In the above example we project all states of the full system onto the molecular HOMO and LUMO (orbitals 15 and 16), assuming that the graphene atoms are

listed last in system A and that the H atom saturating the dangling bond (to be neglected) is given first in system B. Had we saturated the radical with a methyl group, 7 atomic orbitals should have been neglected from system B.

# Bibliography


[1] K. S. Novoselov. Electric Field Effect in Atomically Thin Carbon Films. *Science*, 306(5696):666–669, October 2004.

[2] P. R. Wallace. The Band Theory of Graphite. *Physical Review*, 71(9):622–634, May 1947.

[3] S. Reich, J. Maultzsch, C. Thomsen, and P. Ordejón. Tight-binding description of graphene. *Physical Review B*, 66(3), July 2002.

[4] R. S. Deacon, K.-C. Chuang, R. J. Nicholas, K. S. Novoselov, and A. K. Geim. Cyclotron resonance study of the electron and hole velocity in graphene monolayers. *Physical Review B*, 76(8), August 2007.

[5] A. H. Castro Neto, F. Guinea, N. M. R. Peres, K. S. Novoselov, and A. K. Geim. The electronic properties of graphene. *Reviews of Modern Physics*, 81(1):109–162, January 2009.

[6] Jean-Noe Fuchs and Mark Oliver Goerbig. Introduction to the Physical Properties of Graphene.

[7] Cristina Bena and Steven A. Kivelson. Quasiparticle scattering and local density of states in graphite. *Physical Review B*, 72(12), September 2005.

[8] Aaron Bostwick, Taisuke Ohta, Thomas Seyller, Karsten Horn, and Eli Rotenberg. Quasiparticle dynamics in graphene. *Nature Physics*, 3(1):36–40, January 2007.

[9] Georgi Diankov, Michael Neumann, and David Goldhaber-Gordon. Extreme Monolayer-Selectivity of Hydrogen-Plasma Reactions with Graphene. *ACS Nano*, 7(2):1324–1332, February 2013.

[10] Pablo A. Denis and Federico Iribarne. Comparative Study of Defect Reactivity in Graphene. *The Journal of Physical Chemistry C*, 117(37):19048–19055, September 2013.

[11] Ali Eftekhari and Parvaneh Jafarkhani. Curly Graphene with Specious Interlayers Displaying Superior Capacity for Hydrogen Storage. *The Journal of Physical Chemistry C*, 117(48):25845–25851, December 2013.

[12] Yasuhiro Yamada, Kazumasa Murota, Ryo Fujita, Jungpil Kim, Ayuko Watanabe, Masashi Nakamura, Satoshi Sato, Kenji Hata, Peter Ercius, Jim Ciston, Cheng Yu Song, Kwanpyo Kim, William Regan, Will Gannett, and Alex Zettl. Subnanometer Vacancy Defects Introduced on Graphene by Oxygen Gas. *Journal of the American Chemical Society*, 136(6):2232–2235, February 2014.

[13] Yasuhiro Yamada, Hajime Yasuda, Kazumasa Murota, Masashi Nakamura, Toshiaki Sodesawa, and Satoshi Sato. Analysis of heat-treated graphite oxide by X-ray photoelectron spectroscopy. *Journal of Materials Science*, 48(23):8171–8198, December 2013.

[14] Yasuhiro Yamada, Jungpil Kim, Shintaro Matsuo, and Satoshi Sato. Nitrogen-containing graphene analyzed by X-ray photoelectron spectroscopy. *Carbon*, 70:59–74, April 2014.

[15] J. C Charlier, P.C Eklund, J Zhu, A.C Ferrari, A Jorio, G Dresselhaus, and M.S Dresselhaus. Electron and Phonon Properties of Graphene: Their Relationship with Carbon Nanotubes. In *Carbon Nanotubes: Advanced Topics in the Synthesis, Structure, Properties and Applications.* Berlin/Heidelberg: Springer-Verlag., 2007.

[16] A. K. Geim and K. S. Novoselov. The rise of graphene. *Nature Materials*, 6(3):183–191, March 2007.

[17] K. S. Novoselov, A. K. Geim, S. V. Morozov, D. Jiang, M. I. Katsnelson, I. V. Grigorieva, S. V. Dubonos, and A. A. Firsov. Two-dimensional gas of massless Dirac fermions in graphene. *Nature*, 438(7065):197–200, November 2005.

[18] S. V. Morozov, K. S. Novoselov, M. I. Katsnelson, F. Schedin, D. C. Elias, J. A. Jaszczak, and A. K. Geim. Giant Intrinsic Carrier Mobilities in Graphene and Its Bilayer. *Physical Review Letters*, 100(1), January 2008.

[19] Jian-Hao Chen, Chaun Jang, Shudong Xiao, Masa Ishigami, and Michael S. Fuhrer. Intrinsic and extrinsic performance limits of graphene devices on SiO2. *Nature Nanotechnology*, 3(4):206–209, April 2008.

[20] Akin Akturk and Neil Goldsman. Electron transport and full-band electron-phonon interactions in graphene. *Journal of Applied Physics*, 103(5):053702, March 2008.

[21] Gordon W. Semenoff. Condensed-Matter Simulation of a Three-Dimensional Anomaly. *Physical Review Letters*, 53(26):2449–2452, December 1984.

[22] V. P. Gusynin and S. G. Sharapov. Unconventional Integer Quantum Hall Effect in Graphene. *Physical Review Letters*, 95(14), September 2005.

[23] C. Lee, X. Wei, J. W. Kysar, and J. Hone. Measurement of the Elastic Properties and Intrinsic Strength of Monolayer Graphene. *Science*, 321(5887):385–388, July 2008.

[24] Benjamin D. Briggs, Bhaskar Nagabhirava, Gayathri Rao, Robert Geer, Haiyuan Gao, Yang Xu, and Bin Yu. Electromechanical robustness of monolayer graphene with extreme bending. *Applied Physics Letters*, 97(22):223102, November 2010.

[25] Ardavan Zandiatashbar, Gwan-Hyoung Lee, Sung Joo An, Sunwoo Lee, Nithin Mathew, Mauricio Terrones, Takuya Hayashi, Catalin R. Picu, James Hone, and Nikhil Koratkar. Effect of defects on the intrinsic strength and stiffness of graphene. *Nature Communications*, 5, January 2014.

[26] I. W. Frank, D. M. Tanenbaum, A. M. van der Zande, and P. L. McEuen. Mechanical properties of suspended graphene sheets. *Journal of Vacuum Science & Technology B: Microelectronics and Nanometer Structures*, 25(6):2558, 2007.

[27] N. D. Mermin and H. Wagner. Absence of Ferromagnetism or Antiferromagnetism in One- or Two-Dimensional Isotropic Heisenberg Models. *Physical Review Letters*, 17(22):1133–1136, November 1966.

[28] Jannik C. Meyer, A. K. Geim, M. I. Katsnelson, K. S. Novoselov, T. J. Booth, and S. Roth. The structure of suspended graphene sheets. *Nature*, 446(7131):60–63, March 2007.

[29] Johan M. Carlsson. Graphene: Buckle or break. *Nature Materials*, 6(11):801–802, November 2007.

[30] A. Fasolino, J. H. Los, and M. I. Katsnelson. Intrinsic ripples in graphene. *Nature Materials*, 6(11):858–861, November 2007.

[31] D. Bolmatov and Chung-Yu Mou. Graphene-based modulation-doped superlattice structures. *Journal of Experimental and Theoretical Physics*, 112(1):102–107, January 2011.

[32] Dima Bolmatov. Thermodynamic properties of tunneling quasiparticles in graphene-based structures. *Physica C: Superconductivity*, 471(23-24):1651–1654, December 2011.

[33] Joseph N. Grima, Szymon Winczewski, Luke Mizzi, Michael C. Grech, Reuben Cauchi, Ruben Gatt, Daphne Attard, Krzysztof W. Wojciechowski, and Jarosław Rybicki. Tailoring Graphene to Achieve Negative Poisson's Ratio Properties. *Advanced Materials*, 27(8):1455–1459, February 2015.

[34] Elliott H. Lieb. Two theorems on the Hubbard model. *Physical Review Letters*, 62(10):1201–1204, March 1989.

[35] Oleg V Yazyev. Emergence of magnetism in graphene materials and nanostructures. *Reports on Progress in Physics*, 73(5):056501, May 2010.

[36] Oleg V. Yazyev and Lothar Helm. Defect-induced magnetism in graphene. *Physical Review B*, 75(12), March 2007.

[37] R. R. Nair, M. Sepioni, I-Ling Tsai, O. Lehtinen, J. Keinonen, A. V. Krasheninnikov, T. Thomson, A. K. Geim, and I. V. Grigorieva. Spin-half paramagnetism in graphene induced by point defects. *Nature Physics*, 8(3):199–202, January 2012.

[38] Ayako Hashimoto, Kazu Suenaga, Alexandre Gloter, Koki Urita, and Sumio Iijima. Direct evidence for atomic defects in graphene layers. *Nature*, 430(7002):870–873, August 2004.

[39] Hai-Yao Deng and Katsunori Wakabayashi. Edge effect on a vacancy state in semi-infinite graphene. *Physical Review B*, 90(11), September 2014.

[40] Kyoko Nakada, Mitsutaka Fujita, Gene Dresselhaus, and Mildred S. Dresselhaus. Edge state in graphene ribbons: Nanometer size effect and edge shape dependence. *Physical Review B*, 54(24):17954–17961, December 1996.

[41] Katsunori Wakabayashi, Mitsutaka Fujita, Hiroshi Ajiki, and Manfred Sigrist. Electronic and magnetic properties of nanographite ribbons. *Physical Review B*, 59(12):8271–8282, March 1999.

[42] Donat J. Adams, Oliver Gröning, Carlo A. Pignedoli, Pascal Ruffieux, Roman Fasel, and Daniele Passerone. Stable ferromagnetism and doping-induced half-metallicity in asymmetric graphene nanoribbons. *Physical Review B*, 85(24), June 2012.

[43] J. Zhou, Q. Wang, Q. Sun, X. S. Chen, Y. Kawazoe, and P. Jena. Ferromagnetism in Semihydrogenated Graphene Sheet. *Nano Letters*, 9(11):3867–3870, November 2009.

[44] D. W. Boukhvalov, M. I. Katsnelson, and A. I. Lichtenstein. Hydrogen on graphene: Electronic structure, total energy, structural distortions and magnetism from first-principles calculations. *Physical Review B*, 77(3), January 2008.

[45] Simone Casolo, Ole Martin Lø vvik, Rocco Martinazzo, and Gian Franco Tantardini. Understanding adsorption of hydrogen atoms on graphene. *The Journal of Chemical Physics*, 130(5):054704, 2009.

[46] Haitao Liu, Sunmin Ryu, Zheyuan Chen, Michael L. Steigerwald, Colin

Nuckolls, and Louis E. Brus. Photochemical Reactivity of Graphene. *Journal of the American Chemical Society*, 131(47):17099–17101, December 2009.

[47] Alexander Sinitskii, Ayrat Dimiev, David A. Corley, Alexandra A. Fursina, Dmitry V. Kosynkin, and James M. Tour. Kinetics of Diazonium Functionalization of Chemically Converted Graphene Nanoribbons. *ACS Nano*, 4(4):1949–1954, April 2010.

[48] Sandip Niyogi, Elena Bekyarova, Mikhail E. Itkis, Hang Zhang, Kristin Shepperd, Jeremy Hicks, Michael Sprinkle, Claire Berger, Chun Ning Lau, Walt A. deHeer, Edward H. Conrad, and Robert C. Haddon. Spectroscopy of Covalently Functionalized Graphene. *Nano Letters*, 10(10):4061–4066, October 2010.

[49] T. L. Makarova, A. L. Shelankov, A. A. Zyrianova, A. I. Veinger, T. V. Tisnek, E. Lähderanta, A. I. Shames, A. V. Okotrub, L. G. Bulusheva, G. N. Chekhova, D. V. Pinakov, I. P. Asanov, and ž. Šljivančanin. Edge state magnetism in zigzag-interfaced graphene via spin susceptibility measurements. *Scientific Reports*, 5:13382, August 2015.

[50] Andrey K. Bodenmann and Allan H. MacDonald. Graphene: Exploring carbon flatland. *Physics Today*, 60(8):35–41, August 2007.

[51] A. K. Geim. Graphene: Status and Prospects. *Science*, 324(5934):1530–1534, June 2009.

[52] F. V. Kusmartsev, W. M. Wu, M. P. Pierpoint, and K. C. Yung. Application of Graphene Within Optoelectronic Devices and Transistors. In Prabhakar Misra, editor, *Applied Spectroscopy and the Science of Nanomateri-*

*als*, volume 2, pages 191–221. Springer Singapore, Singapore, 2015. DOI: 10.1007/978-981-287-242-5_9.

[53] Buddhika Jayasena and Sathyan Subbiah. A novel mechanical cleavage method for synthesizing few-layer graphenes. *Nanoscale Research Letters*, 6(1):95, 2011.

[54] B Jayasena, C D Reddy, and S Subbiah. Separation, folding and shearing of graphene layers during wedge-based mechanical exfoliation. *Nanotechnology*, 24(20):205301, May 2013.

[55] Keith R. Paton, Eswaraiah Varrla, Claudia Backes, Ronan J. Smith, Umar Khan, Arlene O'Neill, Conor Boland, Mustafa Lotya, Oana M. Istrate, Paul King, Tom Higgins, Sebastian Barwich, Peter May, Pawel Puczkarski, Iftikhar Ahmed, Matthias Moebius, Henrik Pettersson, Edmund Long, João Coelho, Sean E. O'Brien, Eva K. McGuire, Beatriz Mendoza Sanchez, Georg S. Duesberg, Niall McEvoy, Timothy J. Pennycook, Clive Downing, Alison Crossley, Valeria Nicolosi, and Jonathan N. Coleman. Scalable production of large quantities of defect-free few-layer graphene by shear exfoliation in liquids. *Nature Materials*, 13(6):624–630, April 2014.

[56] Tesfaye Abtew, Bi-Ching Shih, Sarbajit Banerjee, and Peihong Zhang. Graphene–ferromagnet interfaces: hybridization, magnetization and charge transfer. *Nanoscale*, 5(5):1902, 2013.

[57] Peter Sutter. Epitaxial graphene: How silicon leaves the scene. *Nature Materials*, 8(3):171–172, March 2009.

[58] Taisuke Ohta, Aaron Bostwick, J. L. McChesney, Thomas Seyller, Karsten Horn, and Eli Rotenberg. Interlayer Interaction and Electronic Screening

in Multilayer Graphene Investigated with Angle-Resolved Photoemission Spectroscopy. *Physical Review Letters*, 98(20), May 2007.

[59] Aaron Bostwick, Taisuke Ohta, Jessica L McChesney, Konstantin V Emtsev, Thomas Seyller, Karsten Horn, and Eli Rotenberg. Symmetry breaking in few layer graphene films. *New Journal of Physics*, 9(10):385–385, October 2007.

[60] S. Y. Zhou, G.-H. Gweon, J. Graf, A. V. Fedorov, C. D. Spataru, R. D. Diehl, Y. Kopelevich, D.-H. Lee, Steven G. Louie, and A. Lanzara. First direct observation of Dirac fermions in graphite. *Nature Physics*, 2(9):595–599, September 2006.

[61] Ram Sevak Singh, Venkatram Nalla, Wei Chen, Andrew Thye Shen Wee, and Wei Ji. Laser Patterning of Epitaxial Graphene for Schottky Junction Photodetectors. *ACS Nano*, 5(7):5969–5975, July 2011.

[62] E. N. Voloshina, Yu. S. Dedkov, S. Torbrügge, A. Thissen, and M. Fonin. Graphene on Rh(111): Scanning tunneling and atomic force microscopies studies. *Applied Physics Letters*, 100(24):241606, June 2012.

[63] I. Pletikosić, M. Kralj, P. Pervan, R. Brako, J. Coraux, A. T. N'Diaye, C. Busse, and T. Michely. Dirac Cones and Minigaps for Graphene on Ir(111). *Physical Review Letters*, 102(5), February 2009.

[64] Arjun Dahal and Matthias Batzill. Graphene–nickel interfaces: a review. *Nanoscale*, 6(5):2548, 2014.

[65] Keun Soo Kim, Yue Zhao, Houk Jang, Sang Yoon Lee, Jong Min Kim, Kwang S. Kim, Jong-Hyun Ahn, Philip Kim, Jae-Young Choi, and Byung Hee Hong. Large-scale pattern growth of graphene films for stretchable transparent electrodes. *Nature*, 457(7230):706–710, February 2009.

[66] Sukang Bae, Hyeongkeun Kim, Youngbin Lee, Xiangfan Xu, Jae-Sung Park, Yi Zheng, Jayakumar Balakrishnan, Tian Lei, Hye Ri Kim, Young Il Song, Young-Jin Kim, Kwang S. Kim, Barbaros Özyilmaz, Jong-Hyun Ahn, Byung Hee Hong, and Sumio Iijima. Roll-to-roll production of 30-inch graphene films for transparent electrodes. *Nature Nanotechnology*, 5(8):574–578, August 2010.

[67] Javad Rafiee, Xi Mi, Hemtej Gullapalli, Abhay V. Thomas, Fazel Yavari, Yunfeng Shi, Pulickel M. Ajayan, and Nikhil A. Koratkar. Wetting transparency of graphene. *Nature Materials*, 11(3):217–222, January 2012.

[68] Robert S. Weatherup, Bernhard C. Bayer, Raoul Blume, Caterina Ducati, Carsten Baehtz, Robert Schlögl, and Stephan Hofmann. In Situ Characterization of Alloy Catalysts for Low-Temperature Graphene Growth. *Nano Letters*, 11(10):4154–4160, October 2011.

[69] X. Li, W. Cai, J. An, S. Kim, J. Nah, D. Yang, R. Piner, A. Velamakanni, I. Jung, E. Tutuc, S. K. Banerjee, L. Colombo, and R. S. Ruoff. Large-Area Synthesis of High-Quality and Uniform Graphene Films on Copper Foils. *Science*, 324(5932):1312–1314, June 2009.

[70] L. A. Ponomarenko, F. Schedin, M. I. Katsnelson, R. Yang, E. W. Hill, K. S. Novoselov, and A. K. Geim. Chaotic Dirac Billiard in Graphene Quantum Dots. *Science*, 320(5874):356–358, April 2008.

[71] X. Wang, X. Li, L. Zhang, Y. Yoon, P. K. Weber, H. Wang, J. Guo, and H. Dai. N-Doping of Graphene Through Electrothermal Reactions with Ammonia. *Science*, 324(5928):768–771, May 2009.

[72] Floriano Traversi, Valeria Russo, and Roman Sordan. Integrated comple-

mentary graphene inverter. *Applied Physics Letters*, 94(22):223312, June 2009.

[73] Y.-M. Lin, C. Dimitrakopoulos, K. A. Jenkins, D. B. Farmer, H.-Y. Chiu, A. Grill, and Ph. Avouris. 100-GHz Transistors from Wafer-Scale Epitaxial Graphene. *Science*, 327(5966):662–662, February 2010.

[74] Y.-M. Lin, A. Valdes-Garcia, S.-J. Han, D. B. Farmer, I. Meric, Y. Sun, Y. Wu, C. Dimitrakopoulos, A. Grill, P. Avouris, and K. A. Jenkins. Wafer-Scale Graphene Integrated Circuit. *Science*, 332(6035):1294–1297, June 2011.

[75] Elena Bekyarova, Mikhail E. Itkis, Palanisamy Ramesh, Claire Berger, Michael Sprinkle, Walt A. de Heer, and Robert C. Haddon. Chemical Modification of Epitaxial Graphene: Spontaneous Grafting of Aryl Groups. *Journal of the American Chemical Society*, 131(4):1336–1337, February 2009.

[76] Guanxiong Liu, Sonia Ahsan, Alexander G. Khitun, Roger K. Lake, and Alexander A. Balandin. Graphene-based non-Boolean logic circuits. *Journal of Applied Physics*, 114(15):154310, October 2013.

[77] F. Schedin, A. K. Geim, S. V. Morozov, E. W. Hill, P. Blake, M. I. Katsnelson, and K. S. Novoselov. Detection of individual gas molecules adsorbed on graphene. *Nature Materials*, 6(9):652–655, September 2007.

[78] Kyle R. Ratinac, Wenrong Yang, Simon P. Ringer, and Filip Braet. Toward Ubiquitous Environmental Gas Sensors?Capitalizing on the Promise of Graphene. *Environmental Science & Technology*, 44(4):1167–1176, February 2010.

[79] Yu-Ming Lin and Phaedon Avouris. Strong Suppression of Electrical Noise in Bilayer Graphene Nanodevices. *Nano Letters*, 8(8):2119–2125, August 2008.

[80] Yaping Dan, Ye Lu, Nicholas J. Kybert, Zhengtang Luo, and A. T. Charlie Johnson. Intrinsic Response of Graphene Vapor Sensors. *Nano Letters*, 9(4):1472–1475, April 2009.

[81] Xuan Wang, Linjie Zhi, and Klaus Müllen. Transparent, Conductive Graphene Electrodes for Dye-Sensitized Solar Cells. *Nano Letters*, 8(1):323–327, January 2008.

[82] Goki Eda, Giovanni Fanchini, and Manish Chhowalla. Large-area ultrathin films of reduced graphene oxide as a transparent and flexible electronic material. *Nature Nanotechnology*, 3(5):270–274, May 2008.

[83] Yu Wang, Xiaohong Chen, Yulin Zhong, Furong Zhu, and Kian Ping Loh. Large area, continuous, few-layered graphene as anodes in organic photovoltaic devices. *Applied Physics Letters*, 95(6):063302, August 2009.

[84] E. Schrödinger. An Undulatory Theory of the Mechanics of Atoms and Molecules. *Physical Review*, 28(6):1049–1070, December 1926.

[85] Wolfram Koch and Max C. Holthausen. *A chemist's guide to density functional theory*. Wiley-VCH, Weinheim, 2nd ed., 5. reprint edition, 2008. OCLC: 553727271.

[86] P. Hohenberg and W. Kohn. Inhomogeneous Electron Gas. *Physical Review*, 136(3B):B864–B871, November 1964.

[87] Richard M. Martin. *Electronic structure: basic theory and practical meth-*

*ods*. Cambridge University Press, Cambridge, UK ; New York, 1st pbk. ed. with corrections edition, 2008.

[88] G. P. Brivio and M. I. Trioni. The adiabatic molecule–metal surface interaction: Theoretical approaches. *Reviews of Modern Physics*, 71(1):231–265, January 1999.

[89] W. Kohn. Nobel Lecture: Electronic structure of matter—wave functions and density functionals. *Reviews of Modern Physics*, 71(5):1253–1266, October 1999.

[90] L. H. Thomas. The calculation of atomic fields. *Mathematical Proceedings of the Cambridge Philosophical Society*, 23(05):542, January 1927.

[91] Fermi Enrico. Un Metodo Statistico per la Determinazione di alcune Prioprietà dell'Atomo. *Rend. Accad. Naz. Lincei*, 6:602–607, 1927.

[92] W. Kohn and L. J. Sham. Self-Consistent Equations Including Exchange and Correlation Effects. *Physical Review*, 140(4A):A1133–A1138, November 1965.

[93] null Becke. Density-functional exchange-energy approximation with correct asymptotic behavior. *Physical Review. A, General Physics*, 38(6):3098–3100, September 1988.

[94] John P. Perdew and Yue Wang. Accurate and simple analytic representation of the electron-gas correlation energy. *Physical Review B*, 45(23):13244–13249, June 1992.

[95] John Perdew, Kieron Burke, and Yue Wang. Generalized gradient approximation for the exchange-correlation hole of a many-electron system. *Physical Review B*, 54(23):16533–16539, dec 1996.

[96] Jp Perdew, Kieron Burke, and M Ernzerhof. Generalized Gradient Approximation Made Simple. *Physical Review Letters*, 77(18):3865–3868, oct 1996.

[97] Tomasz A. Wesolowski and Fabien Tran. Gradient-free and gradient-dependent approximations in the total energy bifunctional for weakly overlapping electron densities. *The Journal of Chemical Physics*, 118(5):2072–2080, February 2003.

[98] Stefan Grimme. Accurate description of van der Waals complexes by density functional theory including empirical corrections. *Journal of Computational Chemistry*, 25(12):1463–1473, September 2004.

[99] Stefan Grimme. Semiempirical GGA-type density functional constructed with a long-range dispersion correction. *Journal of Computational Chemistry*, 27(15):1787–1799, November 2006.

[100] Alexandre Tkatchenko and Matthias Scheffler. Accurate Molecular Van Der Waals Interactions from Ground-State Electron Density and Free-Atom Reference Data. *Physical Review Letters*, 102(7), February 2009.

[101] Stefan Grimme, Jens Antony, Stephan Ehrlich, and Helge Krieg. A consistent and accurate *ab initio* parametrization of density functional dispersion correction (DFT-D) for the 94 elements H-Pu. *The Journal of Chemical Physics*, 132(15):154104, April 2010.

[102] Yi Liu and William A. Goddard. First-Principles-Based Dispersion Augmented Density Functional Theory: From Molecules to Crystals. *The Journal of Physical Chemistry Letters*, 1(17):2550–2555, September 2010.

[103] Hyungjun Kim, Jeong-Mo Choi, and William A. Goddard. Universal Correction of Density Functional Theory to Include London Dispersion (up to

Lr, Element 103). *The Journal of Physical Chemistry Letters*, pages 360–363, January 2012.

[104] H. Rydberg, M. Dion, N. Jacobson, E. Schr?der, P. Hyldgaard, S. I. Simak, D. C. Langreth, and B. I. Lundqvist. Van der Waals Density Functional for Layered Structures. *Physical Review Letters*, 91(12), September 2003.

[105] M. Dion, H. Rydberg, E. Schr?der, D. C. Langreth, and B. I. Lundqvist. Van der Waals Density Functional for General Geometries. *Physical Review Letters*, 92(24), June 2004.

[106] Oleg A. Vydrov and Troy Van Voorhis. Nonlocal van der Waals Density Functional Made Simple. *Physical Review Letters*, 103(6), August 2009.

[107] Takeshi Sato and Hiromi Nakai. Density functional method including weak interactions: Dispersion coefficients based on the local response approximation. *The Journal of Chemical Physics*, 131(22):224104, December 2009.

[108] Oleg A. Vydrov and Troy Van Voorhis. Nonlocal van der Waals density functional: The simpler the better. *The Journal of Chemical Physics*, 133(24):244103, December 2010.

[109] Tobias Schwabe and Stefan Grimme. Double-hybrid density functionals with long-range dispersion corrections: higher accuracy and extended applicability. *Physical Chemistry Chemical Physics*, 9(26):3397, 2007.

[110] Tobias Benighaus, Robert A. DiStasio, Rohini C. Lochan, Jeng-Da Chai, and Martin Head-Gordon. Semiempirical Double-Hybrid Density Functional with Improved Description of Long-Range Correlation. *The Journal of Physical Chemistry A*, 112(12):2702–2712, March 2008.

[111] D.C. Langreth and J.P. Perdew. The exchange-correlation energy of a metallic surface. *Solid State Communications*, 17(11):1425–1429, December 1975.

[112] O. Gunnarsson and B. I. Lundqvist. Exchange and correlation in atoms, molecules, and solids by the spin-density-functional formalism. *Physical Review B*, 13(10):4274–4298, May 1976.

[113] Jiří Klimeš, David R Bowler, and Angelos Michaelides. Chemical accuracy for the van der Waals density functional. *Journal of Physics: Condensed Matter*, 22(2):022201, 2010.

[114] Minho Kim, Won June Kim, Eok Kyun Lee, S?bastien Leb?gue, and Hyungjun Kim. Recent development of atom-pairwise van der waals corrections for density functional theory: From molecules to solids. *International Journal of Quantum Chemistry*, 116(8):598–607, April 2016.

[115] Volker Heine. Electronic Structure from the Point of View of the Local Atomic Environment. In *Solid State Physics*, volume 35, pages 1–127. Elsevier, 1980. DOI: 10.1016/S0081-1947(08)60503-2.

[116] Walter Harrison. *Pseudopotentials in the theory of metals*. New York, 1966.

[117] David Vanderbilt. Soft self-consistent pseudopotentials in a generalized eigenvalue formalism. *Physical Review B*, 41(11):7892–7895, April 1990.

[118] A. Messiah. *Quantum Mechanics*. Number v. 2 in Quantum Mechanics. North-Holland Publishing Company, 1962.

[119] William A. Goddard, editor. *Handbook of nanoscience, engineering, and technology*. The electrical engineering handbook series. CRC Press, Boca Raton, 2003.

[120] K. Siegbahn and K. Edvarson. β-Ray spectroscopy in the precision range of 1 : 105. *Nuclear Physics*, 1(8):137–159, January 1956.

[121] ZhenHua Zeng, XiuFang Ma, WuChen Ding, and WeiXue Li. First-principles calculation of core-level binding energy shift in surface chemical processes. *Science China Chemistry*, 53(2):402–410, February 2010.

[122] S. García-Gil, A. García, and P. Ordejón. Calculation of core level shifts within DFT using pseudopotentials and localized basis sets. *The European Physical Journal B*, 85(7), July 2012.

[123] Paul S Bagus, Francesc Illas, Gianfranco Pacchioni, and Fulvio Parmigiani. Mechanisms responsible for chemical shifts of core-level binding energies and their relationship to chemical bonding. *Journal of Electron Spectroscopy and Related Phenomena*, 100(1-3):215–236, October 1999.

[124] E. Pehlke and M. Scheffler. Evidence for site-sensitive screening of core holes at the Si and Ge (001) surface. *Physical Review Letters*, 71(14):2338–2341, October 1993.

[125] Christopher E. Patrick and Feliciano Giustino. Structure of a Water Monolayer on the Anatase TiO 2 ( 101 ) Surface. *Physical Review Applied*, 2(1), July 2014.

[126] Georg Hähner. Near edge X-ray absorption fine structure spectroscopy as a tool to probe electronic and structural properties of thin organic films and liquids. *Chem. Soc. Rev.*, 35(12):1244–1255, 2006.

[127] Joachim Stöhr. *NEXAFS spectroscopy*. Springer, Berlin; New York, 1996. OCLC: 968660139.

[128] W. S. Hu, Y. T. Tao, Y. J. Hsu, D. H. Wei, and Y. S. Wu. Molecular Orientation of Evaporated Pentacene Films on Gold: Alignment Effect of Self-Assembled Monolayer. *Langmuir*, 21(6):2260–2266, March 2005.

[129] S. Söhnchen, S. Lukas, and G. Witte. Epitaxial growth of pentacene films on Cu(110). *The Journal of Chemical Physics*, 121(1):525, 2004.

[130] Guido Fratesi, Valeria Lanzilotto, Luca Floreano, and Gian Paolo Brivio. Azimuthal Dichroism in Near-Edge X-ray Absorption Fine Structure Spectra of Planar Molecules. *The Journal of Physical Chemistry C*, 117(13):6632–6638, April 2013.

[131] J. C. Slater, J. B. Mann, T. M. Wilson, and J. H. Wood. Nonintegral Occupation Numbers in Transition Atoms in Crystals. *Physical Review*, 184(3):672–694, August 1969.

[132] J. F. Janak. Proof that ∂ E ∂ n i = ε in density-functional theory. *Physical Review B*, 18(12):7165–7168, December 1978.

[133] L. Triguero, L. G. M. Pettersson, and H. Ågren. Calculations of near-edge x-ray-absorption spectra of gas-phase and chemisorbed molecules by means of density-functional and transition-potential theory. *Physical Review B*, 58(12):8097–8110, September 1998.

[134] M. Leetmaa, M.P. Ljungberg, A. Lyubartsev, A. Nilsson, and L.G.M. Pettersson. Theoretical approximations to X-ray absorption spectroscopy of liquid water and ice. *Journal of Electron Spectroscopy and Related Phenomena*, 177(2-3):135–157, March 2010.

[135] Matteo Cavalleri, Michael Odelius, Dennis Nordlund, Anders Nilsson, and Lars G. M. Pettersson. Half or full core hole in density functional the-

ory X-ray absorption spectrum calculations of water? *Physical Chemistry Chemical Physics*, 7(15):2854, 2005.

[136] Liang Cao, Xing-Yu Gao, Andrew T. S. Wee, and Dong-Chen Qi. Quantitative Femtosecond Charge Transfer Dynamics at Organic/Electrode Interfaces Studied by Core-Hole Clock Spectroscopy. *Advanced Materials*, 26(46):7880–7888, December 2014.

[137] X Zhu. Electronic structure and electron dynamics at molecule?metal interfaces: implications for molecule-based electronics. *Surface Science Reports*, 56(1-2):1–83, November 2004.

[138] P. A. Brühwiler, O. Karis, and N. Mårtensson. Charge-transfer dynamics studied using resonant core spectroscopies. *Rev. Mod. Phys.*, 74:703–740, Jul 2002.

[139] Li Wang, Wei Chen, and Andrew Thye Shen Wee. Charge transfer across the molecule/metal interface using the core hole clock technique. *Surface Science Reports*, 63(11):465–486, November 2008.

[140] Paolo Vilmercati, Dean Cvetko, Albano Cossaro, and Alberto Morgante. Heterostructured organic interfaces probed by resonant photoemission. *Surface Science*, 603(10-12):1542–1556, June 2009.

[141] R. Friedlein, S. Braun, M.P. de Jong, W. Osikowicz, M. Fahlman, and W.R. Salaneck. Ultra-fast charge transfer in organic electronic materials and at hybrid interfaces studied using the core-hole clock technique. *Journal of Electron Spectroscopy and Related Phenomena*, 183(1-3):101–106, January 2011.

[142] Masahide Ohno. Deexcitation processes in adsorbates. *Physical Review B*, 50(4):2566–2575, July 1994.

[143] Mary Coville and T. Darrah Thomas. Molecular effects on inner-shell lifetimes: Possible test of the one-center model of Auger decay. *Physical Review A*, 43(11):6053–6056, 1991.

[144] Guido Fratesi, Carlo Motta, Mario Italo Trioni, Gian Paolo Brivio, and Daniel Sánchez-Portal. Resonant Lifetime of Core-Excited Organic Adsorbates from First Principles. *The Journal of Physical Chemistry C*, 118(17):8775–8782, May 2014.

[145] J. Ben Taylor, Louise C. Mayor, Janine C. Swarbrick, James N. O'Shea, Cristina Isvoranu, and Joachim Schnadt. Adsorption and charge transfer dynamics of bi-isonicotinic acid on Au(111). *The Journal of Chemical Physics*, 127(13):134707, October 2007.

[146] Olgun Adak, Gregor Kladnik, Gregor Bavdek, Albano Cossaro, Alberto Morgante, Dean Cvetko, and Latha Venkataraman. Ultrafast Bidirectional Charge Transport and Electron Decoherence at Molecule/Surface Interfaces: A Comparison of Gold, Graphene, and Graphene Nanoribbon Surfaces. *Nano Letters*, 15(12):8316–8321, 2015.

[147] Dean Cvetko, Guido Fratesi, Gregor Kladnik, Albano Cossaro, Gian Paolo Brivio, Latha Venkataraman, and Alberto Morgante. Ultrafast electron injection into photo-excited organic molecules. *Phys. Chem. Chem. Phys.*, 18(32):22140–22145, 2016.

[148] Arunabh Batra, Gregor Kladnik, Héctor Vázquez, Jeffrey S. Meisner, Luca Floreano, Colin Nuckolls, Dean Cvetko, Alberto Morgante, and Latha Venkataraman. Quantifying through-space charge transfer dynamics in $\pi$-coupled molecular systems. *Nature Communications*, 3:1086, September 2012.

[149] Abhilash Ravikumar, Anu Baby, He Lin, Gian Paolo Brivio, and Guido Fratesi. Femtomagnetism in graphene induced by core level excitation of organic adsorbates. *Scientific reports*, 6(April):24603, 2016.

[150] Ujjal Kumar Sur. Graphene: A Rising Star on the Horizon of Materials Science. *International Journal of Electrochemistry*, 2012:1–12, 2012.

[151] D. Gunlycke, H. M. Lawler, and C. T. White. Room-temperature ballistic transport in narrow graphene strips. *Physical Review B*, 75(8):085418, February 2007.

[152] K. S. Novoselov, Z. Jiang, Y. Zhang, S. V. Morozov, H. L. Stormer, U. Zeitler, J. C. Maan, G. S. Boebinger, P. Kim, and A. K. Geim. Room-Temperature Quantum Hall Effect in Graphene. *Science*, 315(5817):1379–1379, March 2007.

[153] Yuanbo Zhang, Yan-Wen Tan, Horst L. Stormer, and Philip Kim. Experimental observation of the quantum Hall effect and Berry's phase in graphene. *Nature*, 438(7065):201–204, November 2005.

[154] K.I. Bolotin, K.J. Sikes, Z. Jiang, M. Klima, G. Fudenberg, J. Hone, P. Kim, and H.L. Stormer. Ultrahigh electron mobility in suspended graphene. *Solid State Communications*, 146(9-10):351–355, June 2008.

[155] Kirill I. Bolotin, Fereshte Ghahari, Michael D. Shulman, Horst L. Stormer, and Philip Kim. Observation of the fractional quantum Hall effect in graphene. *Nature*, 462(7270):196–199, November 2009.

[156] I. I. Barbolina, K. S. Novoselov, S. V. Morozov, S. V. Dubonos, M. Missous, A. O. Volkov, D. A. Christian, I. V. Grigorieva, and A. K. Geim. Submicron sensors of local electric field with single-electron resolution at room temperature. *Applied Physics Letters*, 88(1):013901, 2006.

[157] Nikolaos Tombros, Csaba Jozsa, Mihaita Popinciuc, Harry T. Jonkman, and Bart J. van Wees. Electronic spin transport and spin precession in single graphene layers at room temperature. *Nature*, 448(7153):571–574, August 2007.

[158] Héctor A. Becerril, Jie Mao, Zunfeng Liu, Randall M. Stoltenberg, Zhenan Bao, and Yongsheng Chen. Evaluation of Solution-Processed Reduced Graphene Oxide Films as Transparent Conductors. *ACS Nano*, 2(3):463–470, March 2008.

[159] Chong-an Di, Dacheng Wei, Gui Yu, Yunqi Liu, Yunlong Guo, and Daoben Zhu. Patterned Graphene as Source/Drain Electrodes for Bottom-Contact Organic Field-Effect Transistors. *Advanced Materials*, 20(17):3289–3293, September 2008.

[160] E. Beaurepaire, J.-C. Merle, A. Daunois, and J.-Y. Bigot. Ultrafast Spin Dynamics in Ferromagnetic Nickel. *Physical Review Letters*, 76(22):4250–4253, May 1996.

[161] C. Boeglin, E. Beaurepaire, V. Halté, V. López-Flores, C. Stamm, N. Pontius, H. A. Dürr, and J.-Y. Bigot. Distinguishing the ultrafast dynamics of spin and orbital moments in solids. *Nature*, 465(7297):458–461, May 2010.

[162] Bin Wang, Jianwei Li, Fuming Xu, Yadong Wei, Jian Wang, and Hong Guo. Transient dynamics of magnetic Co–graphene systems. *Nanoscale*, 7(22):10030–10038, 2015.

[163] Yung-Chang Lin, Po-Yuan Teng, Po-Wen Chiu, and Kazu Suenaga. Exploring the Single Atom Spin State by Electron Spectroscopy. *Physical Review Letters*, 115(20):206803, 2015.

[164] Dietrich Menzel. Ultrafast charge transfer at surfaces accessed by core electron spectroscopies. *Chemical Society Reviews*, 37(10):2212, 2008.

[165] Michael W. Rowell, Mark A. Topinka, Michael D. McGehee, Hans Jürgen Prall, Gilles Dennler, Niyazi Serdar Sariciftci, Liangbing Hu, and George Gruner. Organic solar cells with carbon nanotube network electrodes. *Applied Physics Letters*, 88(23):23–25, 2006.

[166] Xuan Wang, , * Linjie Zhi, and Klaus Müllen*. Transparent, Conductive Graphene Electrodes for Dye-Sensitized Solar Cells. *Nanoletters*, 8:323–327, 2007.

[167] Lewis Gomez De Arco, Yi Zhang, Cody W Schlenker, Koungmin Ryu, Mark E Thompson, and Chongwu Zhou. Supporting Information for Continuous , Highly Flexible and Transparent Graphene Films by Chemical Vapor Deposition for Organic Photovoltaics. *ACS nano*, 4(5):2865–73, 2010.

[168] Piotr Matyba, Hisato Yamaguchi, Goki Eda, Manish Chhowalla, Ludvig Edman, and Nathaniel D. Robinson. Graphene and mobile ions: The key to all-plastic, solution-processed light-emitting devices. *ACS Nano*, 4(2):637–642, 2010.

[169] Junbo Wu, Mukul Agrawal, Héctor A. Becerril, Zhenan Bao, Zunfeng Liu, Yongsheng Chen, and Peter Peumans. Organic light-emitting diodes on solution-processed graphene transparent electrodes. *ACS Nano*, 4(1):43–48, 2010.

[170] Florian Blobner, Runyuan Han, Andreas Kim, Wilfried Wurth, and Peter Feulner. Spin-dependent electron transfer dynamics probed by resonant photoemission spectroscopy. *Phys. Rev. Lett.*, 112(8):086801, Feb 2014.

[171] P. Feulner, F. Blobner, J. Bauer, R. Han, A. Kim, T. Sundermann, N. Müller, U. Heinzmann, and W. Wurth. Ways to Spin Resolved Core-Hole-Clock Measurements. *e-Journal of Surface Science and Nanotechnology*, 13(0):317–323, 2015.

[172] John P. Perdew, Kieron Burke, and Yue Wang. Generalized gradient approximation for the exchange-correlation hole of a many-electron system. *Physical Review B*, 54(23):16533–16539, December 1996.

[173] John P. Perdew, Kieron Burke, and Matthias Ernzerhof. Generalized Gradient Approximation Made Simple. *Physical Review Letters*, 77(18):3865–3868, October 1996.

[174] Paolo Giannozzi, Stefano Baroni, Nicola Bonini, Matteo Calandra, Roberto Car, Carlo Cavazzoni, Davide Ceresoli, Guido L Chiarotti, Matteo Cococcioni, Ismaila Dabo, Andrea Dal Corso, Stefano de Gironcoli, Stefano Fabris, Guido Fratesi, Ralph Gebauer, Uwe Gerstmann, Christos Gougoussis, Anton Kokalj, Michele Lazzeri, Layla Martin-Samos, Nicola Marzari, Francesco Mauri, Riccardo Mazzarello, Stefano Paolini, Alfredo Pasquarello, Lorenzo Paulatto, Carlo Sbraccia, Sandro Scandolo, Gabriele Sclauzero, Ari P Seitsonen, Alexander Smogunov, Paolo Umari, and Renata M Wentzcovitch. QUANTUM ESPRESSO: a modular and open-source software project for quantum simulations of materials. *Journal of Physics: Condensed Matter*, 21(39):395502, September 2009.

[175] D. C. Elias, R. R. Nair, T. M. G. Mohiuddin, S. V. Morozov, P. Blake, M. P. Halsall, A. C. Ferrari, D. W. Boukhvalov, M. I. Katsnelson, A. K. Geim, and K. S. Novoselov. Control of Graphene's Properties by Reversible Hydrogenation: Evidence for Graphane. *Science*, 323(5914):610–613, January 2009.

[176] Toma Susi, Duncan J. Mowbray, Mathias P. Ljungberg, and Paola Ayala. Calculation of the graphene C 1s core level binding energy. *Physical Review B - Condensed Matter and Materials Physics*, 91(8):1–5, 2015.

[177] Steven Bailey, David Visontai, Colin J. Lambert, Martin R. Bryce, Harry Frampton, and David Chappell. A study of planar anchor groups for graphene-based single-molecule electronics. *The Journal of Chemical Physics*, 140(5):054708, February 2014.

[178] Lingmei Kong, Axel Enders, Talat S Rahman, and Peter A Dowben. Molecular adsorption on graphene. *Journal of Physics: Condensed Matter*, 26(44):443001, November 2014.

[179] E.N. Voloshina, D. Mollenhauer, L. Chiappisi, and B. Paulus. Theoretical study on the adsorption of pyridine derivatives on graphene. *Chemical Physics Letters*, 510(4-6):220–223, July 2011.

[180] Elton J G Santos, Andrés Ayuela, and Daniel Sánchez-Portal. Universal magnetic properties of sp 3 -type defects in covalently functionalized graphene. *New Journal of Physics*, 14(4):043022, April 2012.

[181] He Lin, Guido Fratesi, and Gian Paolo Brivio. Graphene magnetism induced by covalent adsorption of aromatic radicals. *Phys. Chem. Chem. Phys.*, 17(3):2210–2215, 2015.

[182] Jeongmin Hong, Elena Bekyarova, Ping Liang, Walt A de Heer, Robert C Haddon, and Sakhrat Khizroev. Room-temperature magnetic ordering in functionalized graphene. *Scientific reports*, 2:624, 2012.

[183] Abraham Nitzan. *Chemical dynamics in condensed phases relaxation, transfer and reactions in condensed molecular systems*. Oxford University Press, 2006.

[184] PerOlov Löwdin. On the Non-Orthogonality Problem Connected with the Use of Atomic Wave Functions in the Theory of Molecules and Crystals. *The Journal of Chemical Physics*, 18(3):365, 1950.

[185] PerOlov Löwdin. On the Nonorthogonality Problem. In *Advances in Quantum Chemistry*, volume 5, pages 185–199. Elsevier, 1970.

[186] R. Gotter, G. Fratesi, R. A. Bartynski, F. Da Pieve, F. Offi, A. Ruocco, S. Ugenti, M. I. Trioni, G. P. Brivio, and G. Stefani. Spin-dependent on-site electron correlations and localization in itinerant ferromagnets. *Physical Review Letters*, 109(12):1–5, 2012.

[187] R. Gotter, F. Offi, A. Ruocco, F. Da Pieve, R. Bartynski, M. Cini, and G. Stefani. Evidence for the collapse of short-range magnetic order in CoO at the Néel temperature. *EPL (Europhysics Letters)*, 94(3):37008, 2011.

[188] Javier Durantini, Pablo P. Boix, Miguel Gervaldo, Gustavo M. Morales, Luis Otero, Juan Bisquert, and Eva M. Barea. Photocurrent enhancement in dye-sensitized photovoltaic devices with titania–graphene composite electrodes. *Journal of Electroanalytical Chemistry*, 683:43 – 46, 2012.

[189] Johann Coraux, Alpha T N'Diaye, Martin Engler, Carsten Busse, Dirk Wall, Niemma Buckanie, Frank-J Meyer zu Heringdorf, Raoul van Gastel, Bene Poelsema, and Thomas Michely. Growth of graphene on Ir(111). *New Journal of Physics*, 11(3):039801, March 2009.

[190] Peter W. Sutter, Jan-Ingo Flege, and Eli A. Sutter. Epitaxial graphene on ruthenium. *Nature Materials*, 7(5):406–411, May 2008.

[191] Peter Sutter, Jerzy T. Sadowski, and Eli Sutter. Graphene on Pt(111): Growth and substrate interaction. *Physical Review B*, 80(24), December 2009.

[192] Peter Sutter and Eli Sutter. Microscopy of Graphene Growth, Processing, and Properties. *Advanced Functional Materials*, 23(20):2617–2634, May 2013.

[193] Arjun Dahal and Matthias Batzill. Graphene–nickel interfaces: a review. *Nanoscale*, 6(5):2548, 2014.

[194] Giovanni Bertoni, Lionel Calmels, Anne Altibelli, and Virginie Serin. First-principles calculation of the electronic structure and EELS spectra at the graphene/Ni(111) interface. *Physical Review B*, 71(7), February 2005.

[195] Hao Zhang, Xiaojun Lv, Yueming Li, Ying Wang, and Jinghong Li. P25-Graphene Composite as a High Performance Photocatalyst. *ACS Nano*, 4(1):380–386, January 2010.

[196] Lewis Gomez De Arco, Yi Zhang, Cody W. Schlenker, Koungmin Ryu, Mark E. Thompson, and Chongwu Zhou. Continuous, Highly Flexible, and Transparent Graphene Films by Chemical Vapor Deposition for Organic Photovoltaics. *ACS Nano*, 4(5):2865–2873, May 2010.

[197] P. A. Brühwiler, O. Karis, and N. Mårtensson. Charge-transfer dynamics studied using resonant core spectroscopies. *Reviews of Modern Physics*, 74(3):703–740, July 2002.

[198] H. Ueba and B. Gumhalter. Theory of two-photon photoemission spectroscopy of surfaces. *Progress in Surface Science*, 82(4-6):193–223, January 2007.

[199] H. Petek and S. Ogawa. Femtosecond time-resolved two-photon photoemission studies of electron dynamics in metals. *Progress in Surface Science*, 56(4):239–310, December 1997.

[200] N V Smith. Inverse photoemission. *Reports on Progress in Physics*, 51(9):1227–1294, September 1988.

[201] B. Fain, S. H. Lin, and V. Khidekel. Limitations of pump-probe femtosecond time-resolved experiments: Time-dependent absorption and dispersion line shapes. *Physical Review A*, 47(4):3222–3239, April 1993.

[202] A. Azima, S. Düsterer, P. Radcliffe, H. Redlin, N. Stojanovic, W. Li, H. Schlarb, J. Feldhaus, D. Cubaynes, M. Meyer, J. Dardis, P. Hayden, P. Hough, V Richardson, E. T. Kennedy, and J. T. Costello. Time-resolved pump-probe experiments beyond the jitter limitations at FLASH. *Applied Physics Letters*, 94(14):144102, 2009.

[203] Joachim Schnadt, Paul A. Brühwiler, Luc Patthey, James N. O'Shea, Sven Södergren, Michael Odelius, Rajeev Ahuja, Olof Karis, Margit Bässler, Petter Persson, Hans Siegbahn, S. Lunell, and Nils Mårtensson. Experimental evidence for sub-3-fs charge transfer from an aromatic adsorbate to a semiconductor. *Nature*, 418(6898):620–623, August 2002.

[204] Daniel Sánchez-Portal. Slab calculations and Green's function recursive methods combined to study the electronic structure of surfaces: application to Cu(111)–(4×4)-Na. *Progress in Surface Science*, 82(4-6):313–335, January 2007.

[205] Daniel Sánchez-Portal, Dietrich Menzel, and Pedro M. Echenique. First-principles calculation of charge transfer at surfaces: The case of core-excited Ar * ( 2 p 3 / 2 - 1 4 s ) on Ru(0001). *Physical Review B*, 76(23), December 2007.

[206] Guido Fratesi, Carlo Motta, Mario Italo Trioni, Gian Paolo Brivio, and Daniel Sánchez-Portal. Resonant Lifetime of Core-Excited Organic Ad-

sorbates from First Principles. *The Journal of Physical Chemistry C*, 118(17):8775–8782, may 2014.

[207] Paolo Giannozzi, Stefano Baroni, Nicola Bonini, Matteo Calandra, Roberto Car, Carlo Cavazzoni, Davide Ceresoli, Guido L Chiarotti, Matteo Cococcioni, Ismaila Dabo, Andrea Dal Corso, Stefano de Gironcoli, Stefano Fabris, Guido Fratesi, Ralph Gebauer, Uwe Gerstmann, Christos Gougoussis, Anton Kokalj, Michele Lazzeri, Layla Martin-Samos, Nicola Marzari, Francesco Mauri, Riccardo Mazzarello, Stefano Paolini, Alfredo Pasquarello, Lorenzo Paulatto, Carlo Sbraccia, Sandro Scandolo, Gabriele Sclauzero, Ari P Seitsonen, Alexander Smogunov, Paolo Umari, and Renata M Wentzcovitch. QUANTUM ESPRESSO: a modular and open-source software project for quantum simulations of materials. *Journal of physics. Condensed matter : an Institute of Physics journal*, 21(39):395502, sep 2009.

[208] Stefan Grimme. Semiempirical GGA-type density functional constructed with a long-range dispersion correction. *Journal of Computational Chemistry*, 27(15):1787–1799, nov 2006.

[209] L. Ould-Moussa, O. Poizat, M. Castellà-Ventura, G. Buntinx, and E. Kassab. *Ab Initio* Computations of the Geometrical, Electronic, and Vibrational Properties of the Ground State, the Anion Radical, and the $N$ , $N$‘ -Dihydro Cation Radical of 4,4‘-Bipyridine Compared to Transient Raman Spectra. *The Journal of Physical Chemistry*, 100(6):2072–2082, January 1996.

[210] Olivier Poizat, G. Buntinx, M. Ventura, and M. F. Lautie. Photoreduction of 4,4’-bipyridine. A time-resolved Raman analysis. *The Journal of Physical Chemistry*, 95(3):1245–1253, February 1991.

[211] Qiang Wang, Li Wei, Michael Sullivan, Shuo-Wang Yang, and Yuan Chen. Graphene layers on Cu and Ni (111) surfaces in layer controlled graphene growth. *RSC Advances*, 3(9):3046, 2013.

[212] Daniel Sánchez-Portal, Dietrich Menzel, and Pedro M. Echenique. First-principles calculation of charge transfer at surfaces: The case of core-excited Ar* (2 p 32 -1 4s) on Ru(0001). *Physical Review B - Condensed Matter and Materials Physics*, 76(23):1–19, 2007.

[213] Daniel Sánchez-Portal. Slab calculations and Green's function recursive methods combined to study the electronic structure of surfaces: application to Cu(111)–(4x4)-Na. *Progress in Surface Science*, 82(4–6):313–335, 2007.

[214] Mads Brandbyge, Jose-Luis Mozos, Pablo Ordejon, Jeremy Taylor, and Kurt Stokbro. Density functional method for nonequilibrium electron transport. *Physical Review B*, 65:18, 2001.

[215] J M Soler, E Artacho, J D Gale, A Garcìa, J Junquera, P Ordejòn, and D Sànchez-Portal. SIESTA Method For Ab Initio Order-N Materials Simulation, The. *J. Phys.: Condens. Matter*, 14(11):2745–2779, 2002.

[216] Masayuki Hasegawa, Kazume Nishidate, Takuya Hosokai, and Noriyuki Yoshimoto. Electronic-structure modification of graphene on Ni(111) surface by the intercalation of a noble metal. *Physical Review B - Condensed Matter and Materials Physics*, 87(8):1–9, 2013.

[217] Giovanni Bertoni, Lionel Calmels, Anne Altibelli, and Virginie Serin. First-principles calculation of the electronic structure and EELS spectra at the graphene/Ni(111) interface. *Physical Review B - Condensed Matter and Materials Physics*, 71(7):1–8, 2005.

[218] Miguel Fuentes-Cabrera, M. I. Baskes, Anatoli V. Melechko, and Michael L. Simpson. Bridge structure for the graphene/Ni(111) system: A first principles study. *Physical Review B - Condensed Matter and Materials Physics*, 77(3):1–5, 2008.

[219] A. Garcia-Lekue, T. Balashov, M. Olle, G. Ceballos, A. Arnau, P. Gambardella, D. Sanchez-Portal, and A. Mugarza. Spin-Dependent Electron Scattering at Graphene Edges on Ni(111). *Physical Review Letters*, 112(6):066802, 2014.

[220] M Paulsson. Non Equilibrium Green's Functions for Dummies: Introduction to the One Particle NEGF equations. *eprint arXiv:cond-mat/0210519*, page 10519, 2002.

[221] Laerte L. Patera, Cristina Africh, Robert S. Weatherup, Raoul Blume, Sunil Bhardwaj, Carla Castellarin-Cudia, Axel Knop-Gericke, Robert Schloegl, Giovanni Comelli, Stephan Hofmann, and Cinzia Cepek. *In Situ* Observations of the Atomistic Mechanisms of Ni Catalyzed Low Temperature Graphene Growth. *ACS Nano*, 7(9):7901–7912, September 2013.

[222] Leonard Kleinman and D. M. Bylander. Efficacious Form for Model Pseudopotentials. *Physical Review Letters*, 48(20):1425–1428, May 1982.

[223] D. R. Hamann, M. Schlüter, and C. Chiang. Norm-Conserving Pseudopotentials. *Physical Review Letters*, 43(20):1494–1497, November 1979.

[224] P. E. Blöchl. Projector augmented-wave method. *Physical Review B*, 50(24):17953–17979, December 1994.

[225] null Perdew, null Chevary, null Vosko, null Jackson, null Pederson, null Singh, and null Fiolhais. Atoms, molecules, solids, and surfaces: Applica-

tions of the generalized gradient approximation for exchange and correlation. *Physical Review. B, Condensed Matter*, 46(11):6671–6687, September 1992.

[226] Jianmin Tao, John P. Perdew, Viktor N. Staroverov, and Gustavo E. Scuseria. Climbing the Density Functional Ladder: Nonempirical Meta–Generalized Gradient Approximation Designed for Molecules and Solids. *Physical Review Letters*, 91(14), September 2003.

[227] John P. Perdew, Matthias Ernzerhof, and Kieron Burke. Rationale for mixing exact exchange with density functional approximations. *The Journal of Chemical Physics*, 105(22):9982–9985, December 1996.

[228] Axel D. Becke. A new mixing of Hartree–Fock and local density-functional theories. *The Journal of Chemical Physics*, 98(2):1372–1377, January 1993.

[229] D. D. Johnson. Modified Broyden's method for accelerating convergence in self-consistent calculations. *Physical Review B*, 38(18):12807–12813, December 1988.

[230] D. J. Chadi and Marvin L. Cohen. Special Points in the Brillouin Zone. *Physical Review B*, 8(12):5747–5753, December 1973.

[231] Hendrik J. Monkhorst and James D. Pack. Special points for Brillouin-zone integrations. *Physical Review B*, 13(12):5188–5192, June 1976.

[232] M. Methfessel and A. T. Paxton. High-precision sampling for Brillouin-zone integration in metals. *Physical Review B*, 40(6):3616–3621, August 1989.

[233] Nicola Marzari, David Vanderbilt, Alessandro De Vita, and M. C. Payne. Thermal Contraction and Disordering of the Al(110) Surface. *Physical Review Letters*, 82(16):3296–3299, April 1999.

[234] Salomon R Billeter, Alessandro Curioni, and Wanda Andreoni. Efficient linear scaling geometry optimization and transition-state search for direct wavefunction optimization schemes in density functional theory using a plane-wave basis. *Computational Materials Science*, 27(4):437–445, June 2003.

[235] José M Soler, Emilio Artacho, Julian D Gale, Alberto García, Javier Junquera, Pablo Ordejón, and Daniel Sánchez-Portal. The siesta method for ab initio order- n materials simulation. *Journal of Physics: Condensed Matter*, 14(11):2745, 2002.

[236] Anu Baby, He Lin, Gian Paolo Brivio, Luca Floreano, and Guido Fratesi. Core-level spectra and molecular deformation in adsorption: V-shaped pentacene on Al(001). *Beilstein Journal of Nanotechnology*, 6:2242–2251, November 2015.

[237] Daniel Sanchez-Portal, Emilio Artacho, and Jose M Soler. Projection of plane-wave calculations into atomic orbitals. *Solid State Communications*, 95(10):685–690, September 1995.